The Dissertation Committee for Seunghan Lee
certifies that this is the approved version of the following dissertation:

Discrete Hamilton's Equations for Thermo-electromagnetic Systems

Committee:

Eric P. Fahrenthold, Supervisor

Mircea Driga

Mark F. Hamilton

Raul G. Longoria

Alfred E. Traver

Discrete Hamilton's Equations for Thermo-electromagnetic Systems

by

Seunghan Lee, B.S.; M.S.

DISSERTATION

Presented to the Faculty of the Graduate School of

The University of Texas at Austin

in Partial Fulfillment

of the Requirements

for the Degree of

DOCTOR OF PHILOSOPHY

THE UNIVERSITY OF TEXAS AT AUSTIN

May 2010

Dedicated

to my parents,

my wife and my children.

Acknowledgments

The author would like to first thank God for giving me the endurance to complete this dissertation. I wish to thank the multitudes of people who helped me. First of all, I would like to express sincere gratitude and appreciation to my supervisor, Dr. Fahrenthold for many years of his support, patience and wise guidance. This work could not have been done without his help. I would also like to thank other committee members, Dr. Mircea Driga, Dr. Mark F. Hamilton, Dr. Raul G. Longoria, and Dr. Alfred E. Traver for their comments and kindness.

Thanks to all my friends for their encouragement to me. Many thanks go to my family members for their support, patience, and sacrifice during the preparation and completion of this work. I would like to give special thanks to my parents for their endless and unconditional love and support. Last but not least I also like to thank my wife Kyungmi, my daughter Seoyi, and my son Jungwoo for the time they sacrificed in getting me here.

This work was supported by the Office of Naval Research and NASA Johnson Space Center.

Discrete Hamilton's Equations for Thermo-electromagnetic Systems

Publication No. ___________________

Seunghan Lee, Ph.D.
The University of Texas at Austin, 2010

Supervisor: Eric P. Fahrenthold

Energy methods are used extensively in the formulation of discrete system models. They simplify the systematic integration of diverse kinematic schemes, and are well suited for characterizing complex energy domain coupling effects. Continuum mechanics models are by contrast normally based on partial differential equation descriptions of the physical system. The research presented here develops a new Hamiltonian method for the simulation of distributed parameter electromagnetic and thermo-electromagnetic systems. It expands the application of current system dynamics modeling techniques, to encompass complex distributed parameter electromagnetic systems.

Table of Contents

List of Tables

List of Figures

Chapter 1

Introduction

1.1 Introduction

Many practical systems incorporate dynamically interacting continuum subsystems such as an electromechanical system which is represented by a combination of electromagnetic and mechanical parts. It is not easy for an engineer to analyze such system by means of analytical or numerical methods, especially when including several different coupled energy domains.

The continuum dynamics models normally used for engineering design are formulated by constructing approximate solutions of a set of governing partial differential equations, most often using finite difference or weighted residual finite element techniques. These methods provide an accurate approach to multiphysics simulations [95] in many practical problems. However, such models are in general not simple to formulate or modify. Alternative discrete and systematic modeling techniques are needed to represent the mechanical [85], chemical [25] or electromagnetic [53] phenomena of interest in the system dynamics field.

Scientists and engineers interested in the simulation of distributed property systems are often faced with the difficult task of integrating diverse modeling schemes. Improved methods for the systematic integration of multiscale models [62][71] are therefore needed, to facilitate the use of virtual prototyping in engineering design.

In recent research [30][33][81][73][29] a discrete energy method has been developed and validated as a basic extension of classical Hamiltonian methods, to simulate the nonlinear thermomechanical dynamics of physical systems described by finite element based, particle based, and hybrid particle-finite element based kinematics. The preceding work has included formulations in Eulerian, Lagrangian, and Arbitrary Lagrangian-Eulerian frames. The governing equations for these systems differ from those which arise for example when using weighted residual finite element methods. They are instead canonical discrete Hamilton's equations, formulated without reference to any partial differential equations, and developed using reference frames and state variables not considered in classical Hamiltonian formulations.

To extend the preceding work, and thereby provide essential components of a unified Hamiltonian modeling approach, the present research formulated and validated a new discrete Hamiltonian method for distributed electromagnetic systems. The research thereby enables a unified Hamiltonian modeling approach to virtual prototyping problems for systems described by combinations of both electric and mechanical subsystems and processes. Engineers who focus on reducing costly and time consuming prototyping, through the use of computer aided engineering (CAE) software, can now achieve these goals with a new numerical method.

1.2 Scope of the Research

The present research provides an extension of Koo and Fahrenthold [57] and Horban and Fahrenthold [44], which developed discrete energy methods for thermofluids and solid materials, respectively. The underlying formulation is used to develop a discrete Hamiltonian energy method for general electromagnetic systems. To guarantee physical continuity properties, this method uses edge and face finite elements to interpolate the state variables. The former, which have tangential continuity and allow normal discontinuities, discretizes the magnetic field intensity as generalized quasi-velocities while the latter, which have normal continuity and allow tangential discontinuities, interpolates the electric flux density as a generalized coordinate. A dual formulation, which interpolates electric field intensity and magnetic flux density by edge and face elements, respectively, is developed in Appendix A. The model incorporates internal energy variables for the modeling of thermo-electromagnetic coupling. The kinetic and potential energies of the system define the system Hamiltonian function which is used to develop the system level state space model. These equations are integrated in time by a standard Runge Kutta integration scheme. In open boundary electromagnetic problems the computational domain is truncated by an absorbing boundary condition known as an anisotropic Perfectly Matched Layer (PML) whose material parameters are represented by an anisotropic tensor in the form of the electric permittivity and the magnetic permeability. These numerical properties are included in the complex inductance and elastance matrices, which requires minimum modification of the derived Hamilton's equations. The proposed methods are validated in simulations of two and three dimensional benchmark problems with closed and open boundaries.

The transient description of discrete Hamiltonian equations derived for general electromagnetic systems is specialized to perform magnetostatic and frequency domain analysis. The equations derived in the time domain are transformed into the frequency domain and then validated by the benchmark problems with both closed and open boundary conditions. In the static case, the electric and magnetic variables become independent of each other. To guarantee divergence free conditions, in magnetostatic case a vector magnetic potential function is introduced. This method is also validated by test problems.

1.3 Dissertation Organization

The contents of this dissertation are organized as follows.

Chapter 2 details the systematic development of a new Hamiltonian formulation for a thermo-electromagnetic systems. Edge elements are used to interpolate magnetic field intensity while face elements are used to interpolate electric flux density. The use of a system dynamics approach based on a Hamiltonian technique avoids the classical numerical approaches, which are based on partial differential equations (PDE). Internal energy variables are introduced to provide a framework to couple the electromagnetic and thermal energy domains. Hamilton's equations are derived as a set of first order ordinary differential equations.

Chapter 3 outlines the development of a new discrete energy based modeling approach for general electromagnetic systems. Vector finite element basis functions are used to interpolate the state variables. First order ordinary differential equations are formulated using a Hamiltonian technique. The derived Hamilton's equations, without thermal coupling, are shown to solve model problems by comparison to exact solutions. The equations derived for thermo-electromagnetic systems show accurate results in the simulation of a one dimensional electric resistive heating problem.

Chapter 4 develops discrete equations for both frequency domain electromagnetic and magnetostatic problems. The transient formulation derived in chapter three is transformed into the frequency domain for general electromagnetic systems. In the static case, magnetic fields become independent of electric fields. Hence a magnetic vector potential is introduced to incorporate a divergence constraints into the magnetostatic equations. The developed model is validated via test problems.

Finally, chapter 5 presents conclusions of the present research and recommendations for future work.

Chapter 2

Discrete Hamiltonian Formulation for Thermo-electromagnetic Systems

2.1 Introduction

Thermo-electromagnetic systems, such as induction heating in transformers and electromagnetic actuators, exhibit different behavior when their internal temperature changes due to temperature dependent material properties. Unless certain simplifications are assumed, the interaction of the electromagnetic and thermal energy domains complicates the numerical analysis. To determine the thermal and electromagnetic field distributions for coupled thermo-electromagnetic systems, the finite difference (FD) [90] and finite element methods (FEM) [26] are widely used to solve partial differential equations.

The energy based method used in this research avoids the use of partial differential equations and directly derives a ordinary differential equations for coupled thermo-electromagnetic systems. Koo and Fahrenthold [57] and Fahrenthold and Hean [29] developed a discrete Hamiltonian description of thermo-mechanical systems. In the interest of applying discrete energy methods to thermo-electromagnetic systems, a new Hamiltonian methodology for the simulation of thermo-electromagnetic problems is developed here as an extension of previous work [44][33][81][73]. In mixed energy domain applications, a key to application of the method used here is the introduction of internal energy variable as a generalized coordinate. The present formulation includes full thermo-electromagnetic coupling, a quasi-velocity based description of nonholonomic constraints, and systematic discretization of distributed property systems.

The present chapter is organized as follows. First the continuum system of interest is discretized, by introducing edge and face type finite element interpolations. Then the Hamiltonian for the system is formulated, by writing stored energy expressions for the discretized system. Next, the evolution equations for the internal state variables are presented, the latter representing nonholonomic constraints on the system's generalized coordinates. Lagrange's multipliers are then used to couple electric, magnetic, and thermal energy domains. The canonical form of Hamilton's equations with associated constraints results in an explicit ODE model of thermo-electromagnetic systems.

2.2 Interpolation Functions

The two families of finite elements which conform in the function space of H(curl) and H(div) were introduced by Nedelec [72], they have very important properties for the numerical analysis of electromagnetic systems. The edge elements have tangential continuity but allow normal discontinuities across interfaces, whereas the face elements have normal continuity but allow tangential discontinuities across interfaces. The assignment of electric or magnetic field intensity vectors to edge elements and electric or magnetic flux density vectors to face elements is often preferred because the physical continuity requirements of the electric and magnetic field variables are then most closely matched, and the interelement boundary conditions are automatically satisfied.

Using the aforementioned desirable properties, the discretization of the modeled control volume may be performed by face and edge type finite elements [79][49]. Face basis functions are used to interpolate electric displacement, in terms of discrete generalized coordinates, while edge basis functions are used to interpolate magnetic field intensity, in terms of discrete generalized quasi-velocities as shown in figure (2.1). Internal energy is uniform in each element and is a generalized coordinate for the thermodynamic system.

2.2.1 Magnetic Field Intensity: Edge Elements

Many types of elements can be used to discretize the computational domain. In this dissertation, rectangular (quadrilateral) elements are used to solve two dimensional problems and hexahedral brick elements are used to solve three dimensional problems. The basis functions for edge elements are easily derived, for the reference element of a three dimensional hexahedron, as shown in figure (2.2). If the edge numbering scheme shown in table (2.1) is used, the edge based vector interpolation functions are written as [79][49]

$$\begin{array}{llll} \vec{\mathbf{w}}_1 = (1-y)(1-z) & \vec{\mathbf{a}}_x, & \vec{\mathbf{w}}_2 = y(1-z) & \vec{\mathbf{a}}_x \\ \vec{\mathbf{w}}_3 = (1-y)z & \vec{\mathbf{a}}_x, & \vec{\mathbf{w}}_4 = yz & \vec{\mathbf{a}}_x \\ \vec{\mathbf{w}}_5 = (1-z)(1-x) & \vec{\mathbf{a}}_y, & \vec{\mathbf{w}}_6 = z(1-x) & \vec{\mathbf{a}}_y \\ \vec{\mathbf{w}}_7 = (1-z)x & \vec{\mathbf{a}}_y, & \vec{\mathbf{w}}_8 = zx & \vec{\mathbf{a}}_y \\ \vec{\mathbf{w}}_9 = (1-x)(1-y) & \vec{\mathbf{a}}_z, & \vec{\mathbf{w}}_{10} = x(1-y) & \vec{\mathbf{a}}_z \\ \vec{\mathbf{w}}_{11} = (1-x)y & \vec{\mathbf{a}}_z, & \vec{\mathbf{w}}_{12} = xy & \vec{\mathbf{a}}_z \end{array} \tag{2.1}$$

where $\vec{\mathbf{w}}_i$ is vector interpolation function at edge 'i' on a reference element and $\vec{\mathbf{a}}_x$, $\vec{\mathbf{a}}_y$, and $\vec{\mathbf{a}}_z$ represent a set of orthogonal unit vectors in a rectangular coordinate system.

The above polynomial basis functions are used to interpolate the magnetic field intensity, chosen as a generalized velocity, and a constant tangential field value is assigned to each edge of the hexahedral element (which has 12 edges). The edge interpolation functions and associated tangential magnetic field values are written in a column vector for element 'i' as

$$\mathbf{w}^{(i)} = [\vec{\mathbf{w}}_1\ \vec{\mathbf{w}}_2\ \vec{\mathbf{w}}_3\ ...\ \vec{\mathbf{w}}_{12}]^T \tag{2.2}$$

$$\mathbf{H}^{(i)} = [H_1\ H_2\ H_3\ ...\ H_{12}]^T \tag{2.3}$$

where T denotes transpose, $\mathbf{w}^{(i)}$ is column vector of edge interpolation functions for the hexahedral element, and $\mathbf{H}^{(i)}$ is column vector of tangential magnetic field values on the edges of the 'i'th element. The magnetic field intensity for element 'i' can be expressed as [49]

$$\vec{\mathbf{H}}^{(i)} = \sum_{j=1}^{n_{es}} \vec{\mathbf{w}}_j^{(i)}\ H_j^{(i)} = \mathbf{w}^{(i)T}\ \mathbf{H}^{(i)} \tag{2.4}$$

where n_{es} is number of edges in the element, and $\vec{\mathbf{H}}^{(i)}$ is the magnetic field intensity in the 'i'th element.

2.2.2 Electric Flux Density: Face Elements

Basis functions for face elements can also be derived, for the same hexahedral element, as shown in figure (2.3). The face numbering scheme defined in table (2.2) is used here to construct vector interpolation functions denoted as [79][49]

$$\begin{array}{ll} \vec{\mathbf{f}}_1 = (-1+x) \quad \vec{\mathbf{a}}_x, & \vec{\mathbf{f}}_2 = x \quad \vec{\mathbf{a}}_x \\ \vec{\mathbf{f}}_3 = (-1+y) \quad \vec{\mathbf{a}}_y, & \vec{\mathbf{f}}_4 = y \quad \vec{\mathbf{a}}_y \\ \vec{\mathbf{f}}_5 = (-1+z) \quad \vec{\mathbf{a}}_z, & \vec{\mathbf{f}}_6 = z \quad \vec{\mathbf{a}}_z \end{array} \tag{2.5}$$

where $\mathbf{f}_i$ is the face interpolation functions for face 'i' in a reference element.

The above polynomial basis functions are used to interpolate the electric flux density, chosen as a generalized coordinate, and a constant normal field value is assigned to each face of the hexahedral element (which has 6 faces). The face interpolation functions and corresponding electric flux density values can be written in vector form for element 'i' as

$$\mathbf{f}^{(i)} = [\vec{\mathbf{f}}_1 \ \vec{\mathbf{f}}_2 \ \vec{\mathbf{f}}_3 \ ... \ \vec{\mathbf{f}}_6]^T \tag{2.6}$$

$$\mathbf{D}^{(i)} = [D_1 \ D_2 \ D_3 \ ... \ D_6]^T \tag{2.7}$$

where $\mathbf{f}^{(i)}$ is column vector of face interpolation functions in the 'i'th element and $\mathbf{D}^{(i)}$ is column vector of normal electric flux density values on the faces of the 'i'th element. The electric flux density in element 'i' is calculated as [49]

$$\vec{\mathbf{D}}^{(i)} = \sum_{j=1}^{n_{ef}} \vec{\mathbf{f}}_j^{(i)} \ D_j^{(i)} = \mathbf{f}^{(i)T} \ \mathbf{D}^{(i)} \tag{2.8}$$

where n_{ef} is number of faces in the element, and $\vec{\mathbf{D}}^{(i)}$ is the electric flux density in the 'i'th element. Note that a particular discretization method is used here for magnetic and electric state variables, but the modeling method developed in this dissertation is not limited to one interpolation method.

2.3 Magnetic Co-energy

The magnetic co-energy T^* is in general defined by

$$T^* = \frac{1}{2}\int_v \mu\, \vec{\mathbf{H}} \cdot \vec{\mathbf{H}}\, dv \tag{2.9}$$

where μ is the magnetic permeability and v is volume of interest. The generalized quasi-velocity assigned to each edge is used to a obtain discrete form of the magnetic co-energy function. Substituting equation (2.4) into equation (2.9), The magnetic co-energy can be expressed, for element 'i', as

$$T^{*(i)} = \frac{1}{2}\int_{v^{(i)}} \mu^{(i)}\, \mathbf{H}^{(i)T}\mathbf{w}^{(i)}\mathbf{w}^{(i)T}\mathbf{H}^{(i)}\, dv = \frac{1}{2}\mathbf{H}^{(i)T}\mathbf{L}^{(i)}\mathbf{H}^{(i)} \tag{2.10}$$

where

$$\mathbf{L}^{(i)} = \int_{v^{(i)}} \mu^{(i)}\mathbf{w}^{(i)}\mathbf{w}^{(i)T} dv \tag{2.11}$$

with $v^{(i)}$ the volume of element 'i', $\mu^{(i)}$ the magnetic permeability of element 'i', and $\mathbf{L}^{(i)}$ the inductance matrix for element 'i'. The system magnetic co-energy T^* is expressed as the sum of the element co-energies

$$T^* = \sum_{i=1}^{n_e} T^{*(i)} = \frac{1}{2}\sum_{i=1}^{n_e} \mathbf{H}^{(i)T}\,\mathbf{L}^{(i)}\,\mathbf{H}^{(i)} \tag{2.12}$$

where n_e is number of elements. A Boolean matrix may be introduced to relate the magnetic field vector for element 'i' to the global magnetic field vector [56][67]

$$\mathbf{H}^{(i)} = \mathbf{B}^{e(i)}\,\mathbf{H} \tag{2.13}$$

where $\mathbf{H}$ is global column vector of magnetic field intensities and $\mathbf{B}^{e(i)}$ is a Boolean matrix. Substituting equation (2.13) into equation (2.12), the system magnetic co-energy simplifies to

$$T^* = \frac{1}{2}\sum_{i=1}^{n_e} [\mathbf{B}^{e(i)}\mathbf{H}]^T\,\mathbf{L}^{(i)}\,\mathbf{B}^{e(i)}\mathbf{H} = \frac{1}{2}\,\mathbf{H}^T\,\mathbf{L}\,\mathbf{H} \tag{2.14}$$

where

$$\mathbf{L} = \sum_{i=1}^{n_e} \mathbf{B}^{e(i)T}\,\mathbf{L}^{(i)}\,\mathbf{B}^{e(i)} \tag{2.15}$$

with $\mathbf{L}$ the global inductance matrix.

From equation (2.14), the generalized magnetic momenta are defined as

$$\mathbf{P} = \frac{\partial T^*}{\partial \mathbf{H}} = \mathbf{L}\,\mathbf{H} \tag{2.16}$$

where $\mathbf{P}$ is a discrete magnetic flux variable, and represents the generalized momenta for the system.

2.4 Potential Energy

The general potential energy expression for thermo-electromagnetic systems may be written in a functional form as

$$V = V(\mathbf{D}, U) \tag{2.17}$$

where D is the electric flux density and U is the internal energy. The potential function can be decomposed into two parts

$$V = V_{electric} + V_{thermo} \tag{2.18}$$

where $V_{electric}$ is the electric potential energy and V_{thermo} is the thermal potential energy. The general electric potential energy expression for the system is

$$V_{electric} = \frac{1}{2}\int_{v} \epsilon^{-1}\, \vec{\mathbf{D}} \cdot \vec{\mathbf{D}}\, dv \tag{2.19}$$

where ϵ is the electric permittivity. Equation (2.8), which interpolates the electric flux density with face elements, allows equation (2.19) to be expressed in a discrete form, for element 'i', as

$$V^{(i)}_{electric} = \frac{1}{2}\int_{v^{(i)}} \epsilon^{(i)-1}\mathbf{D}^{(i)T}\,\mathbf{f}^{(i)}\,\mathbf{f}^{(i)T}\,\mathbf{D}^{(i)} dv = \frac{1}{2}\mathbf{D}^{(i)T}\,\mathbf{K}^{(i)}\,\mathbf{D}^{(i)} \tag{2.20}$$

where

$$\mathbf{K}^{(i)} = \int_{v^{(i)}} \epsilon^{(i)-1}\mathbf{f}^{(i)}\,\mathbf{f}^{(i)T} dv \tag{2.21}$$

with $\epsilon^{(i)}$ the electric permittivity for element 'i', and $\mathbf{K}^{(i)}$ an elastance matrix for element 'i'. The electric potential energy for the system is the sum

$$V_{electric} = \sum_{i=1}^{n_e} V^{(i)}_{electric} = \frac{1}{2}\sum_{i=1}^{n_e} \mathbf{D}^{(i)T}\,\mathbf{K}^{(i)}\,\mathbf{D}^{(i)} \tag{2.22}$$

If a Boolean matrix is introduced, equation (2.22) reduces to

$$V_{electric} = \frac{1}{2}\sum_{i=1}^{n_e} [\mathbf{B}^{f(i)}\mathbf{D}]^T\,\mathbf{K}^{(i)}\,\mathbf{B}^{f(i)}\mathbf{D} = \frac{1}{2}\,\mathbf{D}^T\,\mathbf{K}\,\mathbf{D} \tag{2.23}$$

where

$$\mathbf{D}^{(i)} = \mathbf{B}^{f(i)}\,\mathbf{D} \tag{2.24}$$

$$\mathbf{K} = \sum_{i=1}^{n_e} \mathbf{B}^{f(i)T}\,\mathbf{K}^{(i)}\,\mathbf{B}^{f(i)} \tag{2.25}$$

with $\mathbf{D}$ global column vector of electric flux densities, $\mathbf{K}$ a global elastance matrix, and $\mathbf{B}^{f(i)}$ a Boolean matrix which relates the faces in element 'i' to the faces of the system.

The thermal potential energy can be represented by the sum [33][57]

$$V_{thermo} = \sum_{i=1}^{n_e} U^{(i)} \tag{2.26}$$

where $U^{(i)}$ is internal energy for element 'i'. Equation (2.26) can be expressed as

$$V_{thermo} = \mathbf{1}^T\,\mathbf{U} \tag{2.27}$$

where $\mathbf{1}$ denotes a system level nondimensional vector, all of whose components are unity, and $\mathbf{U}$ is a system level internal energy vector. The stored energy functions define generalized conservative forces as

$$\mathbf{F} = \frac{\partial V}{\partial \mathbf{D}} = \mathbf{K}\,\mathbf{D} \tag{2.28}$$

$$\mathbf{1} = \frac{\partial V}{\partial \mathbf{U}} \tag{2.29}$$

where $\mathbf{F}$ is a discrete electric field variable, a generalized conservative force for the system.

2.5 Discrete Ampere's equation

The evolution equations for the generalized coordinates **D** can be derived from Ampere's equation, in integral form. The integral form of ampere's equation can be written as [5][45]

$$\int_S \dot{\vec{\mathbf{D}}} \cdot d\vec{S} = \oint_{\partial S} \vec{\mathbf{H}} \cdot d\vec{\ell} - \int_S \vec{\mathbf{J}} \cdot d\vec{S} \tag{2.30}$$

where $d\vec{S}$ is a differential surface area, $d\vec{\ell}$ is differential contour vector, and $\vec{\mathbf{J}}$ is an electric current density. Note that the current density and electric flux density are piecewise constant on the faces, and distributed inside the element. Similarly, magnetic field intensity is interpolated by edge elements so its value is constant on each edge. The use of edge and face interpolations allows the integral equation (2.30) to be expressed in discrete form. The discrete Ampere's equations are nonholonomic constraints, described for surface 'i' as

$$\dot{D}^{(i)} = S^{(i)-1} \oint \vec{\mathbf{H}} \cdot d\vec{\ell} - J^{(i)} = \mathbf{a}^{(i)T}\mathbf{H} - J^{(i)} \tag{2.31}$$

where 'i' is a face index, $S^{(i)}$ is the surface area of the 'i'th face, $\mathbf{a}^{(i)}$ is constant column vector, **H** is a global vector of magnetic field intensity values at the edges of the system, and $J^{(i)}$ is the electric current density on face 'i'. Equation (2.31) for the system is

$$\dot{\mathbf{D}} = \mathbf{A}\,\mathbf{H} - \mathbf{J} \tag{2.32}$$

where

$$\mathbf{D} = [D^{(1)}\, D^{(2)}\, \cdots D^{(n_f)}]^T \tag{2.33}$$

$$\mathbf{A} = [\mathbf{a}^{(1)}\, \mathbf{a}^{(2)}\, \cdots\, \mathbf{a}^{(n_f)}]^T \tag{2.34}$$

$$\mathbf{J} = [J^{(1)}\, J^{(2)}\, \cdots J^{(n_f)}]^T \tag{2.35}$$

with n_f the number of faces in the system and $\mathbf{A}$ a function of geometry.

The current density in equation (2.32) includes both conductive and impressed (excitation) currents. Therefore, it can be expressed as the sum of two different currents

$$\mathbf{J} = \mathbf{J}^c + \mathbf{J}^s(t) \tag{2.36}$$

where the superscript 's' represents an impressed current source and the superscript 'c' denotes the conduction current. In conductive materials, electric energy is dissipated through irreversible entropy production, with a conductivity that in general depends on temperature. This conversion of electromagnetic energy into thermal energy is quantified by the constitutive equation relating conductive current density and electric field intensity. The electric flux density ($\mathbf{D}$) is selected as a generalized coordinate, and interpolated by face elements, in the present numerical formulation. Hence the current flux density is piecewise constant on the faces. The constitutive relation for face 'i' is

$$J^{c(i)} = \frac{\sigma^{(i)}}{\epsilon^{(i)}} D^{(i)} \tag{2.37}$$

where $\sigma^{(i)}$ is the electric conductivity (inverse of resistivity ρ) and $\epsilon^{(i)}$ is the electric permittivity on face 'i'. They are assumed to be uniform on the faces.

The constitutive relation for the system is

$$\mathbf{J}^c = \left[J^{c(1)}\; J^{c(2)}\; \cdots\; J^{c(n_f)}\right]^T = \boldsymbol{\mathfrak{C}}^e\, \mathbf{D} \tag{2.38}$$

where $\boldsymbol{\mathfrak{C}}^e$ is a diagonal electric conductance matrix for the system which in general depends on temperature.

By substituting equations (2.36) and (2.38) into equation (2.32), the nonholonomic constraint equation for $\mathbf{D}$ is

$$\dot{\mathbf{D}} = \mathbf{A}\,\mathbf{L}^{-1}\mathbf{P} - \boldsymbol{\mathfrak{C}}^e\,\mathbf{D} - \mathbf{J}^s(t) \tag{2.39}$$

The coefficients of the generalized velocities in equation (2.39), combined with Lagrange multipliers, will determine nonconservative generalized forces in the magnetic momentum equations for thermo-electromagnetic systems, as derived in a later section.

2.6 Internal Energy Evolution Equation

Ampere's equation is an evolution equation for the electric flux density variables. Likewise a rate equation for internal energy is introduced as a nonholonomic constraint, to couple the electromagnetic energy domain with the thermal energy domain. For a thermo-electromagnetic system, internal energy evolution depends on the irreversible power production, associated with electrical dissipation (due to electric conduction) and thermal power flow (due to heat conduction). The control volume is assumed to be thermally insulated across external boundaries so that the conduction power flow into the system is not considered here. The evolution equation for the internal energy for element 'i' is [29]

$$\dot{U}^{(i)} = \dot{U}^{irr(i)} - \dot{U}^{con(i)} \tag{2.40}$$

where $\dot{U}^{irr(i)}$ is the rate of irreversible energy production associated with electric conduction and $\dot{U}^{con(i)}$ is the thermal power due to heat conduction. Total irreversible power generation due to current densities in the system is calculated by summing the products of the generalized forces and the current densities for the faces

$$\dot{U}^{irr} = \sum_{i=1}^{n_f} F_i \, J_i \tag{2.41}$$

where n_f is the number of faces in the system. Note that some faces are shared by two elements while other faces lie on external boundaries. Hence an allocated current density is introduced to distribute the power on shared faces of the elements. The power production due to the current densities for element 'i' is

$$\dot{U}^{irr(i)} = \mathbf{F}^{(i)T} \, \hat{\mathbf{J}}^{(i)} \tag{2.42}$$

where $\hat{\mathbf{J}}^{(i)}$ is the allocated current density for element 'i', defined by

$$\hat{\mathbf{J}}^{(i)} = \boldsymbol{\alpha}^{(i)} \left(\mathbf{J}^c + \mathbf{J}^s \right) = \boldsymbol{\alpha}^{(i)} \left(\mathfrak{C}^e \, \mathbf{D} + \mathbf{J}^s \right) \tag{2.43}$$

where $\boldsymbol{\alpha}^{(i)}$ is a constant allocation matrix, $\mathfrak{C}^e$ is the global electric conductance matrix, and $\mathbf{D}$ is the global column vector of electric flux density. Using the Boolean matrix defined by equation (2.24), the electric generalized force for element 'i' is

$$\mathbf{F}^{(i)} = \mathbf{B}^{f(i)}\mathbf{F} = \mathbf{B}^{f(i)}\mathbf{K}\,\mathbf{D} \tag{2.44}$$

Substituting equations (2.43) and (2.44) into equation (2.42), equation (2.42) reduces to

$$\dot{U}^{irr(i)} = [\mathbf{f}^{irr(i)}]^T \mathbf{D} + [\mathbf{f}^{sirr(i)}]^T \mathbf{J}^s(t) \tag{2.45}$$

where

$$\begin{aligned} \mathbf{f}^{irr(i)} &= \boldsymbol{\mathfrak{C}}^{eT} \boldsymbol{\alpha}^{(i)T}\, \mathbf{B}^{f(i)} \mathbf{K}\, \mathbf{D} \\ \mathbf{f}^{sirr(i)} &= \boldsymbol{\alpha}^{(i)T}\, \mathbf{B}^{f(i)} \mathbf{K}\, \mathbf{D} \end{aligned} \tag{2.46}$$

with $\mathbf{f}^{irr(i)}$ and $\mathbf{f}^{sirr(i)}$ are column vectors.

Power production due to heat conduction can be expressed for element 'i' by

$$\dot{U}^{con(i)} = \sum_{j=1}^{n_n^{(i)}} k^{(i,j)} \left(\theta^{(i)} - \theta^{(j)}\right) \tag{2.47}$$

where $n_n^{(i)}$ is the number of neighboring elements for element 'i', $\theta^{(i)}$ is the temperature for element 'i', and $k^{(i,j)}$ is the heat conduction coefficient associated with elements 'i' and 'j', taken to vary linearly with temperature

$$k^{(i,j)} = \frac{1}{2\,\ell^{(i,j)}} \left[\left(k_0 + k^{'} \theta^{(i)}\right) A^{(i)} + \left(k_0 + k^{'} \theta^{(j)}\right) A^{(j)} \right] \tag{2.48}$$

Here k_0 is the thermal conductivity at ambient temperature, $k^{'}$ is the rate of change of thermal conductivity with temperature, $\ell^{(i,j)}$ is the length between the centers of element 'i' and element 'j', and $A^{(i)}$ is the interface area for element 'i'.

Temperature can be represented either as a function of internal energy [27][29] or as a function of entropy [96]. The former constitutive relation is used in this research. Note that an entropy evolution equation can be adopted as a nonholonomic constraint in the latter case [43][56]. If the system does not undergo a phase change, internal energy can be approximated for element 'i' using

$$U^{(i)} = c_v^{(i)}\,\gamma^{(i)}\,v^{(i)}\theta^{(i)} \tag{2.49}$$

where $c_v^{(i)}$, $\gamma^{(i)}$, and $v^{(i)}$ are respectively the specific heat, mass density, and volume for element 'i'. Using equations (2.47) and (2.49), equation (2.47) becomes

$$\dot{U}^{con(i)} = \mathbf{k}^{con(i)T}\mathbf{U} \tag{2.50}$$

where $\mathbf{U}$ is a global column vector of internal energy variables and $\mathbf{k}^{con(i)}$ is column vector which depends on internal energy and hence varies with time. Using equations (2.45) and (2.50), the internal energy evolution equation for the system is

$$\dot{\mathbf{U}} = \mathbf{f}^{irr}\,\mathbf{D} - \mathbf{k}^{con}\,\mathbf{U} + \mathbf{f}^{sirr}\mathbf{J}^{s}(t) \tag{2.51}$$

where

$$\begin{aligned}
\dot{\mathbf{U}} &= [\dot{U}^{(1)}\ \dot{U}^{(2)}\ \dot{U}^{(3)}\ ...\ \dot{U}^{(n_e)}]^T \\
\mathbf{f}^{irr} &= [\mathbf{f}^{irr(1)}\ \mathbf{f}^{irr(2)}\ \mathbf{f}^{irr(3)}\ ...\ \mathbf{f}^{irr(n_e)}]^T \\
\mathbf{k}^{con} &= [\mathbf{k}^{con(1)}\ \mathbf{k}^{con(2)}\ \mathbf{k}^{con(3)}\ ...\ \mathbf{k}^{con(n_e)}]^T \\
\mathbf{f}^{sirr} &= [\mathbf{f}^{sirr(1)}\ \mathbf{f}^{sirr(2)}\ \mathbf{f}^{sirr(3)}\ ...\ \mathbf{f}^{sirr(n_e)}]^T
\end{aligned} \tag{2.52}$$

with n_e the number of elements. Equation (2.51) quantifies both heat generation due to current flow and heat flow related to heat conduction. Note that the coefficient matrices ($\mathbf{f}^{irr}$ and $\mathbf{k}^{con}$) in general depend on internal energy and hence vary with time. Like the nonholonomic constraint derived for

$\mathbf{D}$, this nonholonomic constraint, along with a Lagrange multiplier, will determine generalized forces in the Hamiltonian momentum equations. In this case, the coefficients of the generalized velocities are zero, so that the magnetic momentum equations will not include thermal generalized forces.

2.7 Discrete Hamilton's Equations for Thermo-electromagnetic Systems

The stored energy functions, constraint equations, and virtual work expressions for the system may be combined with the canonical Hamilton's equations to obtain an ordinary differential equation (ODE) model for the thermo-electromagnetic system. The system Hamiltonian(Π) for the thermo-electromagnetic system is

$$\Pi = T + V = \Pi(\mathbf{P}\,, \mathbf{D}\,, \mathbf{U}) \tag{2.53}$$

The canonical Hamilton's equations are

$$\dot{\mathbf{P}} = \mathbf{Q}^H \tag{2.54}$$

$$\mathbf{0} = -\frac{\partial \Pi}{\partial \mathbf{D}} + \mathbf{Q}^D \tag{2.55}$$

$$\mathbf{0} = -\frac{\partial \Pi}{\partial \mathbf{U}} + \mathbf{Q}^U \tag{2.56}$$

where $\mathbf{Q}^H$, $\mathbf{Q}^D$and $\mathbf{Q}^U$ are generalized forces determined by the nonholonomic constraints and the virtual work. The above equations are augmented by the evolution equations for $\mathbf{D}$ and $\mathbf{U}$, which are the nonholonomic constraints. if Lagrange multipliers $\boldsymbol{\lambda}^D$ and $\boldsymbol{\lambda}^U$ are introduced for these constraints, it follows that

$$\mathbf{Q}^H = -\mathbf{A}^{\mathbf{T}}\,\boldsymbol{\lambda}^D \tag{2.57}$$

$$\mathbf{Q}^D = \boldsymbol{\lambda}^D \tag{2.58}$$

$$\mathbf{Q}^U = \boldsymbol{\lambda}^U \tag{2.59}$$

The degenerate Hamilton's equations for the electric displacement and internal energy variables make it possible to determine in closed form the Lagrange multipliers associated with the nonholonomic constraints,

$$\boldsymbol{\lambda}^D = \frac{\partial \boldsymbol{\Pi}}{\partial \mathbf{D}} = \mathbf{K}\,\mathbf{D} \tag{2.60}$$

$$\boldsymbol{\lambda}^U = \frac{\partial \boldsymbol{\Pi}}{\partial \mathbf{U}} = \mathbf{1} \tag{2.61}$$

Equations (2.39), (2.51), and (2.54) can be combined to produce the final form of Hamilton's equations

$$\dot{\mathbf{P}} = -\mathbf{A}^T\,\mathbf{K}\,\mathbf{D} \tag{2.62}$$

$$\dot{\mathbf{D}} = \quad \mathbf{A}\,\mathbf{L}^{-1}\,\mathbf{P} - \boldsymbol{\mathfrak{C}}^e\mathbf{D} - \mathbf{J}^s(t) \tag{2.63}$$

$$\dot{\mathbf{U}} = \quad \mathbf{f}^{irr}\,\mathbf{D} - \mathbf{k}^{con}\,\mathbf{U} + \mathbf{f}^{sirr}\mathbf{J}^s(t) \tag{2.64}$$

where

$$\mathbf{P} = \mathbf{L}\mathbf{H} \tag{2.65}$$

$$\mathbf{F} = \mathbf{K}\mathbf{D} \tag{2.66}$$

The derived Hamilton's equations are explicit expressions for the time derivatives of the state variables **P**, **D**, and **U**. These ordinary differential equations can be integrated using a Runge-Kutta method. Note that the momentum balance equation is a discrete form of Faraday's law. The divergence constraint on the electric displacement is satisfied in rate form by the face interpolation, while the divergence constraint on the magnetic flux is satisfied in rate form by the use of an edge interpolation for the magnetic field intensity.

2.8 Conclusion

This chapter has developed a discrete Hamiltonian formulation of the governing equations for thermo-electromagnetic systems [35]. The derived formulation extends previous work on continuum thermo-mechanical systems [57][44][29]. This discrete energy method employs edge and face interpolations to discretize the magnetic and electric field variables. Internal energy is employed to model the thermodynamics of the system, and is used to couple the thermal and electromagnetic domains. The numerical modeling technique developed here eliminates the use of a weighted residual formulation. The approach employs a fully discrete model formulation process, and makes no reference to partial differential equations.

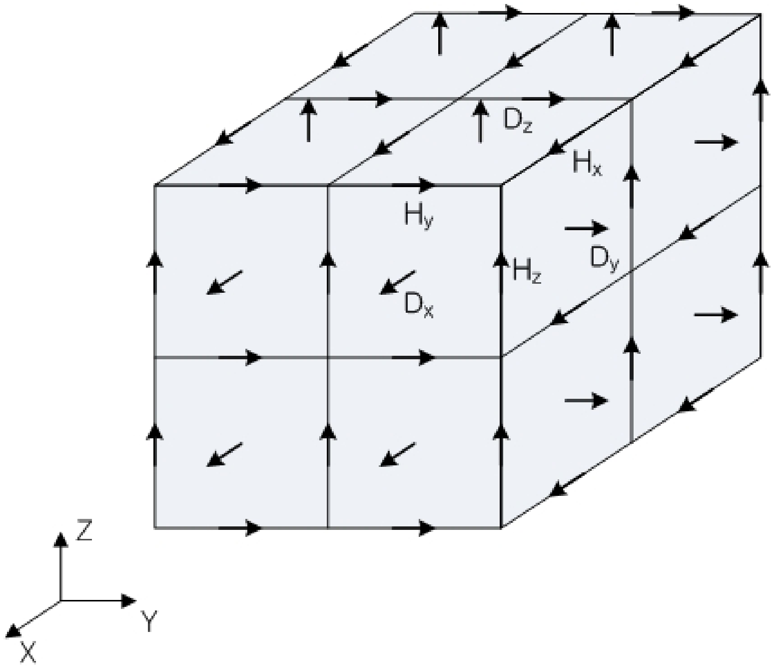

Figure 2.1: The discretization of magnetic field and electric field variables for discrete Hamiltoninan formulation

Edge number ($\mathbf{w}_i$)	1	2	3	4	5	6	7	8	9	10	11	12
Node connectivity	1-2	4-3	5-6	8-7	1-4	5-8	2-3	6-7	1-5	2-6	4-8	3-7

Table 2.1: Edge numbering scheme for a hexahedral element [79]

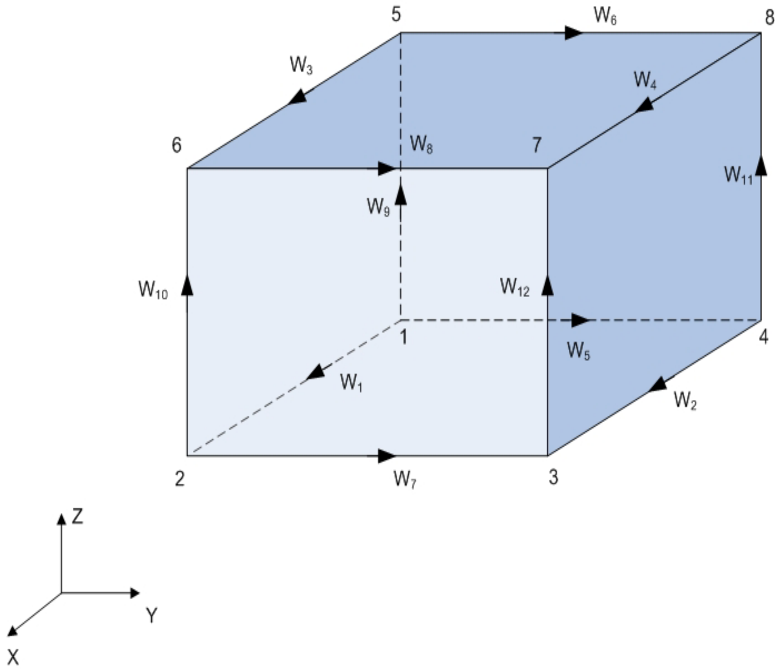

Figure 2.2: Edges in a hexahedral element [49]

Face number ($\mathbf{f}_i$)	1	2	3	4	5	6
Node connectivity	1-4-8-5	2-3-7-6	1-5-6-2	4-8-7-3	1-2-3-4	5-6-7-8

Table 2.2: Face numbering scheme for a hexahedral element [79]

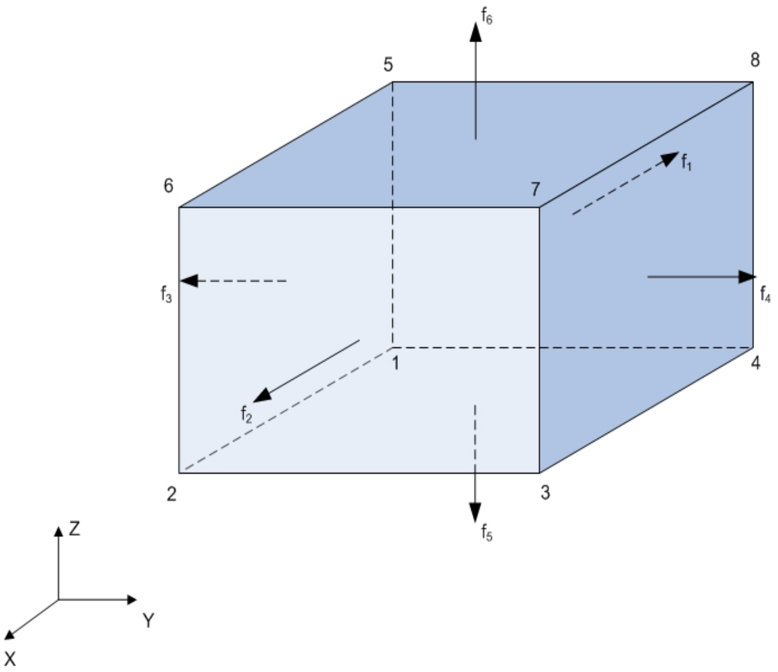

Figure 2.3: Faces in a hexahedral element

Chapter 3

Verification Problems for the Time Domain Hamiltonian Equations

3.1 Introduction

In the time domain, the electromagnetic systems are described by Maxwell's equations or the vector Helmholtz equations for the electric and magnetic fields. However, many real world electromagnetic problems including scattering, radiation, waveguide analysis, etc., may not be solved analytically, and require numerical solution techniques. Finite difference time domain (FDTD) methods are most often used for computational electromagnetic problems in the time domain, in spite of their geometric limitations [101][89][100]. Nodal finite element methods are usually limited to static problems, due to nonphysical solutions associated with spurious modes [13][87]. Vector finite element methods (VFEM) are gaining favor within the computational electromagnetic community as an effective and efficient approach to solve electromagnetic problems [72][14][60]. They discretize the problem domain using either edge elements or both edge and face elements. The former basis functions have been extensively used to formulate finite element solutions of the vector Helmholtz equations [64][65][61]. The latter approach has been proposed to convert the weak form of Maxwell's equations into a coupled system of ordinary differential equations, using edge elements as a basis for the electric field and face elements as a basis for the magnetic flux density [69][**?**].

Many practical electromagnetic problems involve electromagnetic wave propagation or scattering into unbounded regions. The accurate and efficient numerical solution of problems in unbounded regions has been a great challenge in the computational electromagnetics community. Among many boundary conditions proposed to truncate computational domain, the perfectly matched layer (PML) method has been most successfully employed for electromagnetic problems. It was first introduced by Berenger [7][9]. It creates a reflectionless nonphysical absorber adjacent to the outer grid boundaries, to truncate the computational domain. This method is discussed by many papers [7][9][22][80]. These formulations have been successfully used for FDTD methods [34][52][93], the frequency domain finite element methods [98][58], and the time domain finite element methods [47][48]. Here an anisotropic PML [80][34][89], in which complex permeability and permittivity tensors are used to model the propagating wave, is adopted to solve open boundary condition problems. This method can be applied with a minimum of model modifications (these numerical properties can be implemented as constitutive equations, and result in additional evolution equations in the PML regions.)

The first five sections of this chapter describe the interpolation functions, magnetic and internal energy expressions, constraint equations, numerical damping, and virtual work for general electromagnetic systems. The chapter then constructs an appropriate form of Maxwell's equations, by employing a discrete energy method. It avoids the introduction of a variational functional, based on partial differential equations (PDE). It employs an anisotropic PML which truncates the computational domain, so that the interface between the absorbing PML material and free space is reflectionless for all frequencies, polarizations, and angles of incidence, with the proper choice of material properties. The numerical model is validated via benchmark problems with closed, open, or mixed boundary conditions. The discrete Hamiltonian formulation derived in the preceding chapter for thermo-electromagnetic systems is validated by solving a one dimensional thermo-electromagnetic diffusion problem.

3.2 Discrete Hamilton's Equations for Electromagnetic Problems in Time Domain

3.2.1 Interpolation

Discretization of the modeled control volume is performed using edge and face type finite elements [79][49]. Edge basis functions are used to interpolate the magnetic field intensity, in terms of discrete generalized velocities, while face basis functions are used to interpolate the electric flux density, in terms of discrete generalized coordinates.

3.2.2 Magnetic Co-energy and Electric Potential Energy

The edge and face interpolations allow the magnetic co-energy and the electric potential energy functions to be expressed in discrete form. They were described in the previous chapter and can be summarized in the functional form

$$T^* = T^*(\mathbf{H}) \tag{3.1}$$

$$V = V(\mathbf{D}) \tag{3.2}$$

These functions define generalized magnetic momenta and generalized electric conservative forces for the system as

$$\mathbf{P} = \frac{\partial T^*}{\partial \mathbf{H}} \tag{3.3}$$

$$\mathbf{F} = \frac{\partial V}{\partial \mathbf{D}} \tag{3.4}$$

where **P** is global column vector of discrete magnetic flux variables (magnetic momenta) and **F** is global column vector of discrete electric field variables (generalized conservative forces). Note that there are no generalized coordinates associated with the generalized velocities **H**, which are generalized quasi-velocities, since their integrals with respect to time do not constitute coordinates which may be used to define physically meaningful potential energy functions. There are no generalized momenta associated with the generalized coordinates **D**.

3.2.3 Evolution Equation: Discrete Ampere's Equation

The discrete evolution equation (2.39) for electric flux density, a generalized coordinate, was derived using the integral form of Ampere's equation in chapter 2. It serves as a nonholonomic constraint in the system level Hamiltonian model

$$\dot{\mathbf{D}} = \mathbf{A}\,\mathbf{L}^{-1}\mathbf{P} - \mathfrak{C}^e\,\mathbf{D} - \mathbf{J}^s(t) \tag{3.5}$$

where $\mathbf{A}$ is a matrix that depends on the geometry, $\mathbf{L}$ is the magnetic inductance matrix, and $\mathfrak{C}^e$ is electric conductance matrix.

3.2.4 Numerical Damping: Magnetic Conduction

Magnetic conductance is a nonphysical property, however it is sometimes introduced, as a dual of electric conductance, to implement absorbing boundary conditions for infinite boundary electromagnetic problems. Therefore, it will be considered here to be a numerical damping. Viscous damping forces, which are associated with generalized velocities, are considered nonconservative generalized forces. In mechanical systems, Rayleigh's dissipation function is often introduced to derive the dissipation forces for Lagrangian or Hamiltonian formulations [37][68]. Here Rayleigh's function (Q^m) can be expressed as

$$Q^m = \frac{1}{2}\int_v \sigma^m \vec{\mathbf{H}} \cdot \vec{\mathbf{H}}\, dv \tag{3.6}$$

where σ^m is magnetic conductivity. Edge interpolation functions are used to interpolate the magnetic field intensity. Substituting equation (2.4) into equation (3.6), the discrete form of equation (3.6) is obtained as the sum of the element dissipation functions

$$Q^m = \sum_{i=1}^{n_e} Q^{m(i)} = \frac{1}{2}\sum_{i=1}^{n_e} \mathbf{H}^{(i)T}\, \mathfrak{R}^{m(i)}\, \mathbf{H}^{(i)} \tag{3.7}$$

where the index n_e is the number of elements, $\mathbf{H}^{(i)}$ is the vector of the tangential magnetic intensity values on the edges of the 'i'th element, and T denotes the transpose. $\mathfrak{R}^{m(i)}$ is an element level magnetic resistance matrix, and is defined as

$$\boldsymbol{\mathcal{R}}^{m(i)} = \int_{v_e} \sigma^{m(i)}\, \mathbf{w}^{(i)}\, \mathbf{w}^{(i)T}\, dv \tag{3.8}$$

where $\mathbf{w}^{(i)}$ is the vector of edge interpolation functions for the 'i'th element. Equation (3.7) reduces, in global matrix form, to

$$Q^m = \frac{1}{2}\,\mathbf{H}^T\, \boldsymbol{\mathcal{R}}^m\, \mathbf{H} \tag{3.9}$$

where

$$\boldsymbol{\mathcal{R}}^m = \sum_{i=1}^{n_e} \mathbf{B}^{e(i)T}\, \boldsymbol{\mathcal{R}}^{m(i)}\, \mathbf{B}^{e(i)} \tag{3.10}$$

with $\mathbf{B}^{e(i)}$ the Boolean matrix defined in equation (2.13), $\mathbf{H}$ a global vector of magnetic field intensities, and $\boldsymbol{\mathcal{R}}^m$ a global magnetic resistance matrix.

Therefore, the dissipation force associated with magnetic conduction can be defined as

$$\mathbf{f}^m = \frac{\partial Q^m}{\partial \mathbf{H}} = \boldsymbol{\mathcal{R}}^m\, \mathbf{H} \tag{3.11}$$

and will be included in Hamilton's equations.

3.2.5 Virtual Work

Magnetic field intensities are used as quasi-velocities and discretized by edge interpolation functions. Hence they can be related to the generalized quasi-coordinates by

$$H_i = \dot{q}_i^m \qquad (i = 1, 2, \cdots n_s) \tag{3.12}$$

where n_s is number of edges in the system. The virtual work is due to the interaction of the computational control volume with the external environment and depends on sources imposed on external boundary surfaces. The nonconservative power associated with electric sources is

$$P^{nc} = -\int_S [\vec{\mathbf{E}}^s(\vec{\mathbf{x}}, t) \times \vec{\mathbf{H}}] \cdot \vec{\mathbf{n}} dS \tag{3.13}$$

where $\vec{\mathbf{E}}^s(\vec{\mathbf{x}}, t)$ is the electric source and depends on space and time, S is the surface bounding the element, and $\vec{\mathbf{n}}$ is the outward vector normal to the surface S.

The virtual work due to electric sources imposed on boundary surfaces depends on a virtual change of the generalized quasi-coordinates. Using the vector identity,

$$(\vec{\mathbf{a}} \times \vec{\mathbf{b}}) \cdot \vec{\mathbf{c}} = (\vec{\mathbf{c}} \times \vec{\mathbf{a}}) \cdot \vec{\mathbf{b}} \tag{3.14}$$

the virtual work in the system can be written from equation (3.13) as

$$\delta W = \sum_{i=1}^{n_e} \delta W^{(i)} \tag{3.15}$$

where

$$\delta W^{(i)} = -\int_{S^{(i)}} [\vec{\mathbf{n}} \times \vec{\mathbf{E}}^s(\vec{\mathbf{x}}, t)] \cdot \delta\vec{\mathbf{q}}^{m(i)}\, dS \tag{3.16}$$

with n_e number of elements, $S^{(i)}$ the total surface bounding element 'i', and $\delta\vec{\mathbf{q}}^{m(i)}$ the virtual change of the generalized quasi-coordinate for element 'i'. The latter are interpolated in the same manner as the magnetic field intensity, and can be written for element 'i' as

$$\delta\vec{\mathbf{q}}^{m(i)} = \mathbf{w}^{(i)T} \delta\mathbf{q}^{m(i)} \tag{3.17}$$

where $\mathbf{w}^{(i)}$ is the vector of the edge interpolation functions for the element 'i' (a function of space). Substituting equation (3.17) into equation (3.16), the virtual work is obtained for element 'i' as

$$\delta W^{(i)} = \mathbf{Q}^{(i)T} \delta \mathbf{q}^{m(i)} \tag{3.18}$$

where

$$\mathbf{Q}^{(i)} = -\int_{S^{(i)}} [\vec{\mathbf{n}} \times \vec{\mathbf{E}}^{s}(\vec{\mathbf{x}}, t)] \cdot \mathbf{w}^{(i)} \, dS \tag{3.19}$$

The virtual work for the system can be expressed as the sum

$$\delta W = \sum_{i=1}^{n_e} \mathbf{Q}^{(i)T} \delta \mathbf{q}^{m(i)} = \sum_{i=1}^{n_e} \mathbf{Q}^{(i)T} [\mathbf{B}^{e(i)} \delta \mathbf{q}^{m}] \tag{3.20}$$

where $\mathbf{B}^{e(i)}$ is the Boolean matrix defined in equation (2.13), and $\delta \mathbf{q}^{m}$ denotes a virtual change of the quasi-coordinates for the system. The generalized forces conjugate to the global quasi-coordinates in equation (3.20), are defined by

$$\delta W = [\mathbf{f}^{s}]^{T} \, \delta \mathbf{q}^{m} \tag{3.21}$$

where $\mathbf{f}^{s}$ is the global force vector

$$\mathbf{f}^{s} = \sum_{i=1}^{n_e} \mathbf{B}^{e(i)T} \, \mathbf{Q}^{(i)} \tag{3.22}$$

3.2.6 Discrete Hamilton's Equations for Electromagnetic Systems

The stored energy functions define the system Hamiltonian, which is combined with the constraint equations, the dissipation function, and the virtual work expression for the system to obtain Hamilton's equations. The result is a state space description of the electrodynamic system. The system Hamiltonian(Π) is

$$\Pi = T + V = \Pi(\mathbf{P},\, \mathbf{D}) \tag{3.23}$$

and the canonical Hamilton's equations are

$$\dot{\mathbf{P}} = \quad \mathbf{Q}^H \tag{3.24}$$

$$\mathbf{0} = -\frac{\partial \Pi}{\partial \mathbf{D}} + \mathbf{Q}^D \tag{3.25}$$

where $\mathbf{Q}^H$ and $\mathbf{Q}^D$ are the generalized nonconservative forces determined by the nonholonomic constraints, Rayleigh's dissipation function, and the virtual work. Hamilton's equations take a degenerate form since there are no generalized coordinates associated with the magnetic field intensities and no generalized momenta associated with the electric flux densities. This makes it possible to determine in closed form the Lagrange multipliers associated with the nonholonomic constraints. Introducing a Lagrange multiplier ($\boldsymbol{\lambda}^D$) for the nonholonomic constraint equation (3.5) results in

$$\mathbf{Q}^H = -\mathbf{A}^{\mathbf{T}}\,\boldsymbol{\lambda}^D - \mathbf{f}^m + \mathbf{f}^s(t) \tag{3.26}$$

$$\mathbf{Q}^D = \boldsymbol{\lambda}^D \tag{3.27}$$

The degenerate Hamilton's equation (3.25) determines in closed form the Lagrange multiplier. The above equations are augmented by the evolution equation (3.5) to produce a complete set of ODE equations for the electromagnetic system. The final form of the discrete Hamilton's equations is

$$\dot{\mathbf{P}} = -\mathbf{A}^T \mathbf{K}\,\mathbf{D} - \mathfrak{R}^m \mathbf{L}^{-1}\mathbf{P} + \mathbf{f}^s(t) \tag{3.28}$$

$$\dot{\mathbf{D}} = \quad \mathbf{A}\,\mathbf{L}^{-1}\,\mathbf{P} \; - \mathfrak{C}^e\,\mathbf{D} - \mathbf{J}^s(t) \tag{3.29}$$

where the constitutive relations are

$$\mathbf{P} = \mathbf{L}\,\mathbf{H} \tag{3.30}$$

$$\mathbf{F} = \mathbf{K}\,\mathbf{D} \tag{3.31}$$

Note that the magnetic momentum balance equation is equivalent to a discrete form of Faraday's law. The divergence constraint on the electric displacement is satisfied in rate form by the face interpolation, while the divergence constraint on the magnetic flux is satisfied in rate form by the use of an edge interpolation for the magnetic field intensity.

3.2.7 Open Boundary Conditions

Infinite boundary condition problems are very important in computational electromagnetics. To limit computational resources, the computational grid should be truncated in some way, absorbing the outgoing waves without introducing significant artifacts into the computation. Berenger [7][9] introduced the Perfectly Matched Layer (PML) as an absorbing boundary condition for infinite domain problems. It has been successfully applied to various computational electromagnetic methods, including finite difference time domain methods (FDTD) and finite element methods. The basic idea is that an absorbing layer is placed adjacent to the edges of computational region, which absorbs outgoing waves without reflections from the edge of the absorber. Several equivalent formulations of PML have been developed. Among them, the uniaxial anisotropic PML is widely used, since a non-physical and rather cumbersome split field notation can be avoided.

3.2.7.1 Review of Anisotropic Perfectly Matched Layer (PML)

This section reviews the theoretical basis of the anisotropic perfectly matched layer (anisotropic PML). The review is based on references [80][98]. A plane wave incidence problem is usually used to mathematically develop the permeability and permittivity tensors of a reflectionless anisotropic absorbing material, referred to as anisotropic PML [80][98][36]. A plane wave incidence on the interface ($x = 0$) is considered here. It is propagating from a half space of an isotropic homogeneous medium to a half space of a uniaxial anisotropic PML medium, as shown in figure (3.1). The main benefit of this method is that the interface does not reflect a wave back into the computation domain, for all frequencies, all angles of incidence, and all polarizations. This absorbing effect can be achieved by a layer of uniaxial anisotropic lossy material whose permittivity ($\bar{\bar{\boldsymbol{\epsilon}}}_2$) and permeability ($\bar{\bar{\boldsymbol{\mu}}}_2$) may be represented in tensor form as

$$\begin{aligned}
\bar{\bar{\boldsymbol{\mu}}}_2 &= \begin{bmatrix} \mu_x + \frac{\sigma_x^m}{j\omega} & 0 & 0 \\ 0 & \mu_y + \frac{\sigma_y^m}{j\omega} & 0 \\ 0 & 0 & \mu_z + \frac{\sigma_z^m}{j\omega} \end{bmatrix} \\
\bar{\bar{\boldsymbol{\epsilon}}}_2 &= \begin{bmatrix} \epsilon_x + \frac{\sigma_x^e}{j\omega} & 0 & 0 \\ 0 & \epsilon_y + \frac{\sigma_y^e}{j\omega} & 0 \\ 0 & 0 & \epsilon_z + \frac{\sigma_z^e}{j\omega} \end{bmatrix}
\end{aligned} \tag{3.32}$$

where μ_ξ $(\xi = x,\ y$ and $z)$ is magnetic permeability, ϵ_ξ is electric permittivity, and σ_ξ^m and σ_ξ^e are magnetic and electric conductivity, respectively. The intrinsic impedance of the absorbing medium should be matched to that of the isotropic medium in the left half space, which requires the condition

$$\frac{\overline{\overline{\boldsymbol{\epsilon}}}_2}{\epsilon_1} = \frac{\overline{\overline{\boldsymbol{\mu}}}_2}{\mu_1} \tag{3.33}$$

where ϵ_1 and μ_1 are the permittivity and permeability of the isotropic medium in the left half space. Then, equation (3.32) can be simplified by

$$\begin{aligned} \overline{\overline{\boldsymbol{\epsilon}}}_2 &= \epsilon_1 \begin{bmatrix} a & 0 & 0 \\ 0 & b & 0 \\ 0 & 0 & c \end{bmatrix} \\ \overline{\overline{\boldsymbol{\mu}}}_2 &= \mu_1 \begin{bmatrix} a & 0 & 0 \\ 0 & b & 0 \\ 0 & 0 & c \end{bmatrix} \end{aligned} \tag{3.34}$$

where a, b, and c are in general complex.

An arbitrarily polarized plane wave, $\vec{\mathbf{H}} = \vec{\mathbf{H}}_0\ e^{-j\vec{\boldsymbol{\beta}}_2 \cdot \vec{\mathbf{x}}}$, is assumed to be propagating in an uniaxial anisotropic medium having the permittivity and permeability tensors given in equation (3.34). The fields excited within anisotropic PML region are governed by the wave equation

$$\vec{\boldsymbol{\beta}}_2 \times \overline{\overline{\boldsymbol{\epsilon}}}_2^{-1} \left[\vec{\boldsymbol{\beta}}_2 \times \vec{\mathbf{H}} \right] + \omega^2 \overline{\overline{\boldsymbol{\mu}}}_2 \vec{\mathbf{H}} = 0 \tag{3.35}$$

where $\vec{\boldsymbol{\beta}}_2 = \beta_{2x}\ \vec{\mathbf{a}}_x + \beta_{2y}\ \vec{\mathbf{a}}_y$, is a constant vector in the anisotropic medium and is confined to xy-plane. By expressing the cross product using matrix operators, the wave equation (3.35) can be written in matrix form as

$$\begin{bmatrix} k_1^2 - a^{-1}c^{-1}\beta_{2y}^2 & a^{-1}c^{-1}\beta_{2x}\beta_{2y} & 0 \\ b^{-1}c^{-1}\beta_{2x}\beta_{2y} & k_1^2 - b^{-1}c^{-1}\beta_{2x}^2 & 0 \\ 0 & 0 & k_1^2 - b^{-1}c^{-1}\beta_{2x}^2 - a^{-1}c^{-1}\beta_{2y}^2 \end{bmatrix} \begin{bmatrix} H_x \\ H_y \\ H_z \end{bmatrix} = 0 \tag{3.36}$$

where $k_1^2 = \omega^2\mu_1\epsilon_1$. The dispersion relation for the anisotropic PML medium is derived by setting the determinant of the coefficient matrix to zero. The eigenmode solutions can be decoupled into TE$_z$ and TM$_z$ modes. The dispersion relations for these two modes are the same and are

$$k_1^2 - b^{-1}c^{-1}\beta_{2x}^2 - a^{-1}c^{-1}\beta_{2y}^2 = 0 \tag{3.37}$$

Next, the reflection coefficient is computed at the interface. Since any arbitrarily polarized plane wave can be divided into a sum of TE$_z$ and TM$_z$ modes, the coefficients of reflection and transmission are separately calculated for the TE$_z$ and TM$_z$ modes. First, the fields are calculated for the TE$_z$ case. In the left half space of figure (3.1), they are

$$\begin{aligned} \vec{\mathbf{H}}_1 &= H_0(1 + \Gamma e^{2j\beta_{1x}x})\, e^{-j\beta_{1x}x - j\beta_{1y}y} \quad \vec{\mathbf{a}}_z \\ \vec{\mathbf{E}}_1 &= H_0\left[-\frac{\beta_{1y}}{\omega\epsilon_1}(1 + \Gamma e^{2j\beta_{1x}x})\,\vec{\mathbf{a}}_x + \frac{\beta_{1x}}{\omega\epsilon_1}(1 - \Gamma e^{2j\beta_{1x}x})\,\vec{\mathbf{a}}_y\right]\, e^{-j\beta_{1x}x - j\beta_{1y}y} \end{aligned} \tag{3.38}$$

where H_0 is the magnitude of the magnetic plane wave, Γ is a reflection coefficient and $\vec{\mathbf{a}}_x$, $\vec{\mathbf{a}}_y$, and $\vec{\mathbf{a}}_z$ represent a set of orthogonal unit vectors in a rectangular coordinate system. In the right half space of figure (3.1), the fields transmitted into anisotropic PML medium are

$$\begin{aligned} \vec{\mathbf{H}}_2 &= H_0\tau e^{-j\beta_{2x}x - j\beta_{2y}y} \quad \vec{\mathbf{a}}_z \\ \vec{\mathbf{E}}_2 &= H_0\tau\left(-\frac{\beta_{2y}}{\omega\epsilon_1 a}\,\vec{\mathbf{a}}_x + \frac{\beta_{2x}}{\omega\epsilon_1 b}\,\vec{\mathbf{a}}_y\right)\, e^{-j\beta_{2x}x - j\beta_{2y}y} \end{aligned} \tag{3.39}$$

where τ is a transmission coefficient. From equations (3.38) and (3.39), the phase matching condition at the interface ($x = 0$) requires

$$\beta_{1y} = \beta_{2y} \tag{3.40}$$

The magnitude matching condition results in the determination of the reflection coefficient at the interface

$$\Gamma = \frac{\beta_{1x} - b^{-1}\beta_{2x}}{\beta_{1x} + b^{-1}\beta_{2x}} \tag{3.41}$$

Therefore, from equation (3.41), reflectionless condition ($\Gamma = 0$) is

$$\beta_{2x} = b\,\beta_{1x} \tag{3.42}$$

Substituting equations (3.40) and (3.42) into the dispersion relation yields

$$\beta_1^2 - bc^{-1}\beta_{1x}^2 - a^{-1}c^{-1}\beta_{1y}^2 = 0 \tag{3.43}$$

If we choose $a = c^{-1}$ and $b = c$, the dispersion condition is satisfied for a plane wave incident on the uniaxial anisotropic lossy medium. The preceding analysis can be repeated for a TM$_z$ polarized wave; the reflectionless condition for the TM$_z$ wave is the same as in equation (3.42). It is concluded that a plane wave incident on the uniaxial anisotropic PML medium can be completely transmitted into the absorbing medium, without any reflection, regardless of incident angle, frequency and polarization, if we choose $c = \left(1 + \frac{\sigma_2}{j\omega\epsilon_1}\right)$, $a = c^{-1}$ and $b = c$. The permeability and permittivity tensors are then

$$\bar{\bar{\epsilon}}_2 = \epsilon_1 \begin{bmatrix} (1 + \frac{\sigma_2}{j\omega\epsilon_1})^{-1} & 0 & 0 \\ 0 & 1 + \frac{\sigma_2}{j\omega\epsilon_1} & 0 \\ 0 & 0 & 1 + \frac{\sigma_2}{j\omega\epsilon_1} \end{bmatrix} \tag{3.44}$$

$$\overline{\overline{\mu}}_2 = \mu_1 \begin{bmatrix} (1+\frac{\sigma_2}{j\omega\epsilon_1})^{-1} & 0 & 0 \\ 0 & 1+\frac{\sigma_2}{j\omega\epsilon_1} & 0 \\ 0 & 0 & 1+\frac{\sigma_2}{j\omega\epsilon_1} \end{bmatrix} \tag{3.45}$$

where σ_2 is conductivity in the anisotropic PML. Note that uniaxial anisotropic materials have no off-diagonal components.

3.2.7.2 Application of Anisotropic PML to Discrete Hamilton's Equations for Electromagnetic Systems

An implementation of the anisotropic PML is developed in this section. In order to apply an anisotropic PML, represented in tensor form using the complex permittivity (3.44) and permeability (3.45), the inductance (2.11) and elastance (2.21) matrices must be modified. This section defines the complex form of the inductance and elastance matrices, for an isotropic homogeneous medium, to be used to model isotropic lossy dielectric materials. It then develops these matrices for a uniaxial anisotropic medium, to implement the anisotropic PML formulation. The complex inductance matrix for element '*i*' can be defined for isotropic media as

$$\mathbf{L}^{*(i)} = \int_{V_e} \mu^{*(i)}\, \mathbf{w}^{(i)}\, \mathbf{w}^{(i)T}\, dV \tag{3.46}$$

where $\mathbf{w}^{(i)}$ denotes column vector of edge interpolation functions for element '*i*' and $\mu^{*(i)}$ represents a complex magnetic permeability

$$\mu^{*(i)} = \mu^{(i)} + \frac{\sigma^{m(i)}}{j\omega} \tag{3.47}$$

where ω is a frequency, j denotes $\sqrt{-1}$, $\mu^{(i)}$ is a magnetic permeability, and $\sigma^{m(i)}$ is a magnetic conductivity (both assumed to be homogeneous for the element). To relate equation (3.46) and equation (2.11), note that

$$\mathbf{L}^{*(i)} = (1 + \frac{\sigma^m}{j\omega\mu})\, \mathbf{L}^{(i)} \tag{3.48}$$

where $\mathbf{L}^{(i)}$ is the element inductance matrix in equation (2.11). Likewise, the complex elastance matrix can be defined as

$$\mathbf{K}^{*(i)} = \int_{V_e} \epsilon^{*(i)-1}\, \mathbf{f}^{(i)}\, \mathbf{f}^{(i)T}\, dV \tag{3.49}$$

where $\mathbf{f}^{(i)}$ is column vector of face interpolation functions for the 'i'th element and $\epsilon^{*(i)}$ is a complex electric permittivity for element 'i' denoted by

$$\epsilon^{*(i)} = \epsilon^{(i)} + \frac{\sigma^{e(i)}}{j\omega} \tag{3.50}$$

Here $\epsilon^{(i)}$ is the electric permittivity and $\sigma^{e(i)}$ is the electric conductivity for element 'i', assumed to be a uniform over the element. Substituting equation (3.50) into equation (3.49),

$$\mathbf{K}^{*(i)} = (1 + \frac{\sigma^e}{j\omega\epsilon})^{-1}\, \mathbf{K}^{(i)} \tag{3.51}$$

In a uniaxial anisotropic medium, material properties depend on direction and are usually written in tensor form. Anisotropic PML requires the developed Hamilton's formulation to incorporate a tensor form, so that the formulation in equations (3.44) and (3.45) can be implemented. Using equation (2.11), the complex inductance matrix is defined for element 'i' as

$$\mathbf{L}^{*(i)} = \int_{V_e} \overline{\overline{\boldsymbol{\mu}}}^{(i)}\, \mathbf{w}^{(i)}\, \mathbf{w}^{(i)T}\, dV \tag{3.52}$$

where $\overline{\overline{\boldsymbol{\mu}}}^{(i)}$ is a magnetic permeability matrix for the 'i'th element. It can be represented in tensor form as

$$\overline{\overline{\boldsymbol{\mu}}}^{(i)} = \begin{bmatrix} \overline{\overline{\boldsymbol{\mu}}}_x & \mathbf{0} & \mathbf{0} \\ \mathbf{0} & \overline{\overline{\boldsymbol{\mu}}}_y & \mathbf{0} \\ \mathbf{0} & \mathbf{0} & \overline{\overline{\boldsymbol{\mu}}}_z \end{bmatrix} \tag{3.53}$$

where $\overline{\overline{\boldsymbol{\mu}}}_\xi$, ($\xi$ = x, y, and z), are the magnetic permeability matrices in the three directions

$$\overline{\overline{\boldsymbol{\mu}}}_\xi = \begin{bmatrix} \mu_\xi + \frac{\sigma_\xi^m}{j\omega} & 0 & 0 & 0 \\ 0 & \mu_\xi + \frac{\sigma_\xi^m}{j\omega} & 0 & 0 \\ 0 & 0 & \mu_\xi + \frac{\sigma_\xi^m}{j\omega} & 0 \\ 0 & 0 & 0 & \mu_\xi + \frac{\sigma_\xi^m}{j\omega} \end{bmatrix} = \left(\mu_\xi + \frac{\sigma_\xi^m}{j\omega}\right)\mathbf{I}^e \tag{3.54}$$

with ω a frequency, σ_ξ^m the magnetic conductivity, μ_ξ the magnetic permeability in the ξ-direction, and $\mathbf{I}^e$ a 4×4 identity matrix. In this dissertation, hexahedral brick elements (figure (2.2)) are used to discretize the computational domain. This element incorporates four x-directional edges, four y-directional edges, and four z-directional edges. If the edges are numbered as in table (2.1), the inductance matrix can be partitioned into three 4×4 block matrices which refer to the x, y, and z directional edges. The off diagonal blocks are zero, since their components are calculated using the inner product of edge interpolation functions. Using equations (3.53) and (3.54), equation (3.52) is written for element 'i' as

$$\mathbf{L}^{*(i)} = \begin{bmatrix} \left(1 + \frac{\sigma_x^m}{j\omega\mu_x}\right)\mathbf{I}^e & \mathbf{0} & \mathbf{0} \\ \mathbf{0} & \left(1 + \frac{\sigma_y^m}{j\omega\mu_y}\right)\mathbf{I}^e & \mathbf{0} \\ \mathbf{0} & \mathbf{0} & \left(1 + \frac{\sigma_z^m}{j\omega\mu_z}\right)\mathbf{I}^e \end{bmatrix} \begin{bmatrix} \mathbf{L}_x^{(i)} & \mathbf{0} & \mathbf{0} \\ \mathbf{0} & \mathbf{L}_y^{(i)} & \mathbf{0} \\ \mathbf{0} & \mathbf{0} & \mathbf{L}_z^{(i)} \end{bmatrix} \tag{3.55}$$

where $\mathbf{L}_\xi^{*(i)}$ denotes the complex magnetic inductance matrix associated with the ξ-directional edges for element 'i'. Using the Boolean matrix defined in equation (2.13), equation (3.55) is written for the system as

$$\mathbf{L}^* = \sum_{i=1}^{n_e} \mathbf{B}^{e(i)T}\, \mathbf{L}^{*(i)}\, \mathbf{B}^{e(i)} \tag{3.56}$$

Hence the constitutive equation (3.30) can be expressed for the system as

$$\mathbf{P} = \mathbf{L}^*\,\mathbf{H} = \begin{bmatrix} \left(1+\frac{\sigma_x^m}{j\omega\mu_x}\right)\mathbf{L}_x & \mathbf{0} & \mathbf{0} \\ \mathbf{0} & \left(1+\frac{\sigma_y^m}{j\omega\mu_y}\right)\mathbf{L}_y & \mathbf{0} \\ \mathbf{0} & \mathbf{0} & \left(1+\frac{\sigma_z^m}{j\omega\mu_z}\right)\mathbf{L}_z \end{bmatrix} \begin{bmatrix} \mathbf{H}_x \\ \mathbf{H}_y \\ \mathbf{H}_z \end{bmatrix} \tag{3.57}$$

where $\mathbf{L}^*$ is the global complex elastance matrix and $\mathbf{L}_\xi$ denotes a partition of the magnetic inductance matrix, associated with the ξ-directional edges for the system.

From equation (2.21), the complex elastance matrix can be similarly expressed for element 'i' as

$$\mathbf{K}^{*(i)} = \int_{V_e} \overline{\overline{\boldsymbol{\epsilon}}}^{(i)-1}\, \mathbf{f}^{(i)}\, \mathbf{f}^{(i)T}\, dV \tag{3.58}$$

where $\overline{\overline{\boldsymbol{\epsilon}}}$ is a electric permittivity tensor. It is expressed in tensor form using

$$\overline{\overline{\boldsymbol{\epsilon}}}^{(i)} = \begin{bmatrix} \overline{\overline{\boldsymbol{\epsilon}}}_x & \mathbf{0} & \mathbf{0} \\ \mathbf{0} & \overline{\overline{\boldsymbol{\epsilon}}}_y & \mathbf{0} \\ \mathbf{0} & \mathbf{0} & \overline{\overline{\boldsymbol{\epsilon}}}_z \end{bmatrix} \tag{3.59}$$

where $\overline{\overline{\boldsymbol{\epsilon}}}_\xi$, ($\xi$ = x, y, and z), is the permittivity matrix for the ξ-direction

$$\overline{\overline{\boldsymbol{\epsilon}}}_\xi = \begin{bmatrix} \epsilon_\xi + \frac{\sigma_\xi^e}{j\omega} & 0 \\ 0 & \epsilon_\xi + \frac{\sigma_\xi^e}{j\omega} \end{bmatrix} = \left(\epsilon_\xi + \frac{\sigma_\xi^e}{j\omega}\right)\mathbf{I}^f \tag{3.60}$$

with σ_ξ^e the electric conductivity and ϵ_ξ the electric permittivity in the ξ-direction, and $\mathbf{I}^f$ a 2×2 identity matrix. Electric field variables are assigned to the faces of a hexahedral element, as shown in figure (2.3), and numbered as in table (2.2). Using equations (3.59) and (3.60), a partition of equation (2.21) into three 2×2 block matrices allows equation (3.58) to be written in block matrix form as

$$\mathbf{K}^{*(i)} = \begin{bmatrix} \left(1+\frac{\sigma_x^e}{j\omega\epsilon_x}\right)^{-1}\mathbf{I}^f & \mathbf{0} & \mathbf{0} \\ \mathbf{0} & \left(1+\frac{\sigma_y^e}{j\omega\epsilon_y}\right)^{-1}\mathbf{I}^f & \mathbf{0} \\ \mathbf{0} & \mathbf{0} & \left(1+\frac{\sigma_z^e}{j\omega\epsilon_z}\right)^{-1}\mathbf{I}^f \end{bmatrix} \begin{bmatrix} \mathbf{K}_x^{(i)} & \mathbf{0} & \mathbf{0} \\ \mathbf{0} & \mathbf{K}_y^{(i)} & \mathbf{0} \\ \mathbf{0} & \mathbf{0} & \mathbf{K}_z^{(i)} \end{bmatrix} \tag{3.61}$$

where $\mathbf{K}_\xi^{(i)}$ denotes the electric elastance matrix associated with the ξ-direction for element 'i'. Using the Boolean matrix defined in equation (2.24), equation (3.61) reduces to

$$\mathbf{K}^* = \sum_{i=1}^{n_e} \mathbf{B}^{f(i)T}\,\mathbf{K}^{*(i)}\,\mathbf{B}^{f(i)} \tag{3.62}$$

Hence the global constitutive equation is represented as

$$\mathbf{F} = \mathbf{K}^*\,\mathbf{D} = \begin{bmatrix} \left(1+\frac{\sigma_x^e}{j\omega\epsilon_x}\right)^{-1}\mathbf{K}_x & \mathbf{0} & \mathbf{0} \\ \mathbf{0} & \left(1+\frac{\sigma_y^e}{j\omega\epsilon_y}\right)^{-1}\mathbf{K}_y & \mathbf{0} \\ \mathbf{0} & \mathbf{0} & \left(1+\frac{\sigma_z^e}{j\omega\epsilon_z}\right)^{-1}\mathbf{K}_z \end{bmatrix} \begin{bmatrix} \mathbf{D}_x \\ \mathbf{D}_y \\ \mathbf{D}_z \end{bmatrix} \tag{3.63}$$

where $\mathbf{K}^*$ is a global complex elastance matrix and $\mathbf{K}_\xi$ denotes the elastance matrix associated with the ξ-direction for the system. Note that the components of the complex elastance matrix and the components of complex inductance matrix are specified for each face and each edge of the lattice.

The computational domain is divided into two regions, one of air and one of anisotropic PML. Hamilton's equations (3.28) and (3.29) apply to both regions. They are

$$\dot{\mathbf{P}} = -\mathbf{A}^T \mathbf{F} + \mathbf{f}^s \tag{3.64}$$

$$\dot{\mathbf{D}} = \mathbf{A}\,\mathbf{H} - \mathbf{J}^s \tag{3.65}$$

where $\mathbf{J}^s$ denotes impressed current sources and $\mathbf{f}^s$ is a global force vector. The constitutive relations are represented differently for the two regions (air and anisotropic PML).

In air region, the constitutive equations are the same as equations (3.30) and (3.31)

$$\begin{aligned} \mathbf{P} &= \mathbf{L}\,\mathbf{H} \\ \mathbf{F} &= \mathbf{K}\,\mathbf{D} \end{aligned} \tag{3.66}$$

In anisotropic PML region, the magnetic permeability tensor (3.45) (derived in reference [80]), is substituted into the constitutive equation (3.57). Due to the block matrix form of the magnetic inductance matrix, the components $\mathbf{P}_x$, $\mathbf{P}_y$, and $\mathbf{P}_z$ of the magnetic momenta can be expressed as.

$$\begin{aligned} \mathbf{P}_x &= \left(1 + \frac{\sigma}{j\omega\epsilon_1}\right)^{-1} \mathbf{L}_x\,\mathbf{H}_x \\ \mathbf{P}_y &= \left(1 + \frac{\sigma}{j\omega\epsilon_1}\right) \mathbf{L}_y\,\mathbf{H}_y \\ \mathbf{P}_z &= \left(1 + \frac{\sigma}{j\omega\epsilon_1}\right) \mathbf{L}_z\mathbf{H}_z \end{aligned} \tag{3.67}$$

where ϵ_1 is the permittivity of the air and σ is the conductivity of the PML. The evolution equations which yield equations (3.67) for the anisotropic PML region are

$$\begin{aligned}
\dot{\mathbf{P}}_x &= -\frac{\sigma}{\epsilon_1}\,\mathbf{P}_x + \mathbf{L}_x\,\dot{\mathbf{H}}_x \\
\dot{\mathbf{P}}_y &= \frac{\sigma}{\epsilon_1}\,\mathbf{L}_y\,\mathbf{H}_y + \mathbf{L}_y\,\dot{\mathbf{H}}_y \\
\dot{\mathbf{P}}_z &= \frac{\sigma}{\epsilon_1}\,\mathbf{L}_z\mathbf{H}_z + \mathbf{L}_z\,\dot{\mathbf{H}}_z
\end{aligned} \tag{3.68}$$

Substituting the electric permittivity tensor (equation (3.44)) into the constitutive equation (3.63) yields

$$\begin{aligned}
\mathbf{F}_x &= \left(1 + \frac{\sigma}{j\omega\epsilon_1}\right)\mathbf{K}_x\mathbf{D}_x \\
\mathbf{F}_y &= \left(1 + \frac{\sigma}{j\omega\epsilon_1}\right)^{-1}\mathbf{K}_y\,\mathbf{D}_y \\
\mathbf{F}_z &= \left(1 + \frac{\sigma}{j\omega\epsilon_1}\right)^{-1}\mathbf{K}_z\,\mathbf{D}_z
\end{aligned} \tag{3.69}$$

The evolution equations which yield equations (3.69) for an anisotropic PML region are

$$\begin{aligned}
\dot{\mathbf{F}}_x &= \frac{\sigma}{\epsilon_1}\,\mathbf{K}_x\,\mathbf{D}_x + \mathbf{K}_x\,\dot{\mathbf{D}}_x \\
\dot{\mathbf{F}}_y &= -\frac{\sigma}{\epsilon_1}\,\mathbf{F}_y + \mathbf{K}_y\,\dot{\mathbf{D}}_y \\
\dot{\mathbf{F}}_z &= -\frac{\sigma}{\epsilon_1}\,\mathbf{F}_z + \mathbf{K}_z\,\dot{\mathbf{D}}_z
\end{aligned} \tag{3.70}$$

3.3 Example Problems for Electromagnetic Systems and Thermo-electromagnetic Systems

In this section, five representative examples are considered to validate the discrete Hamilton's equations derived for thermo-electromagnetic systems with open and closed boundaries. The first test problem considers transverse magnetic (TM) waves with closed boundary conditions (perfect conductor). As a dual problem, the transverse electric (TE) wave problem will be solved using the dual formulation in Appendix A. The anisotropic PML is applied for open boundary conditions, in the case of wave propagation and scattering in biological tissues. Wave propagation problem for a parallel plate waveguide problem, with both closed and open boundary conditions, is used to test three dimensional hexahedral elements. Finally, a Joule heating problem is considered to test the formulation.

3.3.1 Example Problems for Electromagnetic Systems

3.3.1.1 TM Wave

Transverse magnetic (TM) and transverse electric (TE) waves propagating in free space, surrounded by a perfect conducting wall, are typical test examples used to validate new formulations, since they admit exact solutions [45][70]. The two dimensional electromagnetic wave problems, with no variation of the fields in the z direction, are solved for TM_z and TE_z modes. Note that solving in the latter mode requires a dual formulation, in which electric field variables are assigned edge interpolations and magnetic field variables are assigned face interpolations. That formulation is developed in Appendix A.

The first example solves the TM_z wave propagation problem, in which the magnetic fields are transverse to the z-directional plane in the closed region, $\{(x,y)|0 \le x \le x_0, 0 \le y \le y_0\}$. The initial conditions for the electric field intensity are given as

$$E_z(x,y,0) = E_0 sin(\frac{m\,\pi}{x_0}\,x) sin(\frac{n\,\pi}{y_0}\,y) \tag{3.71}$$

with the perfect electric conductor (PEC) boundary condition,

$$E_z = 0 \begin{cases} \text{at } y = 0 \quad \text{and} \quad y = y_0 \\ \text{at } x = 0 \quad \text{and} \quad x = x_0 \end{cases} \tag{3.72}$$

Here E_0 is the magnitude of initial electric field, m and n are mode shapes, and x_0 and y_0 are the x and y lengths of the domain. The initial configuration is shown in figure (3.2) and the geometric and numerical parameters are given in table (3.1). This simulation employs 1,815 square elements, composed of 3,718 edges and 1,815 faces. Magnetic field intensities (H_x and H_y) are interpolated by edge elements and electric flux density (D_z) is interpolated by face elements. Ten grid points per wavelength are used to obtain less than 1% error in the L^2-norm. A second order Runge Kutta method is used to integrate the ordinary differential equations. Figures (3.3) and (3.4) compare the results calculated for the discrete Hamiltonian formulation with the exact solutions at a termination time of 91.7 ns (2.2×period). Figure (3.5) shows the contour plots of the calculated electric and magnetic fields.

3.3.1.2 The Penetration and Scattering of Electromagnetic Fields on Two Dimensional Circular Cylinder Biological Tissues

The second example problem involves the penetration and scattering of electromagnetic plane waves on human biological tissues, at radio frequencies (RF) in an infinite domain as shown in figure (3.6). This problem was solved, for example, to quantify the effects to the human body of exposure to environmental hazards (RF dosimetry). It has been solved with the finite difference time domain and fast fourier transform conjugate gradient methods [11].

This test problem involves two cases. Case one is an electromagnetic wave incident on homogeneous muscle tissue, and case two is an electromagnetic wave incident on an inhomogeneous muscle-fat tissue. The first case considers 100MHz and 300MHz TM polarized waves while the second case considers a 100MHz TM polarized wave. The biological tissues are represented by a two-dimensional circular cylinder, with lossy dielectric materials. The circular cylinder is placed in the center of the free space, and the anisotropic perfectly matched layers [80] [55] surround the computational domain, as shown in figures (3.7) and (3.11). Since exact solutions exist for a simple concentrically layered circular cylinder [18][40], two dimensional cylindrical models of biological tissues are chosen for the verification problem. The TM_z uniform plane wave excitation is normally incident on a lossy dielectric circular cylinder of radius ρ, as shown in figures (3.7) and (3.11). This incident electric field determines the force vector in equation (3.28).

For the homogeneous case, the lossy dielectric material properties approximate biological tissues of human muscle [11][50], and are tabulated in table (3.2). The dielectric circular cylinder model employed 709 square lattices as shown in figure (3.8). Subtraction of the incident field, commonly used in numerical analysis of scattering problems [89][11][88], is used here to prevent the plane wave from interacting with the absorbing boundary conditions as well as to minimize the load of the anisotropic PML as shown in figures (3.8) and (3.12). Spatially graded values are typically used for the numerical conductivity (σ) in the absorbing medium [8]. The grade function normally used for numerical material conductivity is increased from zero at the interface to a maximum at the outer boundary of the anisotropic PML and is given by

$$\sigma(x) = \sigma_{max} \left(\frac{x}{d}\right)^m \tag{3.73}$$

where d is thickness of the anisotropic PML layers and m is normally selected in the range of $3 \leq m \leq 4$ [8][99]. In this dissertation, we choose 3 for m. σ_{max} is the maximum conductivity at the outer boundary and depends on the desired reflection error and the thickness of the absorbing layer [51],

$$\sigma_{max} = -\frac{(m+1)\ln[R_{err}]}{2\eta d} \tag{3.74}$$

where η is the PML's wave impedance and R_{err} is the desired reflection error. The reflection error $R_{err} = e^{-16}$ is selected for this example and a ten-layer PML medium is applied. The values of σ are determined by the spatial grading function and the desired reflection error and are tabulated in table (3.3).

The anisotropic PML is used to absorb x and y direction scattered fields from the biological tissues. For two dimensional problems, the permeability and permittivity tensors of the anisotropic PML material are well referenced [34][52][89]. Implementation of the two dimensional PML model is summarized in appendix B. The anisotropic permittivity and permeability tensors (3.44) and (3.45) are used here to terminate the x-directional waves in the region 1, and a similar formulation is used to terminate the y-directional waves in region 2. However, the corner areas of region 3 need to terminate both x and y-directional waves, so that further modification is required. Figures (3.9) and

(3.10) illustrate the simulation results for homogeneous muscle tissues exposed to incident frequencies of 100MHz and 300MHz, and show the magnitude of the transmitted electric fields inside the homogeneous biological tissues. The discrete Hamiltonian solution is in good agreement with the exact solution.

In case two, the model is composed of an inner layer of muscle and an outer layer of fat, and is exposed to 100MHz TM incident wave. The material properties were obtained from references [11][50] and are listed in table (3.4). The two layered cylinder was discretized by using two dimensional square lattices and embedded in free space. The computational domain is truncated by a 10 layered anisotropic PML, as shown in figure (3.12). Figure (3.13) compares the numerical solution with the exact solution (magnitude of the transmitted electric fields) along the x and y axis. The results of the current method agree very well with the exact solutions.

3.3.1.3 Rectangular Waveguide

The third test problem is the rectangular waveguide problem of Rodridge et al. [79]. It illustrates application of the derived formulation for electromagnetic wave propagation as follows: The geometry of the problem is width ($a = 1m$) in the x direction, height ($b = 0.5m$) in the y direction and infinite in the z direction, as shown in figure (3.14). The excitation wave propagates in the positive z direction, with initial conditions of zero electric and magnetic fields. On the external boundary surface ($z = 0$)

$$\vec{\mathbf{E}}^s = (1 - exp(-(\frac{t}{2T})^2))sin(\pi x/a)sin(\omega t) \;\; \vec{\mathbf{a}}_y \tag{3.75}$$

where $\omega = 5.523599$ rad/s, $T = 0.5$ s, and $\vec{\mathbf{a}}_y$ is unit vector in the y-direction. This electric source determines the force vector derived from the virtual work in the equation (3.28). The wave propagation is bounded by perfect electric conducting guiding structures, described by the boundary conditions

$$E_y = 0, \qquad \text{at } \ x = 0 \ \text{ and } \ x = a \tag{3.76}$$

The waveguide is truncated by introducing an anisotropic PML to absorb outgoing waves propagating in the z direction [80][98][36]. Ten layers of anisotropic PML are included at the right end of the computational domain; they are planes normal to z-axis. Electric and magnetic material parameters are assigned to each face and edge of the PML region. Note that discontinuities at the interface of two distinctive materials generally introduce discretization errors. To reduce this error, the grade function (3.73) is again used for both the electric and magnetic material conductivities. The numerical parameters of the ten layer anisotropic PML depend on the desired reflection error ($R_{err} = e^{-16}$), and are listed in table (3.5).

The exact steady state solution for this problem is [5][21][79]

$$
\begin{aligned}
\mathbf{E}_x &= 0, \\
\mathbf{E}_y &= sin(\frac{\pi x}{a})sin(\omega t - \beta_z z), \\
\mathbf{E}_z &= 0, \\
\mathbf{B}_x &= \frac{\beta_z}{\omega} sin(\frac{\pi x}{a})sin(\omega t - \beta_z z), \\
\mathbf{B}_y &= 0, \\
\mathbf{B}_z &= \frac{(\pi/a)^2}{\omega} cos(\frac{\pi x}{a})cos(\omega t - \beta_z z)
\end{aligned}
\tag{3.77}
$$

where $\beta_z = \sqrt{\omega^2 \mu \epsilon - (\pi/a)^2}$ is the wave number. For this simulation, the computational domain was discretized using 5,000 brick elements, which have 18,215 edges and 16,550 faces, to interpolate as shown in figure (3.15). Figures (3.16) and (3.17) compare the exact and numerical solutions for the steady state electric and magnetic fields, at a stop time of 20 seconds, long enough time for the fields to propagate twice the truncated length of the waveguide. Contour plots of the calculated electric and magnetic fields are given in figure (3.18). They show very good agreement with the exact solutions.

3.3.2 Example Problem for Thermo-electromagnetic System: Resistive Heating in an Electromagnetic Launcher

The ability of the numerical method developed in chapter 2 to model thermo-electromagnetic systems is examined in this section. Electromagnetic launchers are considered to be plausible candidates to launch materials into low earth orbit or penetrate advanced military armors. A large electrical current, up to several million amperes, is required to pass through the rails. Numerical calculation of the resultant current and heat diffusion in the rails plays an important role in the determination of the cross sectional dimensions of the electromagnetic launcher, as shown in figure (3.19). A one dimensional nonlinear analysis, which calculates current and heat diffusion in the rail conductors [28][54], is used to test the derived formulation for thermo-electromagnetic problems. The modeled geometry has a finite thickness and an infinite width, as shown in figure (3.20). The material properties are taken from reference [63] and listed in table (3.6). Note that the magnetic permeability and mass density are assumed to be constant, and that other material properties are taken to change linearly with temperature. A time varying magnetic field is imposed on the lower segment of the plate and vanishes on the upper boundary of the plate, as shown in the figure (3.20),

$$\begin{aligned} H(t) &= H_0\, sin(\pi\, t/p) && at\ \ y = 0 \\ H(t) &= 0 && at\ \ y = b \end{aligned} \tag{3.78}$$

where H_0 is the magnitude of the magnetic field and p is the pulse duration of the magnetic field input. Given a magnetic field source, the coupled heat and current diffusion problem can be formulated using the discrete Hamilton's equations (2.62), (2.63), and (2.64), along with the constitutive relations, initial conditions and boundary conditions. The state space model is

$$\dot{\mathbf{H}}^r = -\mathbf{L}^{-1}\, \mathbf{A}^T\, \mathbf{K}\, \boldsymbol{\mathfrak{C}}^{e-1} \mathbf{A}\, \mathbf{H}^r + \mathbf{b} H(t) \tag{3.79}$$

$$\dot{\mathbf{U}} = \dot{\mathbf{U}}^{irr} - \dot{\mathbf{U}}^{con} \tag{3.80}$$

where $\mathbf{H}^r$ is reduced order magnetic field intensity and $\mathbf{b}$ is a constant column vector. Note that we apply equation (2.63), the discrete Ampere's circuit law, with the assumption of zero displacement current density. The electric conductivity (σ) depends on the temperature

$$\sigma^{(i)} = \frac{1}{\rho^{(i)}} = \frac{1}{\rho_0 + \rho^{'}\,\theta^{(i)}} \tag{3.81}$$

where ρ_0 is electric resistivity at ambient temperature, and $\rho^{'}$ is rate of change of electric resistivity with temperature. Note that the electric conductance matrix depends on temperature and varies with time. The thermal constitutive equations are

$$\begin{aligned} U^{(i)} &= c_v^{(i)} \gamma^{(i)} v^{(i)}\,\theta^{(i)} \\ k^{(i,j)} &= \frac{1}{2\,\ell^{(i,j)}} \left[\left(k_0 + k^{'}\theta^{(i)} \right) A^{(i)} + \left(k_0 + k^{'}\theta^{(j)} \right) A^{(j)} \right] \\ c_v^{(i)} &= c_{v0} + c_v^{'}\,\theta^{(i)} \end{aligned} \tag{3.82}$$

where $c_v^{(i)}$, $\gamma^{(i)}$, and $v^{(i)}$ are the specific heat, mass density, and volume for element 'i', respectively, $k^{(i,j)}$ is a heat conduction coefficient associated with elements 'i' and 'j', $\ell^{(i,j)}$ is length between the centers of element 'i' and element 'j' and $A^{(i)}$ is cross sectional area for element 'i'. Using equation (3.82), equation (2.47) becomes

$$\dot{U}^{con(i)} = \sum_{j=1}^{n_n^{(i)}} k^{(i,j)} \left(\frac{U^{(i)}}{c_v^{(i)}\,\gamma^{(i)}\,v^{(i)}} - \frac{U^{(j)}}{c_v^{(j)}\,\gamma^{(j)}\,v^{(j)}} \right) = \mathbf{k}^{con(i)T}\mathbf{U} \tag{3.83}$$

where $n_n^{(i)}$ is the number of neighboring elements for element 'i', $\mathbf{U}$ is global column vector of internal energies, and $\mathbf{k}^{con(i)}$ is column vector which depends on internal energy and varies with time.

$$\mathbf{k}^{con(i)} = \mathbf{k}^{con(i)}(U, t) \tag{3.84}$$

An insulated thermal boundary condition is imposed, since thermal power flow through external boundaries was not modeled in deriving the energy evolution equation (2.40). Magnetic fields are initially zero and the initial temperature is ambient temperature,

$$\begin{aligned} \mathbf{H} &= 0 \\ \theta^{(i)} &= \theta_0 \end{aligned} \tag{3.85}$$

The numerical solution, calculated from the formulations derived here, is compared with the numerical solutions given in reference [28]. Figures (3.21) and (3.22) show very good agreement.

3.4 Conclusion

The present chapter has outlined a new numerical method for the simulation of electromagnetic systems. Unlike classical finite difference time domain and finite element techniques, the present work formulates the state space dynamic model without reference to any partial differential equations. Instead, edge and face based finite element interpolations are used to define magnetic and potential energy functions, virtual work, and nonholonomic constraints for the system. They are combined to formulate an ordinary differential equation model. It should be emphasized that the contribution of this research lies in its extension of the previous work on mechanical systems [30][33][81] to a new energy domain. Representative electromagnetic examples, with closed and open boundary conditions, have been solved. The numerical results show good agreement with exact solutions and previous numerical results.

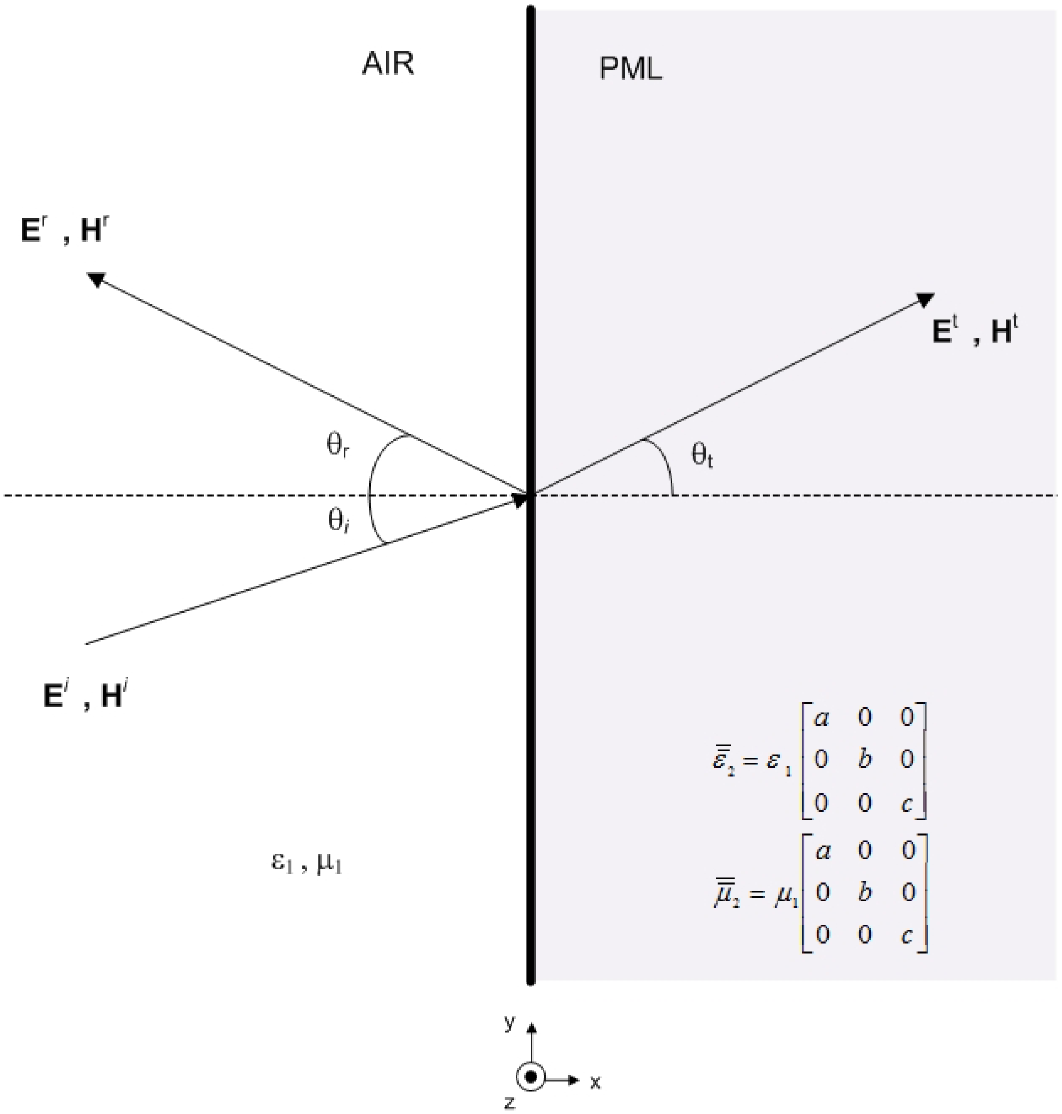

Figure 3.1: Plane wave incidence on the interface between air and PML medium [15]

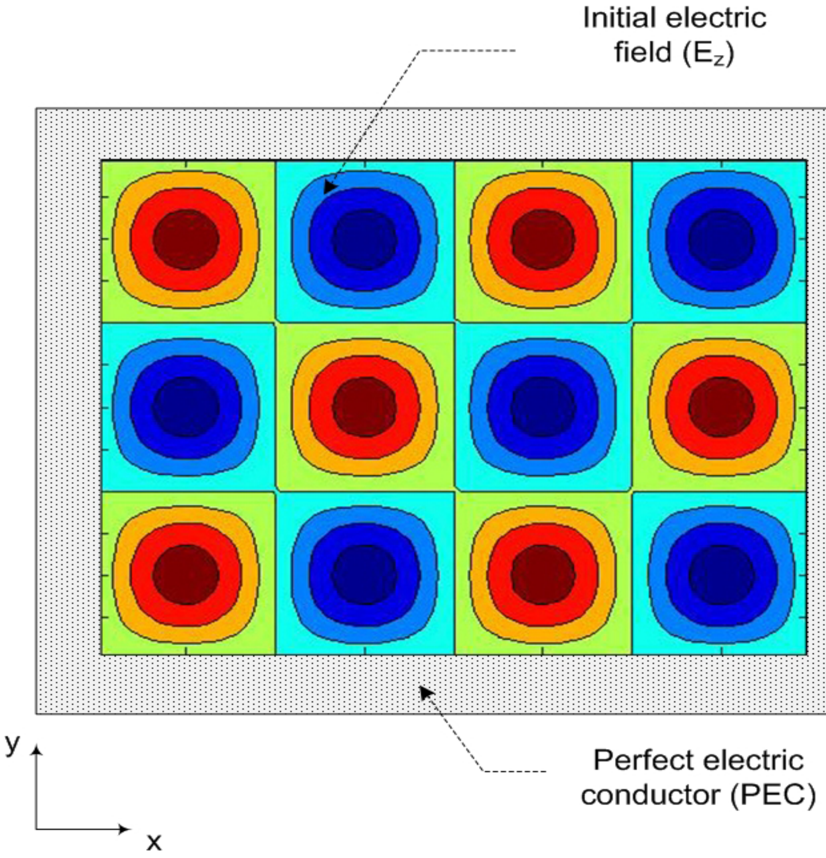

Figure 3.2: Initial configuration for TM wave problem

Parameters	Value
Magnitude of initial electric field	$E_0 = 1$ (V/m)
Mode in x-axis	m = 4
Mode in y-axis	n = 3
Length in x-axis	$x_0 = 40$ (m)
Length in y-axis	$y_0 = 24$ (m)
Permittivity of free space	$\epsilon_0 = 8.8541878 \times 10^{-12}$ (F/m)
Permeability of free space	$\mu_0 = 4\pi \times 10^{-7}$ (H/m)
Relative permittivity of air	$\epsilon_r = 1$
Relative permeability of air	$\mu_r =$1

Table 3.1: Simulation parameters for TM wave problem

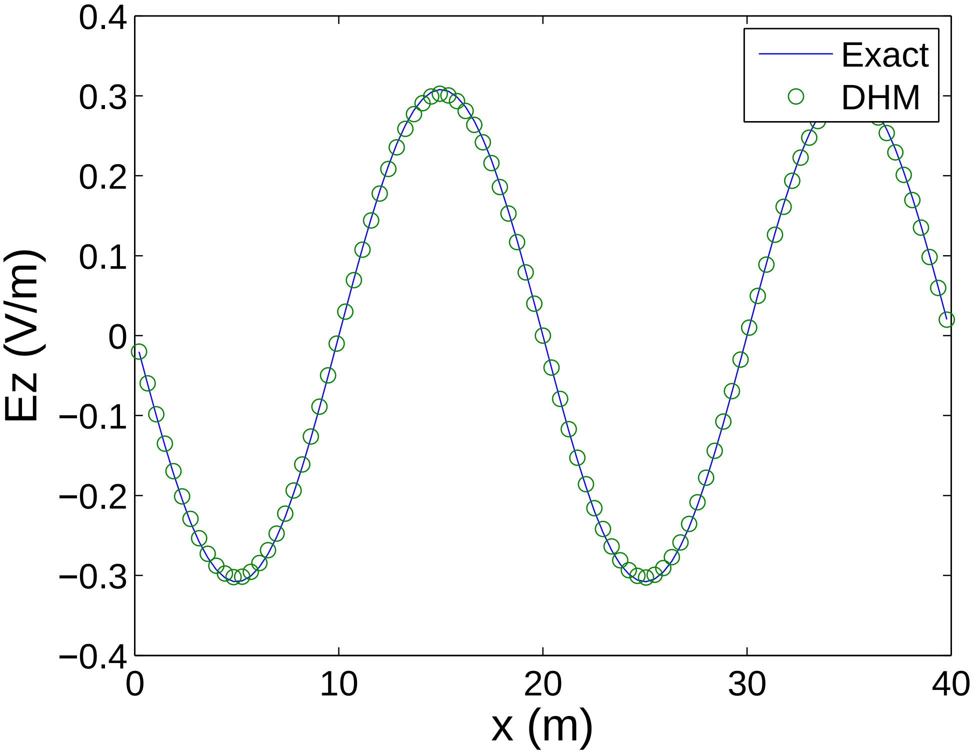

Figure 3.3: Comparison of numerical result calculated by discrete Hamilton's Method (DHM) with exact solution for electric field, Ez at t= 91.7 ns (2.2 × period) and y = 12 m

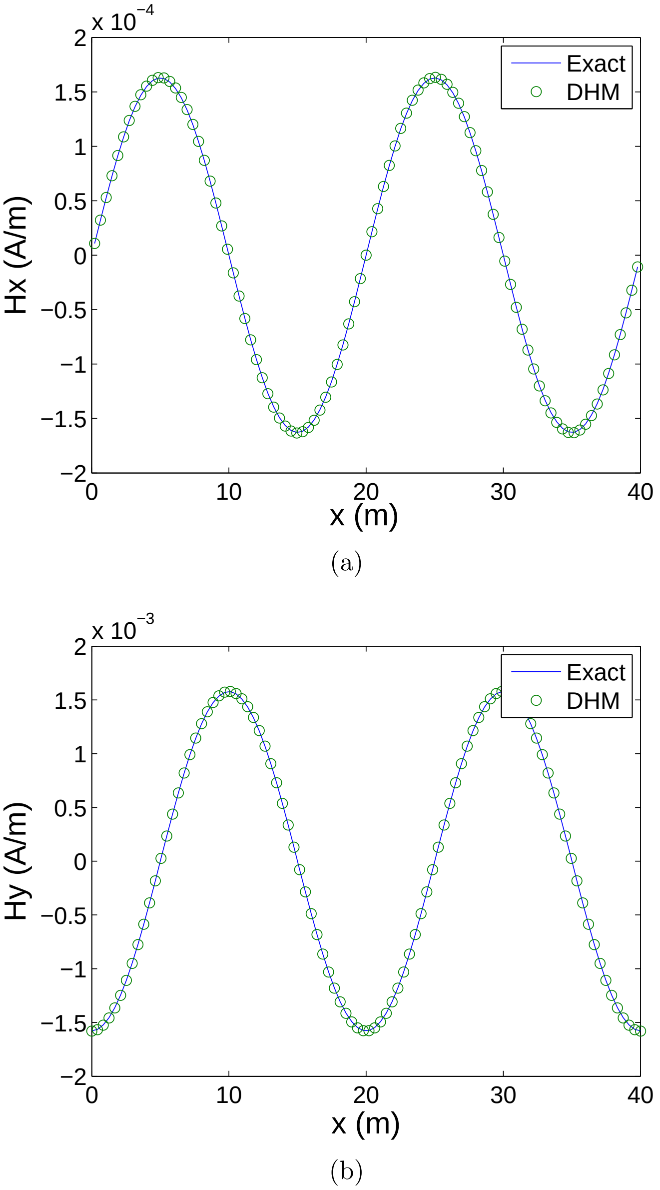

Figure 3.4: Comparison of numerical results calculated by discrete Hamilton's method (DHM) with exact solutions for magnetic field intensities, (a) Hx and (b) Hy at t=91.7 ns (2.2 × period) and y = 12 m

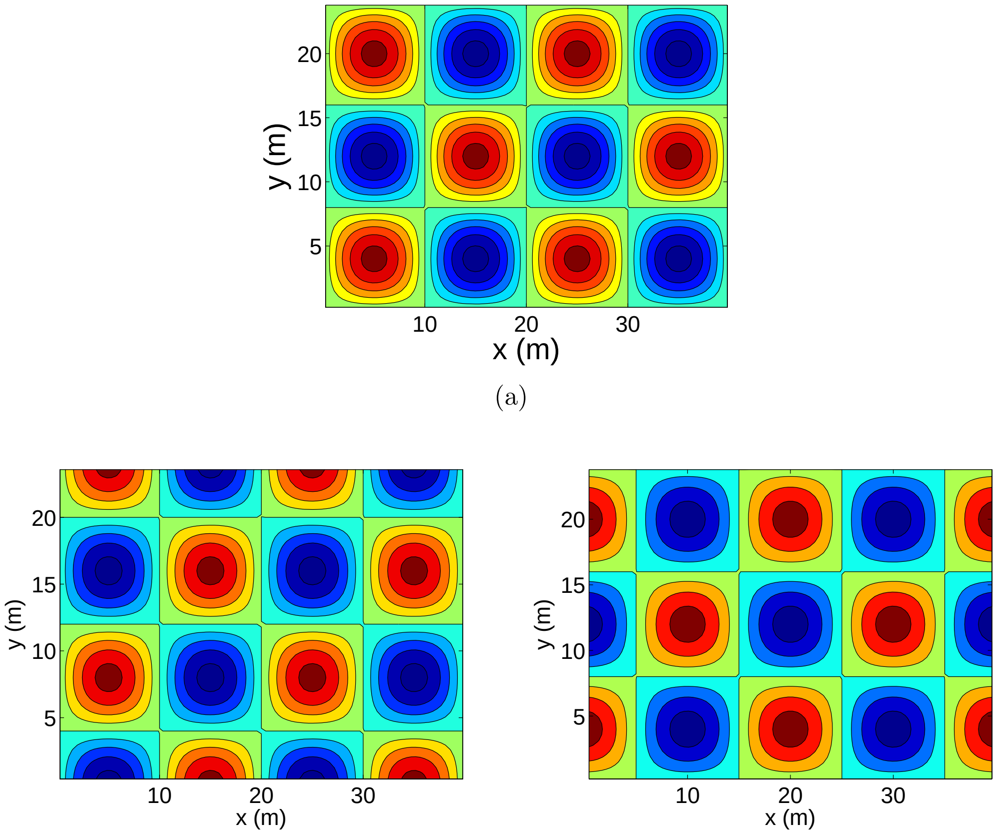

(a)

(b)

(c)

Figure 3.5: Contour plots of the numerical results for (a) E_z, (b) H_x, and (c) H_y at t=91.7 ns (2.2 × period)

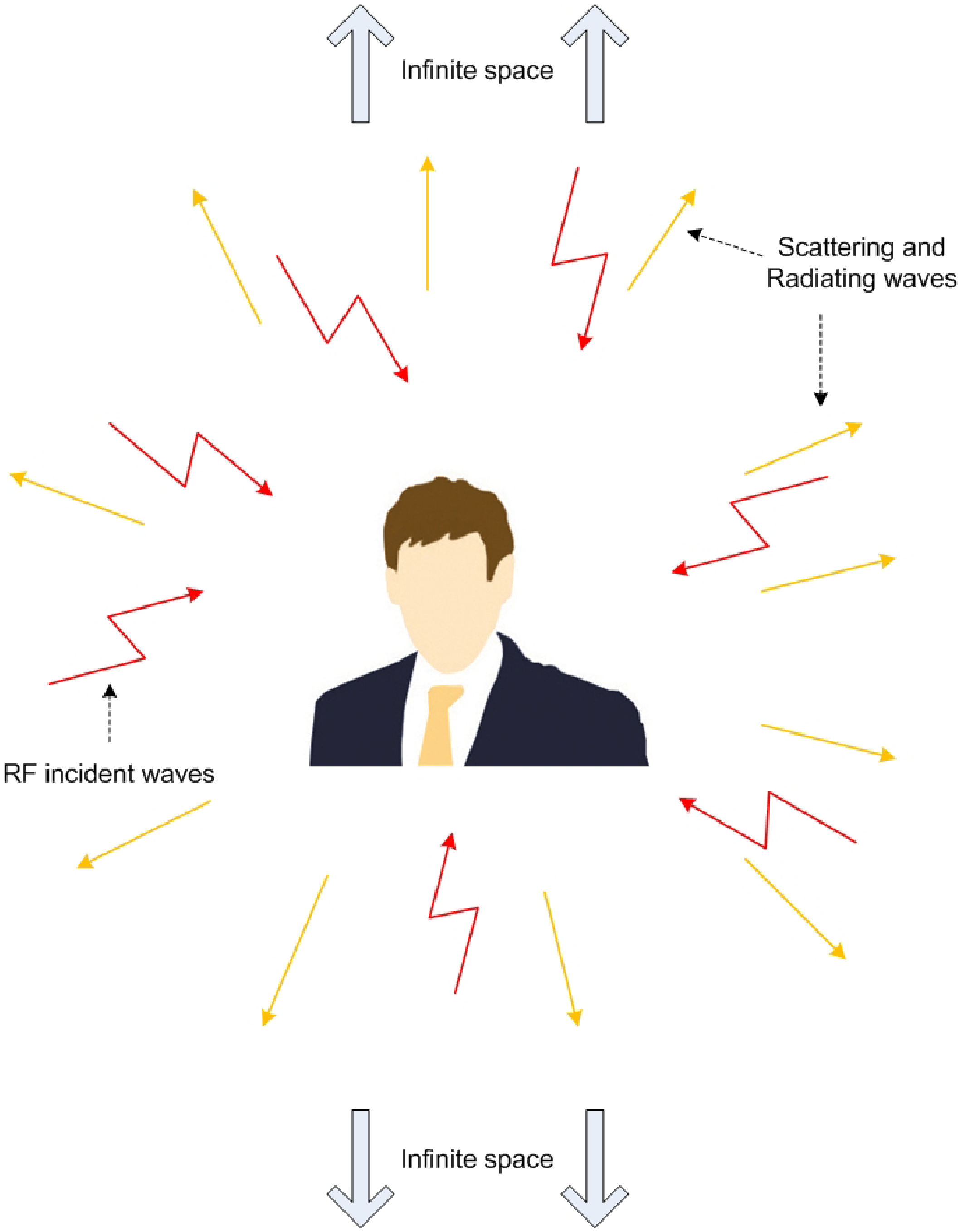

Figure 3.6: Human exposed to radio frequency (RF) electromagnetic field

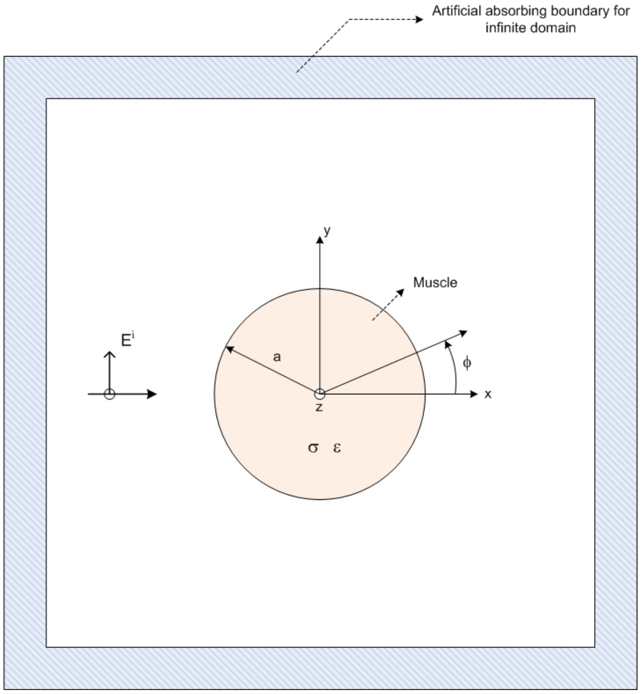

Figure 3.7: Homogeneous circular cylinder muscle tissue model for human exposed to TM polarized plane wave

	Biological tissue	
Parameters	Muscle (100MHz)	Muscle (300MHz)
Dielectric constant	$\epsilon_r = 72$	$\epsilon_r = 54$
Conductivity (S/m)	$\sigma = 0.9$	$\sigma = 1.4$

Table 3.2: Dielectric material properties of homogeneous human muscle tissue [50]

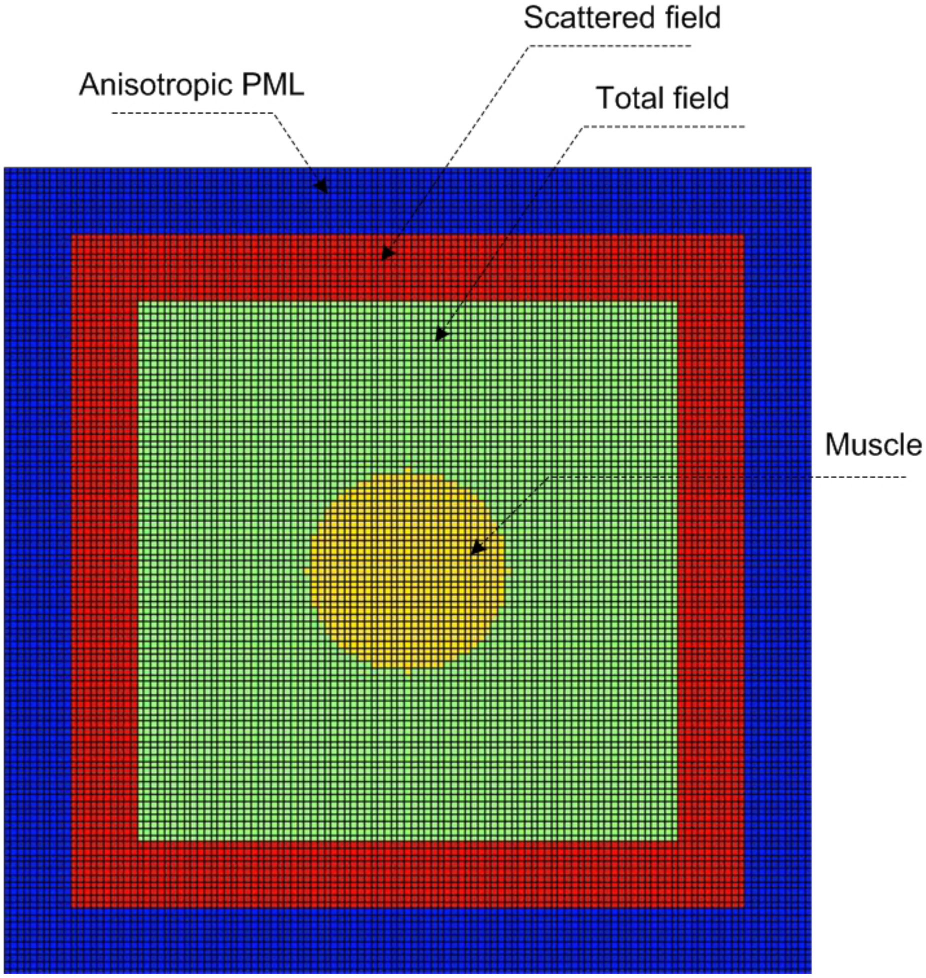

Figure 3.8: Discretization of homogeneous circular cylinder scattering problem

Layers in the plane normal to x-axis					Layers in the plane normal to y-axis				
Magnetic conductivity			Electric conductivity		Magnetic conductivity			Electric conductivity	
edge number	σ_{xx}	σ_{zz}	face number	σ_{yy}	edge number	σ_{xx}	σ_{zz}	face number	σ_{yy}
1	0	0.0016	1	0.0016	1	0	0.0016	1	0.0016
2	0.012	0.0496	2	0.0496	2	0.012	0.0496	2	0.0496
3	0.144	0.338	3	0.338	3	0.144	0.338	3	0.338
4	0.684	1.250	4	1.250	4	0.684	1.250	4	1.250
5	1.112	3.362	5	3.362	5	1.112	3.362	5	3.362
6	5.100	7.442	6	7.442	6	5.100	7.442	6	7.442
7	10.512	14.450	7	14.450	7	10.512	14.450	7	14.450
8	19.404	25.538	8	25.538	8	19.404	25.538	8	25.538
9	33.024	42.050	9	42.050	9	33.024	42.050	9	42.050
10	52.812	65.522	10	65.522	10	52.812	65.522	10	65.522
11	80.400				11	80.400			

Table 3.3: Numerical parameters of electric and magnetic conductivity on each edge and face for ten-layers of anisotropic PML

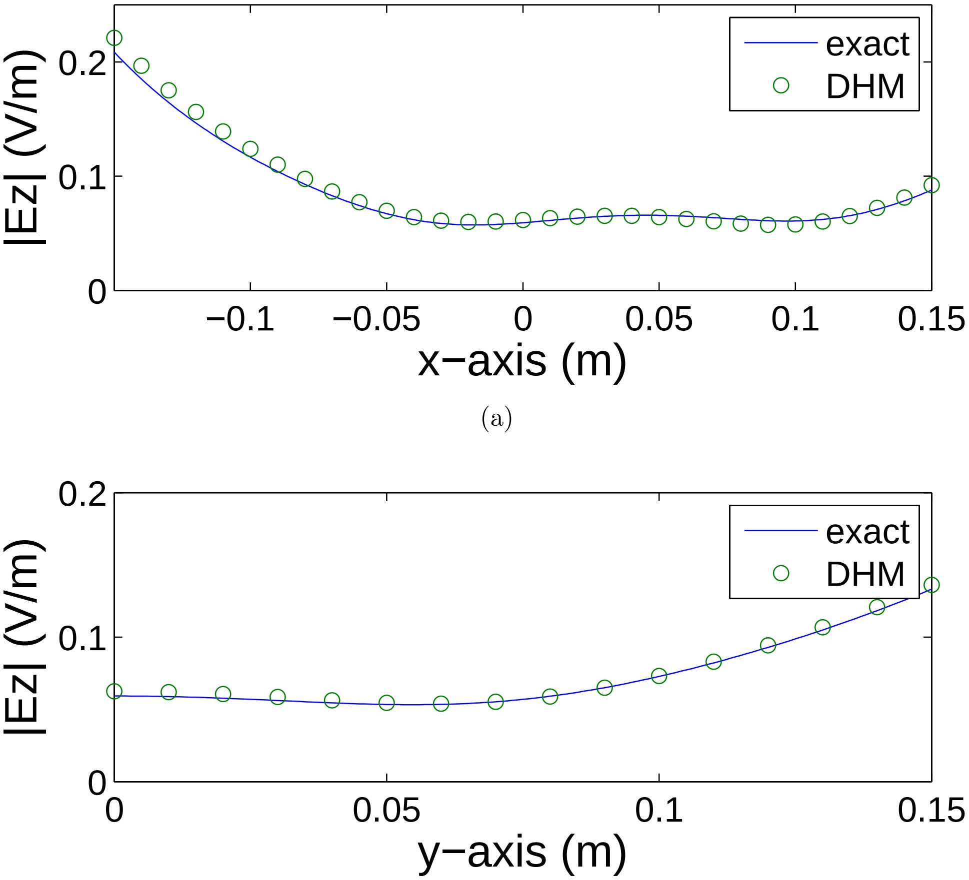

(a)

(b)

Figure 3.9: Comparison of numerical results computed by discrete Hamilton's method (DHM) with exact solutions along (a) x-axis and (b) y-axis for homogeneous muscle cylinder exposed to incident field of 100 MHz frequency

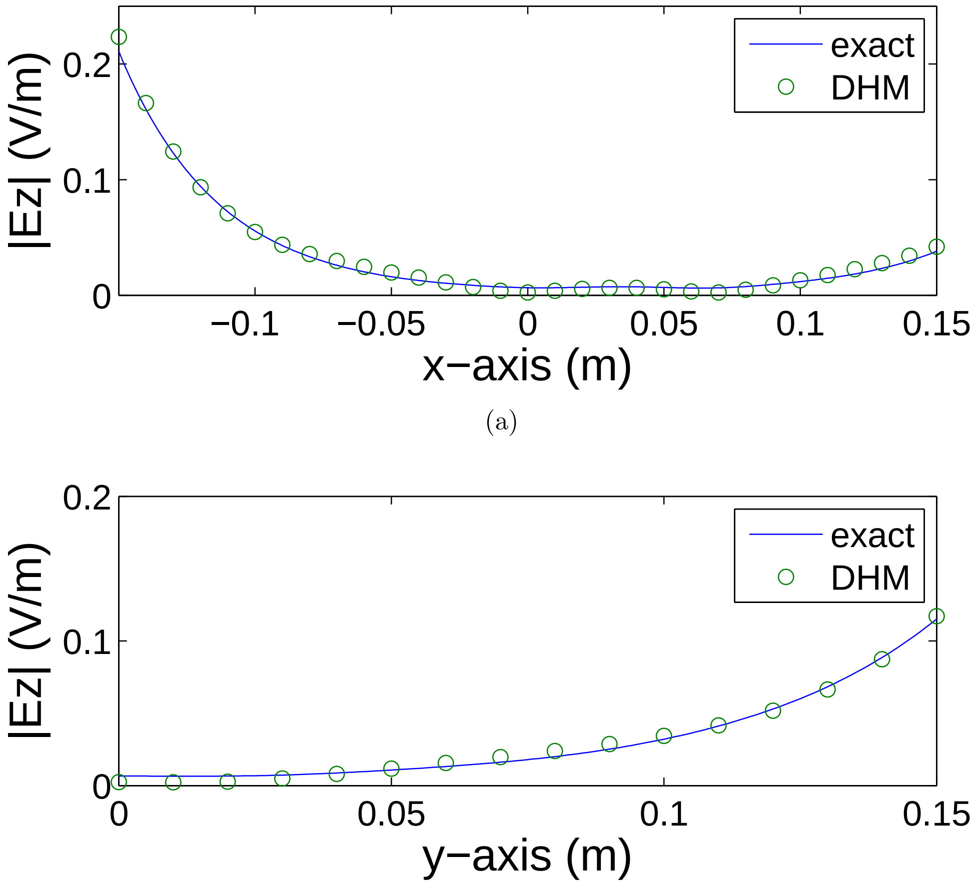

(a)

(b)

Figure 3.10: Comparison of numerical results computed by discrete Hamilton's method (DHM) with exact solutions along (a) x-axis and (b) y-axis for homogeneous muscle cylinder exposed to incident field of 300 MHz frequency

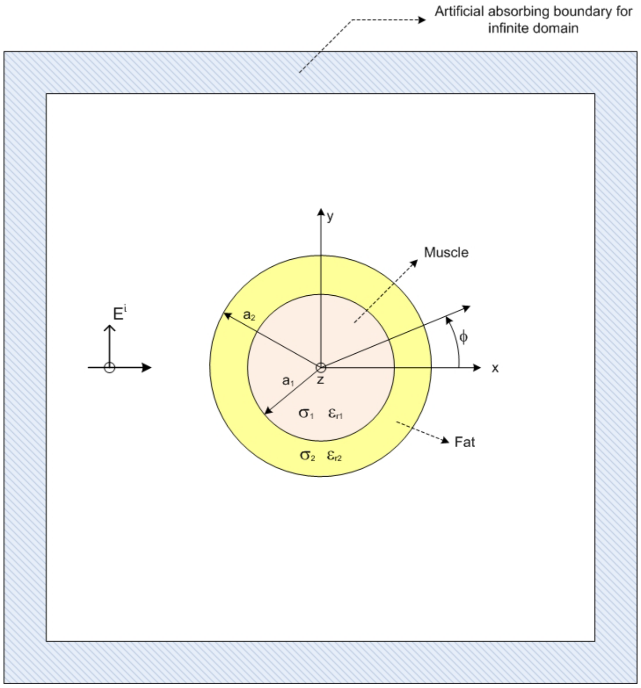

Figure 3.11: Inhomogeneous two-layered circular cylinder muscle-fat tissue model for human exposed to TM polarized plane wave

	Biological tissue	
Parameters	Muscle (100MHz)	Fat (100MHz)
Dielectric constant	$\epsilon_r = 72$	$\epsilon_r = 7.5$
Conductivity (S/m)	$\sigma = 0.9$	$\sigma = 0.048$

Table 3.4: Dielectric material properties of inhomogeneous human muscle-fat tissues [50]

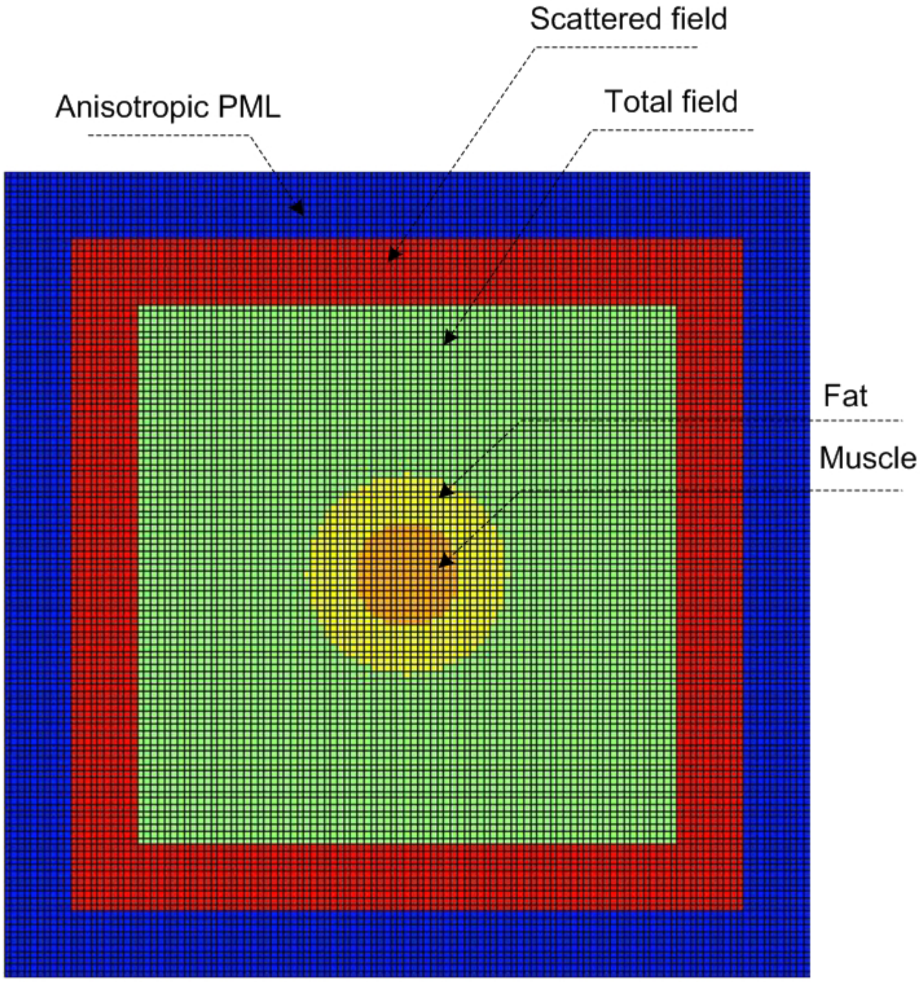

Figure 3.12: Discretization of inhomogeneous circular cylinder scattering problem

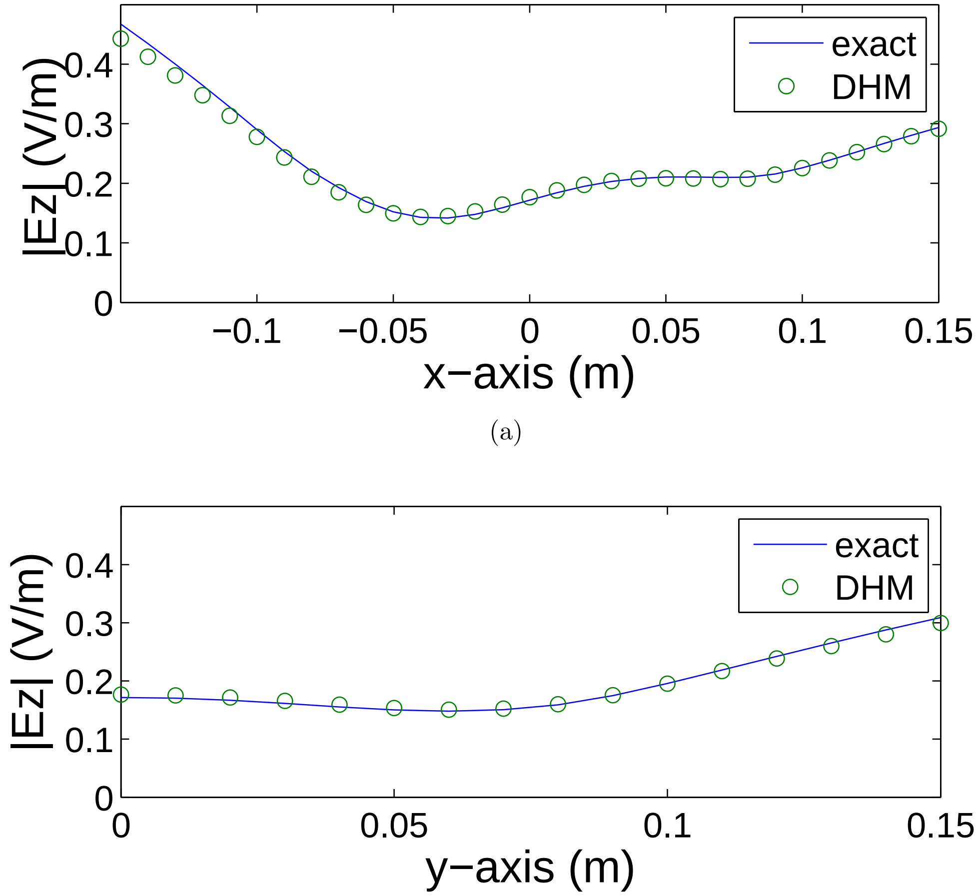

(a)

(b)

Figure 3.13: Comparison of numerical results computed by discrete Hamilton's method (DHM) with exact solutions along (a) x-axis and (b) y-axis for inhomogeneous two layered muscle-fat cylinder exposed to incident field of 100 MHz frequency

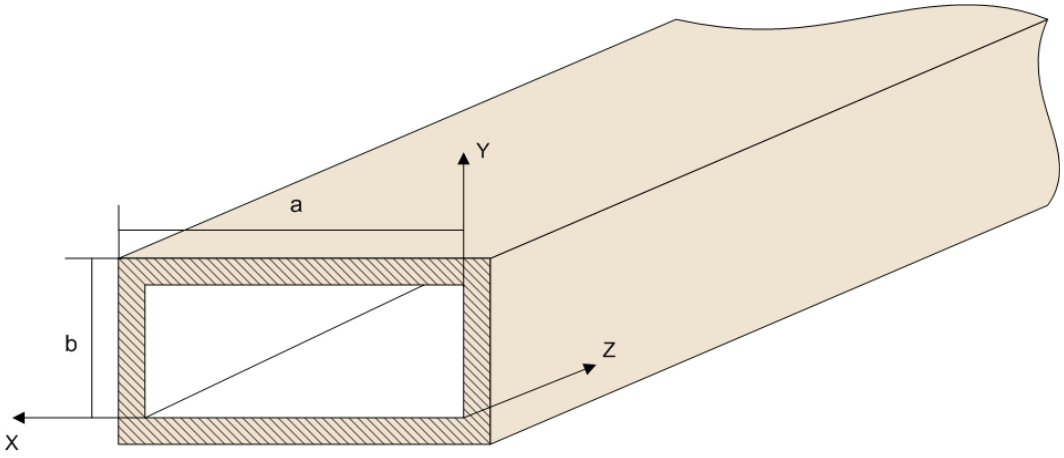

Figure 3.14: Rectangular waveguide [21]

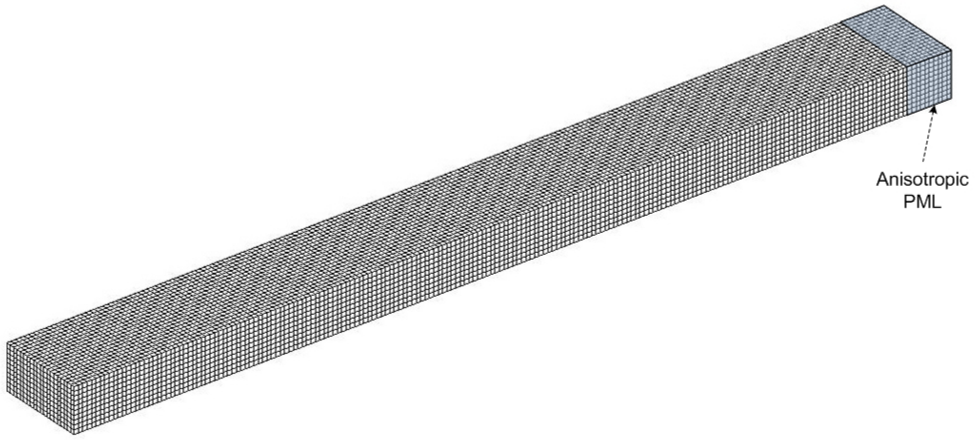

Figure 3.15: Rectangular waveguide hexahedral grid

Magnetic conductivity			Electric conductivity	
edge number	σ_{xx}	σ_{zz}	face number	σ_{yy}
1	0	0.0016	1	0.0016
2	0.012	0.0496	2	0.0496
3	0.144	0.338	3	0.338
4	0.684	1.250	4	1.250
5	1.112	3.362	5	3.362
6	5.100	7.442	6	7.442
7	10.512	14.450	7	14.450
8	19.404	25.538	8	25.538
9	33.024	42.050	9	42.050
10	52.812	65.522	10	65.522
11	80.400			

Table 3.5: Numerical parameters of electric and magnetic conductivity on each edge and face for ten layers of anisotropic PML

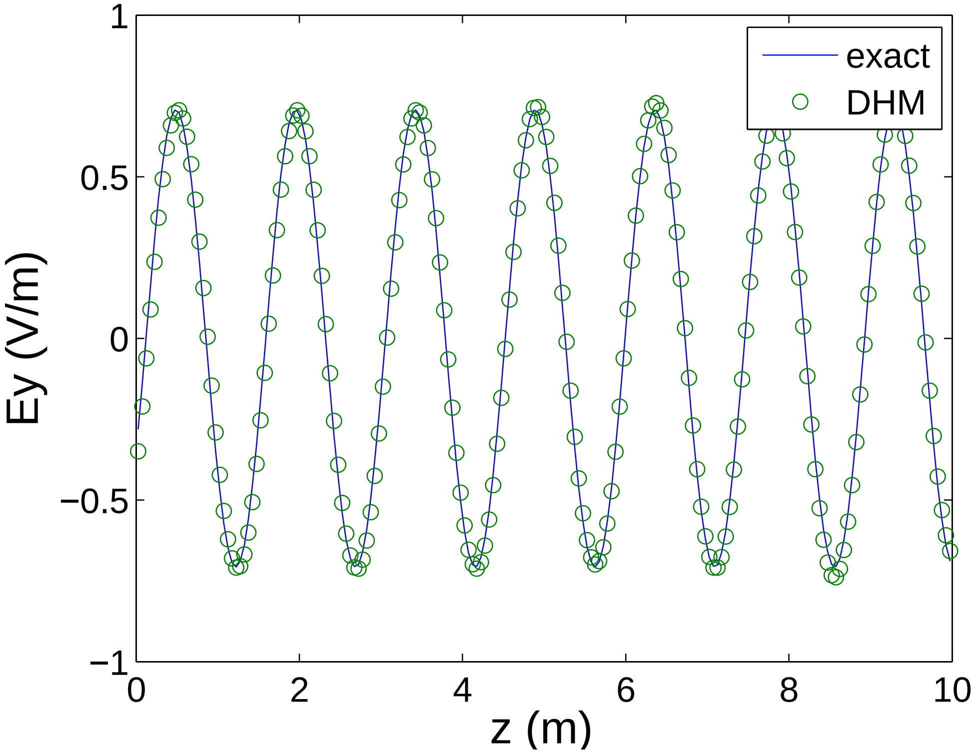

Figure 3.16: Comparison of numerical results (E_y) computed by discrete Hamilton's method (DHM) with the exact solutions at x = 0.225 and t=20 s

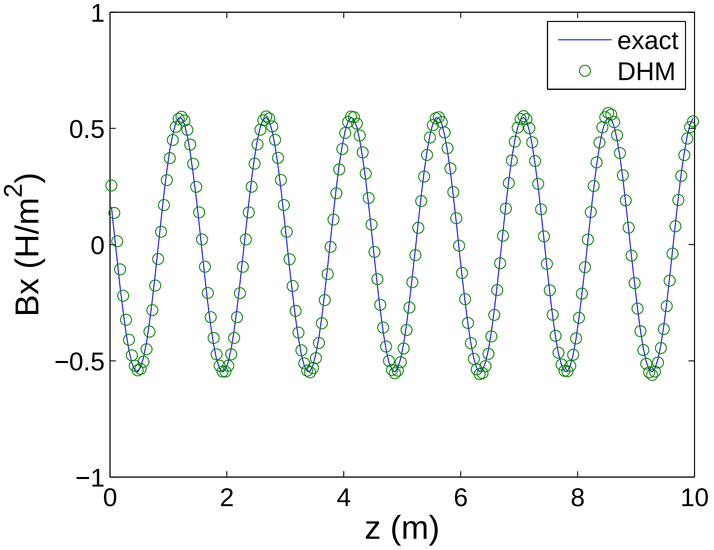

(a)

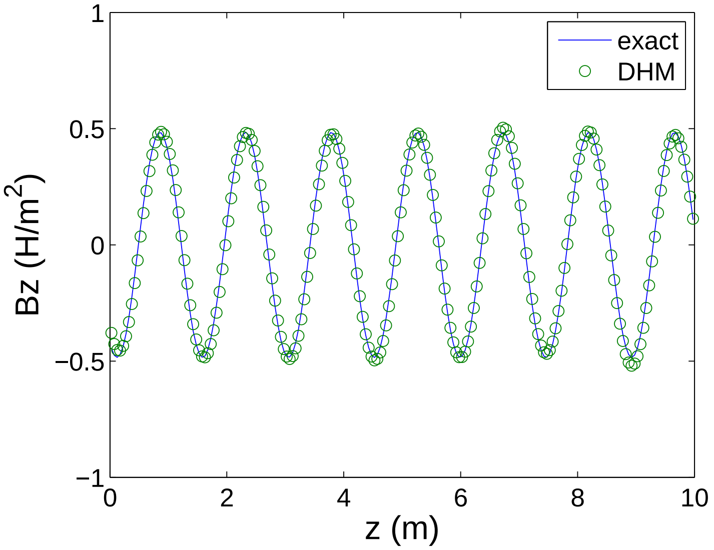

(b)

Figure 3.17: Comparison of numerical results (a) B_x and (b) B_z computed by discrete Hamilton's method (DHM) with the exact solutions at x = 0.225 and t=20 s

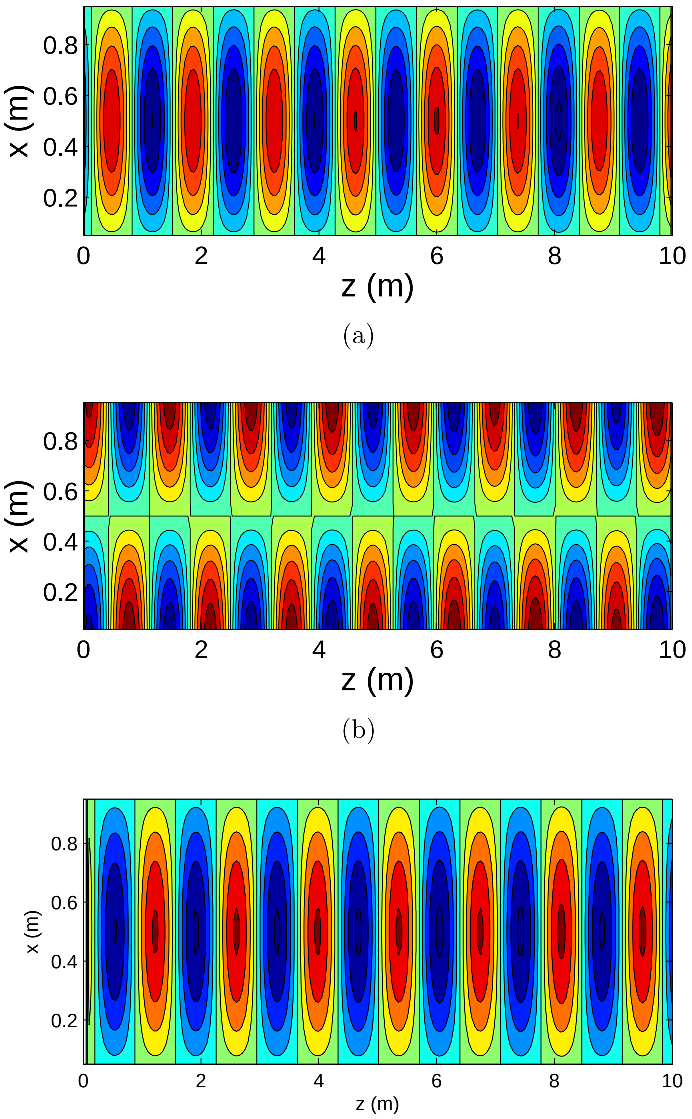

(a)

(b)

(c)

Figure 3.18: Contour plots of the numerical solutions for (a) E_y and (b) B_x and (c) B_z at 20 s

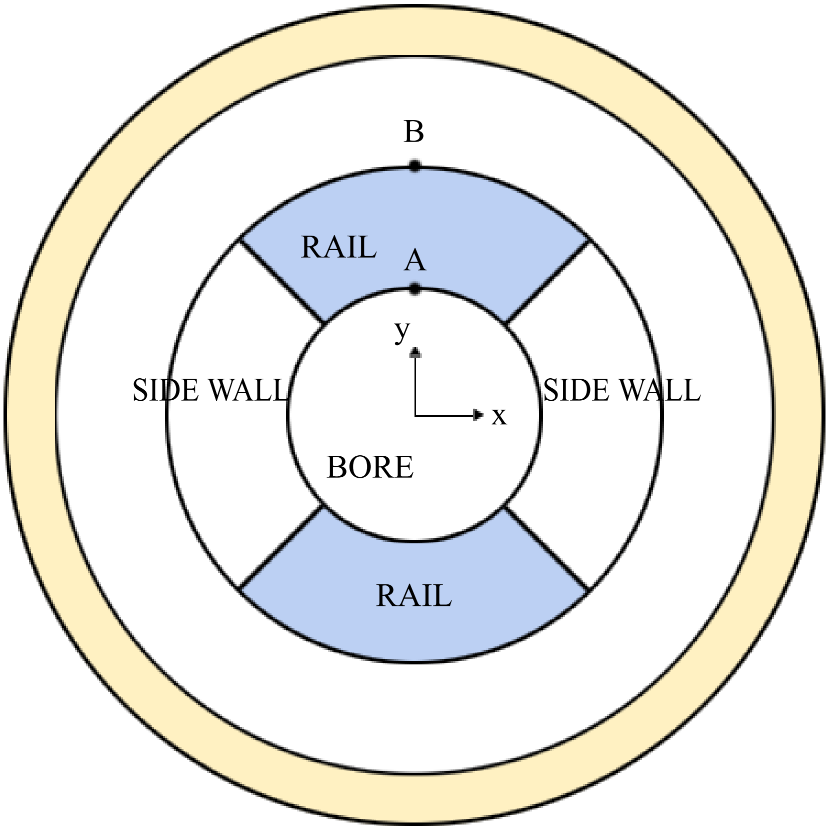

Figure 3.19: EM launcher [27]

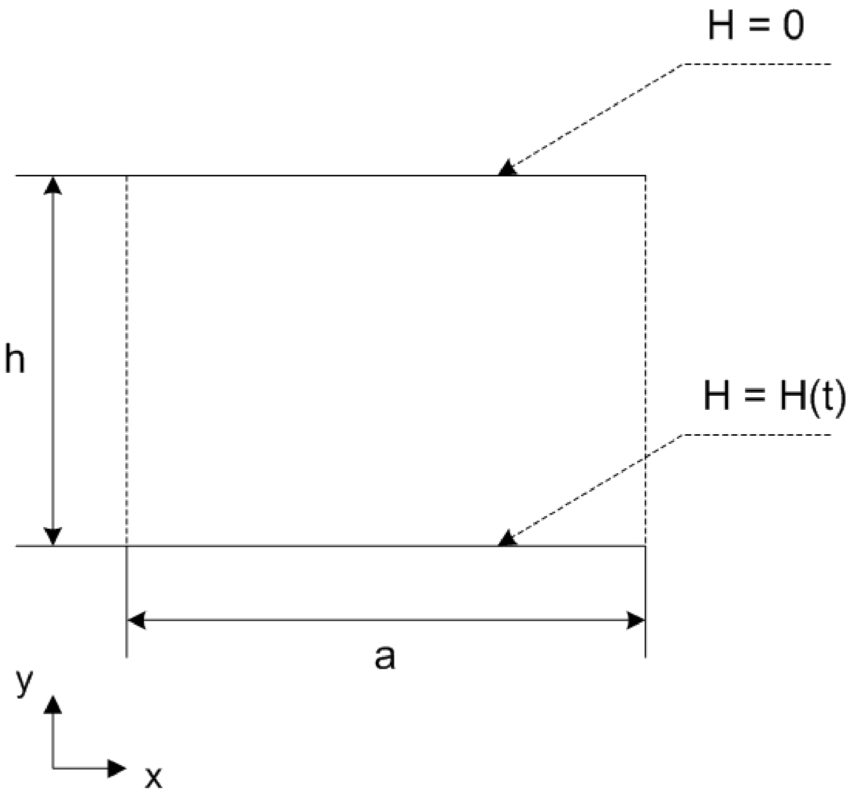

Figure 3.20: Geometry of one dimensional coupled thermo-electromagnetic problem [27]

Parameters	Value
Magnitude of initial magnetic field	$H_0 = 3.20 \times 10^6/\text{a}$ (A/m)
Pulse duration of the current pulse input	p = 0.0066 (s)
Ambient temperature	$T_0 = 20$ (°C)
Height	h = 0.02 (m)
Resistivity	$\rho_0 = 1.57 \times 10^{-8}$ (ohm-m)
Rate of change of the resistivity with temperature	$\rho^{'} = 0.00809 \times 10^8$ (ohm-m/°C)
Thermal conductivity at ambient temperature	$k_0 = 401.0$ (W/m-°C)
Rate of change of the thermal conductivity with temperature	$k^{'} = -0.0655$ (W/m-°C/°C)
Specific heat per unit mass at ambient temperature	$c_{v0} = 3.48 \times 10^2$ (J/°C-kg)
Rate of change of the specific heat per unit mass with temperature	$c_v^{'} = 9.70 \times 10^{-2}$ (J/°C-kg/°C)
Mass density	$\gamma = 8906$ (kg/m^3)
Magnetic permeability	$\mu = 4\pi \times 10^{-7}$ (H/m)

Table 3.6: Simulation parameters for one dimensional thermo-electromagnetic problem (copper) [27][63]

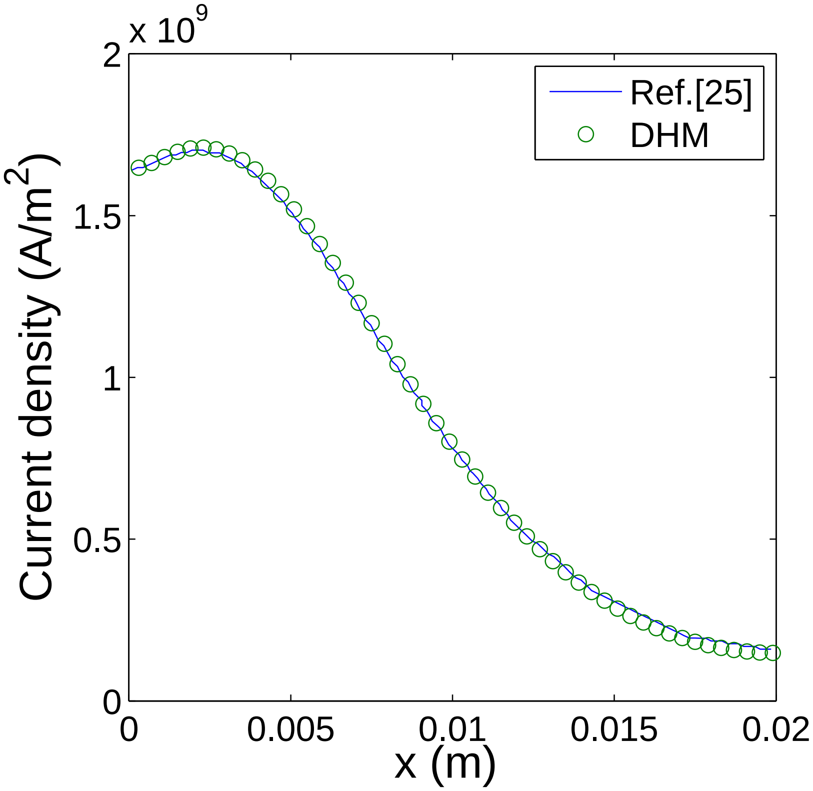

Figure 3.21: Current density distribution at t=p/2, for a copper conductor (h=0.02 m)

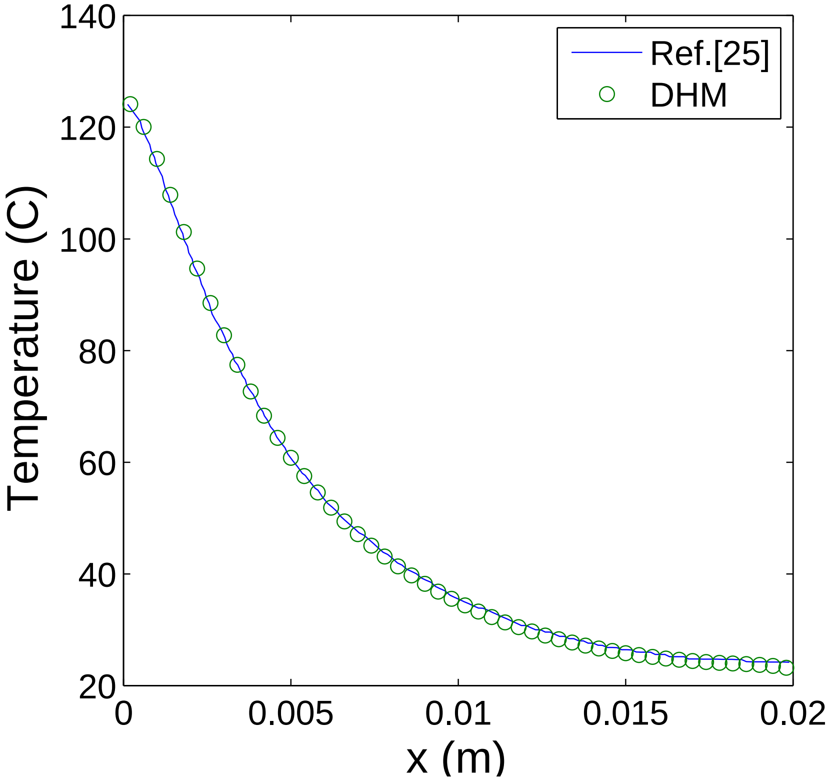

Figure 3.22: Temperature distribution at t=p, for a copper conductor (h=0.02 m)

Chapter 4

Frequency Domain Analysis and Magnetostatic Systems

4.1 Introduction

When man-made electric devices are excited by time harmonic, or sinusoidal sources at a constant frequency and the main interest of the problem for linear media is to find the steady state responses of the fields, formulation of electromagnetic problems in the frequency domain is computationally efficient and effective. The ability of new numerical methods to solve electromagnetic problems, such as antennas, microwaves, and radios, formulated in frequency domain is very important for computational electromagnetics. Frequency domain numerical techniques for electromagnetic systems has been an intense research subject and integral equation methods [78][39] and finite element methods [83][49] have become most powerful tools to calculate the fields. The former method, known as the method of moments, was very popular in the seventies and eighties and was extensively used for the numerical simulation of electromagnetic scattering and radiation problems. However, this method results in fully populated matrices which demand a large storage requirement, even for relatively small problems. Finite element methods which generate very sparse matrix systems, can be divided into classical nodal finite element

[4][84] and "edge-based" finite element methods [59][3][23] depending on the types of basis functions. Node based finite element methods have been extensively used for scalar electromagnetic field problems. However, nonphysical solutions (spurious mode) have been problematic. Edge based finite element methods have been developed to overcome this problem and have been successfully implemented for solving vector electromagnetic field problems.

Even though absorbing boundary condition (ABC) [42][6], perfectly matched layer (PML) [15][98] and finite element boundary integral methods [82][66] have been applied to infinite domain problems, the incorporation of open boundary conditions has played an important role in achieving accuracy and efficiency. The anisotropic PML, an alternative formulation of perfectly matched layer (PML), proposed by Sacks *et al.*[80] has became a promising truncation scheme. It avoids the nonphysical modification of Maxwell's equations introduced in the original PML method. This absorbing layer has anisotropic material properties (ϵ, μ, σ^e, σ^m), which can be realized as anisotropic layers with properly chosen complex permittivity and permeability tensors.

Many electromechanical machines such as transformers, motors, and magnetic bearings, are actuated by steady or dc currents. The accurate calculation of static magnetic fields is important in the design of electromagnetic devices. It may be difficult to analytically calculate these magnetic fields. The most common numerical approach to magnetostatic fields is finite element methods, using the vector or scalar potentials [17][24], which has been successfully applied in many practical applications. Since it often suffered from the enforcement of interelement continuity, edge elements [2][12] and mixed formulations of edge and face elements [16] have been introduced and used for magnetostatic problems.

This chapter is organized as follows. The transient Hamiltonian formulation is converted into a time harmonic form. To validate the derived equations in the frequency domain, benchmark problems are numerically solved and compared with exact solutions. Next, the formulation is reduced to static equations, with the assumption that the time-varying electric and magnetic field terms are neglected. The resulting static equations are decoupled into magnetostatic and electrostatic equations. Some representative examples are chosen and solved to validate the derived magnetostatic formulation.

4.2 Discrete Hamilton's Equations for Electromagnetic Systems in Frequency Domain

In the preceding two chapters, a new discrete formulation of the electromagnetic and thermo-electromagnetic problems has been derived. In this section, assuming an e^{jwt} time dependence, the proposed time domain equations for electromagnetic systems will be transformed into algebraic equations for the time varying electromagnetic quantities. The generalized velocities and generalized coordinates are

$$\begin{aligned} \mathbf{H}(t) &= \tilde{\mathbf{H}} e^{j\omega t} \\ \mathbf{D}(t) &= \tilde{\mathbf{D}} e^{j\omega t} \end{aligned} \tag{4.1}$$

where t is time variable, and $\tilde{\mathbf{H}}$ and $\tilde{\mathbf{D}}$ denote the corresponding frequency dependent variables. The derived time domain discrete Hamilton's equations (3.28) and (3.29) are now expressed as

$$j\omega\tilde{\mathbf{P}} = -\mathbf{A}^T\,\mathbf{K}\,\tilde{\mathbf{D}} - \mathfrak{R}^m\,\mathbf{L}^{-1}\tilde{\mathbf{P}} + \tilde{\mathbf{f}}^s \tag{4.2}$$

$$j\omega\tilde{\mathbf{D}} = \quad \mathbf{A}\,\mathbf{L}^{-1}\,\tilde{\mathbf{P}} \quad - \mathfrak{C}^e\,\tilde{\mathbf{D}} - \tilde{\mathbf{J}}^s \tag{4.3}$$

where $\tilde{\mathbf{P}}$ is global column vector of discrete magnetic momenta, $\tilde{\mathbf{F}}$ is global column vector of discrete generalized forces, $\tilde{\mathbf{J}}^s$ is global column vector of electric impressed current sources, and $\tilde{\mathbf{f}}^s$ is global force vector. From equations (3.30) and (3.31), the magnetic momenta and electric conservative forces are

$$\tilde{\mathbf{P}} = \mathbf{L}\,\tilde{\mathbf{H}} \tag{4.4}$$

$$\tilde{\mathbf{F}} = \mathbf{K}\,\tilde{\mathbf{D}} \tag{4.5}$$

Assuming that magnetic and electric conductivities vanish, either electric field or magnetic field variables can be eliminated from the equations (4.2) and (4.3). They can be combined and written in terms of the magnetic field variable,

$$\mathbf{A}^T\,\mathbf{K}\,\mathbf{A}\,\mathbf{L}^{-1}\,\tilde{\mathbf{P}} - \omega^2\,\tilde{\mathbf{P}} = \mathbf{A}^T\,\mathbf{K}\,\tilde{\mathbf{J}}^s + j\omega\,\tilde{\mathbf{f}}^s \tag{4.6}$$

or expressed in terms of the electric field variable.

$$\mathbf{A}\,\mathbf{L}^{-1}\,\mathbf{A}^T\,\mathbf{K}\,\tilde{\mathbf{D}} - \omega^2\,\tilde{\mathbf{D}} = \mathbf{A}\,\mathbf{L}^{-1}\,\tilde{\mathbf{f}}^s - j\omega\,\tilde{\mathbf{J}}^s \tag{4.7}$$

where ω is a frequency (rad/s) and $j = \sqrt{-1}$. Equations (4.6) and (4.7) represent discrete Hamilton's equations, equivalent to the vector Helmholtz equations in the frequency domain. Note that similar expressions can be obtained for the dual formulation developed in Appendix A.

4.2.1 Open Boundary Conditions: Anisotropic Perfectly Matched Layer (PML) Boundary Condition

The anisotropic PML discussed in the previous chapter used to truncate the computational domain in time dependent problems, is also used to simulate open boundary electromagnetic problems in the frequency domain. The advantage of this method over other PML techniques is that it doesn't introduce a nonphysical split field and only requires a formulation that allows the use of anisotropic material properties. When considering a wave incident upon the interface between air and anisotropic PML as shown in figure (3.1), the tensor form of magnetic permeability (3.45) and electric permittivity (3.44) are analytically obtained [80]. The anisotropic PML concept is readily applied to the derived Hamiltonian equations (4.2), (4.3), (4.4) and (4.5), without further modification in frequency domain. Discrete Hamilton's equations with anisotropic PML have been developed for a plane wave incident on the interface between two different media as shown in figure (3.1). For the two regions, Hamilton's equations are

$$j\omega\tilde{\mathbf{P}} = -\mathbf{A}^T\,\mathbf{K}\,\tilde{\mathbf{D}} + \tilde{\mathbf{f}}^s \tag{4.8}$$

$$j\omega\tilde{\mathbf{D}} = \mathbf{A}\,\mathbf{L}^{-1}\tilde{\mathbf{P}} - \tilde{\mathbf{J}}^s \tag{4.9}$$

with the distributed parameter matrices for the air region

$$\mathbf{L}^{(i)} = \begin{bmatrix} \mathbf{L}_x^{(i)} & \mathbf{0} & \mathbf{0} \\ \mathbf{0} & \mathbf{L}_y^{(i)} & \mathbf{0} \\ \mathbf{0} & \mathbf{0} & \mathbf{L}_z^{(i)} \end{bmatrix} \tag{4.10}$$

$$\mathbf{K}^{(i)} = \begin{bmatrix} \mathbf{K}_x^{(i)} & \mathbf{0} & \mathbf{0} \\ \mathbf{0} & \mathbf{K}_y^{(i)} & \mathbf{0} \\ \mathbf{0} & \mathbf{0} & \mathbf{K}_z^{(i)} \end{bmatrix} \tag{4.11}$$

For the anisotropic PML region, the complex parameter matrices defined in equations (3.67) and (3.69) are used

$$\mathbf{L}^{(i)*} = \begin{bmatrix} \left(1+\frac{\sigma}{j\omega\epsilon_1}\right)^{-1}\mathbf{L}_x^{(i)} & \mathbf{0} & \mathbf{0} \\ \mathbf{0} & \left(1+\frac{\sigma}{j\omega\epsilon_1}\right)\mathbf{L}_y^{(i)} & \mathbf{0} \\ \mathbf{0} & \mathbf{0} & \left(1+\frac{\sigma}{j\omega\epsilon_1}\right)\mathbf{L}_z^{(i)} \end{bmatrix} \tag{4.12}$$

$$\mathbf{K}^{(i)*} = \begin{bmatrix} \left(1+\frac{\sigma}{j\omega\epsilon_1}\right)\mathbf{K}_x^{(i)} & \mathbf{0} & \mathbf{0} \\ \mathbf{0} & \left(1+\frac{\sigma}{j\omega\epsilon_1}\right)^{-1}\mathbf{K}_y^{(i)} & \mathbf{0} \\ \mathbf{0} & \mathbf{0} & \left(1+\frac{\sigma}{j\omega\epsilon_1}\right)^{-1}\mathbf{K}_z^{(i)} \end{bmatrix} \tag{4.13}$$

The main advantages of this artificial layer are that it is independent of the incident angle, polarization and frequency of the waves.

4.2.2 Example Problems for Electromagnetic Systems in Frequency Domain

In this section, the formulation in the frequency domain is validated by calculating cutoff frequencies in a two dimensional cross-section of a homogeneous waveguide and the resonant frequencies of a three dimensional inhomogeneous cavity with closed boundaries. These problems were selected from the literature [77][20]. The test problem involving biological tissues, simulated in the preceding chapter, is used here to test the derived formulation in the frequency domain.

4.2.2.1 Two Dimensional Homogeneous Rectangular Waveguide

This example calculates the cutoff wave numbers over the cross section of a rectangular waveguide, for the transverse magnetic (TM) mode and the transverse electric (TE) mode, which are reduced to two dimensional eigenvalue problems. The former mode calculates eigenvalues for E_z, H_x, and H_y while the latter computes eigenvalues associated with H_z, E_x, and E_y. Exact solutions of these problems are available for waveguides whose cross section is rectangular or circular [77][5][21]. The cutoff wave numbers for an air-filled rectangular waveguide with a ratio of width to height (a/b) of two are solved here, the geometry of waveguide is shown in figure (4.1). In this simulation, the conductivities are zero, the relative permeability and permittivity are unity, and the current source in equation (4.6) is zero. This example requires separate simulations for the TM and TE modes with perfect electric conductor boundary conditions. For the TM mode problem, equations (4.2) and (4.3) are combined to obtain a discrete formulation (4.7) equivalent to the vector Helmholtz equation. The eigenvalue problem is

$$\left[\mathbf{T}^{TM}\right]\ \tilde{\mathbf{D}} = \lambda\,\tilde{\mathbf{D}} \tag{4.14}$$

where

$$\begin{aligned} \left[\mathbf{T}^{TM}\right] &= \mathbf{A}\,\mathbf{L}^{-1}\,\mathbf{A}^{T}\,\mathbf{K} \\ \lambda &= \omega^{2} \end{aligned} \tag{4.15}$$

with PEC boundary condition

$$E_z = 0 \qquad \begin{cases} \text{at } x = 0 \quad \text{and} \quad x = a \\ \text{at } y = 0 \quad \text{and} \quad y = b \end{cases} \tag{4.16}$$

Note that $\left[\mathbf{T}^{TM}\right]$ is $n_f \times n_f$ matrix with n_f being the total number of faces.

For the TE mode, the dual formulation derived in Appendix A formulates the eigenvalue problem in terms of the electric field by

$$\left[\mathbf{T}^{TE}\right] \ \tilde{\mathbf{X}} = \lambda \, \tilde{\mathbf{X}} \tag{4.17}$$

with

$$\begin{aligned} \left[\mathbf{T}^{TE}\right] &= \mathbf{A}^T \, \mathbf{R} \, \mathbf{A} \, \mathbf{C}^{-1} \\ \lambda &= \omega^2 \end{aligned} \tag{4.18}$$

where $\left[\mathbf{T}^{TE}\right]$ is $n_s \times n_s$ matrix with n_s being the total number of edges, $\tilde{\mathbf{X}}$ is a column vector of electric momenta, $\mathbf{R}$ is a reluctance matrix, and $\mathbf{C}$ is a global capacitance matrix, all defined in Appendix A. The PEC boundary condition is

$$E_x = 0 \qquad \text{at } y = 0 \text{ and } \quad y = b \tag{4.19}$$

$$E_y = 0 \qquad \text{at } x = 0 \text{ and } \quad x = a \tag{4.20}$$

The cross section of the rectangular waveguide is discretized using 1,058 uniform square elements having 2,185 edges and 1,058 faces. The tenth lowest cutoff wave numbers are numerically solved using the aforementioned formulations and compared with the exact solutions. The results for TM modes are tabulated in table (4.1). They are in excellent agreement with the exact solutions, the maximum error was found to be less than 0.680% for the ninth lowest mode. Table (4.2) shows the numerically computed results for TE modes, they agree very well with the exact solutions.

4.2.2.2 The Penetration and Scattering of Electromagnetic Fields on Two Dimensional Circular Cylinder Biological Tissues

The scattering problem discussed in chapter three is used here to validate the frequency domain model. The electric fields in the inside of circular cylinder biological tissues are calculated along the x-axis and y-axis. Here equation (4.7) is rewritten as

$$\mathbf{A}\,\mathbf{L}^{-1}\,\mathbf{A}^{T}\,\mathbf{K}\,\tilde{\mathbf{D}} - \omega^{2}\,\tilde{\mathbf{D}} = \mathbf{A}\,\mathbf{L}^{-1}\,\tilde{\mathbf{f}}^{s} \tag{4.21}$$

where $\tilde{\mathbf{f}}^{s}$ is the global force vector, determined by the incident electric field

$$\tilde{\mathbf{E}}^{s} = E_0 e^{-jk_0 x}\,\vec{\mathbf{a}}_z \tag{4.22}$$

where E_0 is the amplitude of the incident plane wave, k_0 is the propagation constant in free space, and $\hat{\mathbf{a}}_z$ is unit vector in the z-direction. The complex inductance and elastance matrices vary, depending on each region, as numbered in the figure (B.1). They are summarized below.

In the main problem domain, there are two separate regions (air and lossy dielectric material). For the air region ($\sigma^{e} = 0$ and $\sigma^{m} = 0$), the inductance and elastance matrices are

$$\begin{aligned} \mathbf{L}^{(i)} &= \mathbf{L}^{(i)} \\ \mathbf{K}^{(i)} &= \mathbf{K}^{(i)} \end{aligned} \tag{4.23}$$

while for the lossy dielectric region ($\sigma^e \neq 0$ and $\sigma^m = 0$), they are

$$\begin{aligned} \mathbf{L}^{(i)} &= \mathbf{L}^{(i)} \\ \mathbf{K}^{(i)} &= \mathbf{K}^{(i)*} = (1 + \frac{\sigma^e}{j\omega\epsilon})^{-1}\mathbf{K}^{(i)} \end{aligned} \tag{4.24}$$

where σ^e is the electric conductivity of the lossy dielectric material.

As shown in figure (B.1), the two dimensional anisotropic PML is divided into three regions, whose numerical parameters are different. They are summarized in the below.

In region 1,

$$\begin{aligned} \mathbf{L}^{(i)} &= \mathbf{L}^{(i)*} = \begin{bmatrix} \left(1 + \frac{\sigma_x}{j\omega\epsilon_1}\right)^{-1} \mathbf{L}_x^{(i)} & \mathbf{0} \\ \mathbf{0} & \left(1 + \frac{\sigma_x}{j\omega\epsilon_1}\right) \mathbf{L}_y^{(i)} \end{bmatrix} \\ \mathbf{K}^{(i)} &= \mathbf{K}^{(i)*} = \left[\left(1 + \frac{\sigma_x}{j\omega\epsilon_1}\right)^{-1} \mathbf{K}_z^{(i)}\right] \end{aligned} \tag{4.25}$$

where σ_x represents the conductivity associated with the x-direction and ϵ_1 is the permittivity of the air.

In region 2,

$$\begin{aligned} \mathbf{L}^{(i)} &= \mathbf{L}^{(i)*} = \begin{bmatrix} \left(1 + \frac{\sigma_y}{j\omega\epsilon_1}\right) \mathbf{L}_x^{(i)} & \mathbf{0} \\ \mathbf{0} & \left(1 + \frac{\sigma_y}{j\omega\epsilon_1}\right)^{-1} \mathbf{L}_y^{(i)} \end{bmatrix} \\ \mathbf{K}^{(i)} &= \mathbf{K}^{(i)*} = \left[\left(1 + \frac{\sigma_y}{j\omega\epsilon_1}\right)^{-1} \mathbf{K}_z^{(i)}\right] \end{aligned} \tag{4.26}$$

where σ_y denotes the conductivity associated with the y-direction.

In region 3,

$$\mathbf{L}^{(i)} = \mathbf{L}^{(i)*} = \begin{bmatrix} \left(1+\frac{\sigma_x}{j\omega\epsilon_1}\right)^{-1}\left(1+\frac{\sigma_y}{j\omega\epsilon_1}\right)\mathbf{L}_x^{(i)} & 0 \\ 0 & \left(1+\frac{\sigma_x}{j\omega\epsilon_1}\right)\left(1+\frac{\sigma_y}{j\omega\epsilon_1}\right)^{-1}\mathbf{L}_y^{(i)} \end{bmatrix}$$

$$\mathbf{K}^{(i)} = \mathbf{K}^{(i)*} = \left[\left(1+\frac{\sigma_x}{j\omega\epsilon_1}\right)^{-1}\left(1+\frac{\sigma_y}{j\omega\epsilon_1}\right)^{-1}\mathbf{K}_z^{(i)}\right] \tag{4.27}$$

The computational domain is discretized using 14,641 rectangular elements for 100Mhz incident waves in both the homogeneous and inhomogeneous cases, and 36,481 rectangular elements for 300MHz waves in the homogeneous case. Both models used 20 elements per wavelength. Figures (4.2) and (4.3) show a comparison of the numerical solutions computed in the frequency domain with the corresponding exact solutions. Figure (4.4) compares the numerical results with the exact solutions for the inhomogeneous model. They show very good agreement for both cases.

4.2.2.3 Three Dimensional Inhomogeneous Cavity Problem

To investigate the derived formulations further, in a three dimensional inhomogeneous problem, a partially filled cavity example [20][94] was selected and solved. This example has exact solutions available in the literature [20] which allow us to directly evaluate the computed results. Note that the calculation of resonant frequencies in three dimensional cavities has been problematic, due to spurious modes, for many years when using conventional finite element methods [77][49]. In addition, the discontinuity in the material interface needs to be properly treated. Equations (4.2) and (4.3) are used to formulate a three dimensional eigenvalue problem, with perfect conductor boundary conditions

$$\left\{\begin{array}{llll} E_y = 0, \text{ and } E_z = 0, & \text{at } x = 0 & \text{and} & x = a \\ E_x = 0, \text{ and } E_z = 0, & \text{at } y = 0 & \text{and} & y = b \\ E_x = 0, \text{ and } E_y = 0, & \text{at } z = 0 & \text{and} & z = c \end{array}\right. \tag{4.28}$$

Equations (4.2) and (4.3) are combined to produce a discrete Hamilton's formulation equivalent to the vector Helmholtz equation. The form of the eigenvalue problem is

$$[\mathbf{T}]\,\tilde{\mathbf{D}} = \lambda\,\tilde{\mathbf{D}} \tag{4.29}$$

with

$$\begin{aligned} [\mathbf{T}] &= \mathbf{A}\,\mathbf{L}^{-1}\,\mathbf{A}^T\,\mathbf{K} \\ \lambda &= \omega^2 \end{aligned} \tag{4.30}$$

where $[\mathbf{T}]$ is $n_f \times n_f$ matrix with n_f being the total number of faces in the system.

The partially filled rectangular cavity is half filled with a dielectric material of relative permittivity ($\epsilon_r = 2$); the cavity geometry ($1 \times 0.1 \times 1$) is shown in figure (4.5). Three dimensional brick elements (2,700) composed of 10,323 edges and 9,180 faces were used to discretize the computational domain. Edge elements are used to impose a divergence free condition on the magnetic fields, so that nonphysical spurious modes are avoided. Since face elements guarantee normal continuity of the electric flux density ($\mathbf{D}$) on element interfaces, no special treatment is needed on material interfaces between two different dielectric materials. The results of the simulation are compared with exact solutions in table (4.4), which shows very good agreement.

4.3 Discrete Hamilton's Equations for Magnetostatic Systems

In the static case, the time varying terms of the discrete Hamilton's equations derived in chapter three vanish, and the electric and magnetic field variables become independent. The magnetostatic equations only are considered in this dissertation, since the electrostatic problem is commonly treated as a dual of the magnetostatic case. The magnetostatic equation alone does not guarantee a divergence free condition. The most common solution to this problem is the introduction of a magnetic vector potential, whose curl is the magnetic flux density[19].

4.3.1 Interpolation Functions

This dissertation employs edges and face interpolation functions, with either rectangular elements for two dimensional problems or hexahedral brick elements for three dimensional problems. These elements are well known and have been discussed in the previous chapters. In the magnetostatic case, magnetic fields are decoupled from electric fields and a magnetic vector potential function is introduced to satisfy the divergence free condition. This new vector variable is assumed to be a piecewise constant on the element faces.

4.3.2 Discrete Hamilton's Equations

In the static case, equation (3.29) reduces to

$$\mathbf{J} = \mathbf{A}\,\mathbf{L}^{-1}\,\mathbf{P} \tag{4.31}$$

with constitutive relation

$$\mathbf{P} = \mathbf{L}\,\mathbf{H} \tag{4.32}$$

Using the discrete curl operator derived in chapter 2, the magnetic momenta ($\mathbf{P}$) can be represented in vector potential form by

$$\mathbf{P} = \mathbf{A}^T \boldsymbol{\mathcal{A}} \tag{4.33}$$

where $\mathbf{A}$ performs the curl operation, and $\boldsymbol{\mathcal{A}}$ is column vector of magnetic vector potentials. New equations (4.31) and (4.33) are assembled to form the linear system

$$\left[\begin{array}{c|c} \mathbf{A}\,\mathbf{L}^{-1} & \mathbf{0} \\ \hline \mathbf{I} & -\mathbf{A}^T \end{array}\right] \left[\begin{array}{c} \mathbf{P} \\ \hline \boldsymbol{\mathcal{A}} \end{array}\right] = \left[\begin{array}{c} \mathbf{J} \\ \hline \mathbf{0} \end{array}\right] \tag{4.34}$$

where $\mathbf{I}$ is identity matrix. The magnetic vector potential is used to only guarantee a divergence free condition, and the magnetic field variables are calculated directly from equation (4.34). Therefore, a gauge condition is not introduced in the calculations.

4.3.3 Example Problems for Magnetostatic Systems

4.3.3.1 Coaxial Cable

The first example models an infinitely long coaxial transmission line, and validates the formulation in a magnetostatic case. The coaxial cable is composed of two conducting materials, laid on a concentric axis, and carries a steady current I in the inner conductor and -I in the outer conductor, as shown in figure (4.6). The geometry of this problem is cylindrically symmetry, so that the magnetic flux density is a function only of radius (ρ). The exact magnetic field distribution is analytically calculated using Ampere's circuital law [41][21]. The exact solution is

$$\begin{aligned} H_\phi &= \frac{I\rho}{2\pi a^2} && (\rho < a) \\ H_\phi &= \frac{I}{2\pi\rho} && (a < \rho < b) \\ H_\phi &= \frac{I}{2\pi\rho}\frac{c^2-\rho^2}{c^2-b^2} && (b < \rho < c) \\ H_\phi &= 0 && (\rho > c) \end{aligned} \tag{4.35}$$

where H_ϕ is the magnetic field intensity (A/m) in the ϕ direction, a is the radius of the inner conductor, b is the inner radius of the outer conductor, and c is the outer radius of the outer conductor. Numerical parameters are listed in table (4.5). The circular interfaces between the conductor and air are discretized approximately by the use of rectangular elements, referred to as a staircase approximation. As shown in figure (4.7), 185 elements are used to model the inner conductor region and 1,284 elements are used to model outer conductor region. The total number of elements used to simulate this problem is 3,721, which enables interpolation of the magnetic fields by 7,564 edges and the vector potential by 3,721 faces. Figure (4.8) shows a comparison of the numerical solutions with the exact solutions. Although some errors are observed at the interfaces between the conductors and the air, due to the staircase approximation, good agreement is shown.

4.3.3.2 Magnetic Shielding

The second example solves the magnetic shielding problem of Brezzi et al. [16], and validates the proposed formulation in a magnetostatic problem involving a strong discontinuity in material properties at an interface. The problem has four subregions, composed of conductor, air, and magnetic shield material. The problem geometry and boundary conditions are shown in figure (4.9). The exact solution is given by Ampere's circuital law

$$\begin{aligned} B_y &= \mu_0 \, J \, x & (x < 0.03) \\ B_y &= 0.03 \, \mu_0 \, J & (0.03 < x < 0.06) \\ B_y &= 0.03 \, \mu_1 \, J & (0.06 < x < 0.07) \\ B_y &= 0.03 \, \mu_0 \, J & (0.07 < x < 0.1) \end{aligned} \tag{4.36}$$

where B_y is magnetic density in the y direction, J ($5 \times 10^5 \ A/m^2$) is the current density of the electrical conductor, μ_0 ($4\pi \times 10^{-7} \ H/m$) is the magnetic permeability of air, and μ_1 is the magnetic permeability of the magnetic shield material. Numerical oscillation of the fields in the air region between the conductor and the magnetic shield is reported to be a problem when the nodal based finite element method is used [16]. Calculations were performed for two different relative permeabilities (10 and 10^6) of magnetic shield material. The computational domain was discretized by 1,600 square elements (3280 edges and 1600 faces). Figures (4.10) and (4.11) show very good agreement between the numerical and exact solutions.

4.4 Conclusion

To validate the new numerical technique in the frequency domain, eigenvalue problems for a two dimensional waveguide and a three dimensional half filled rectangular cavity were formulated, with closed boundary conditions. Penetration and scattering of electromagnetic fields in biological tissues are modeled to test infinite domain boundary conditions. The numerical solutions show good agreement with the exact solutions in all cases.

For magnetostatic systems, a vector magnetic potential was introduced and interpolated by face elements. Numerical results show good agreement with analytical solutions for the test problems.

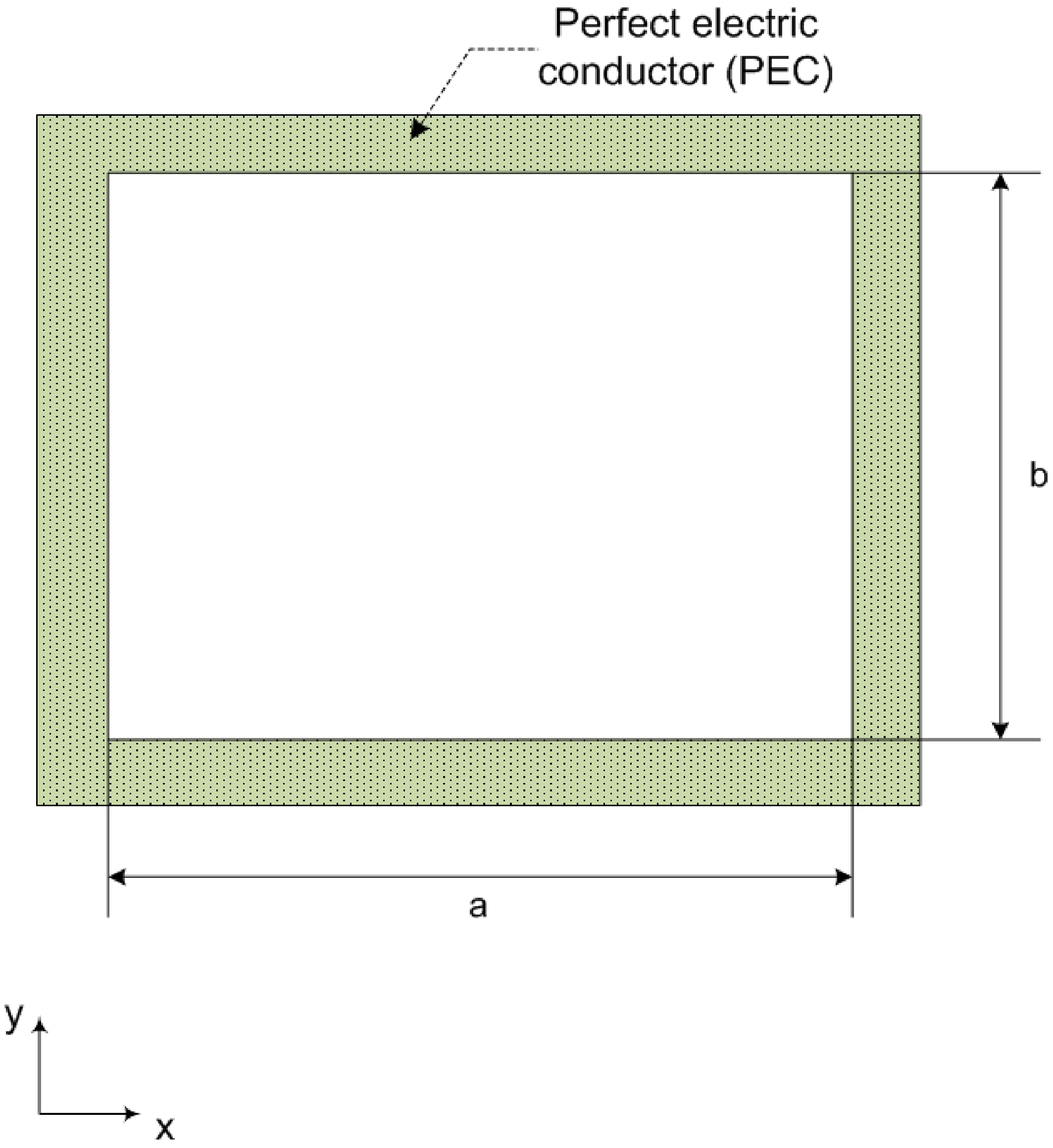

Figure 4.1: The cross section of rectangular waveguide

TM mode			
	$k_c a$		
Mode	exact	DHM	|error| (%)
TM_{11}	7.025	7.029	0.057
TM_{21}	8.886	8.892	0.067
TM_{31}	11.327	11.343	0.141
TM_{12}	12.953	12.991	0.293
TM_{22}, TM_{41}	14.049	14.086	0.263
TM_{32}	15.708	15.749	0.261
TM_{51}	16.918	16.990	0.425
TM_{42}	17.771	17.827	0.315
TM_{13}	19.110	19.240	0.680
TM_{23}, TM_{61}	19.869	19.996	0.639

Table 4.1: Cutoff wave numbers ($k_c a$) calculated by discrete Hamilton's method (DHM) for rectangular waveguide ($\frac{a}{b} = 2$)

TE modes			
	$k_c a$		
Mode	exact	DHM	|error| (%)
TE_{10}	3.142	3.142	0
TE_{20}, TE_{01}	6.283	6.288	0.079
TE_{11}	7.025	7.030	0.071
TE_{21}	8.886	8.893	0.078
TE_{30}	9.425	9.443	0.191
TE_{31}	11.327	11.345	0.158
TE_{40}, TE_{02}	12.566	12.609	0.342
TE_{12}	12.953	12.995	0.324
TE_{22}, TE_{41}	14.050	14.090	0.285
TE_{32}	15.708	15.753	0.286

Table 4.2: Cutoff wave numbers ($k_c a$) calculated by dual formulation for rectangular waveguide ($\frac{a}{b} = 2$)

Parameters	Homogeneous tissue		Inhomogeneous tissue	
	100MHz	300MHz	100MHz	
	Muscle	Muscle	Muscle	Fat
Dielectric constant	$\epsilon_r = 72$	$\epsilon_r = 54$	$\epsilon_r = 72$	$\epsilon_r = 7.5$
Conductivity (S/m)	$\sigma = 0.9$	$\sigma = 1.4$	$\sigma = 0.9$	$\sigma = 0.048$

Table 4.3: Dielectric material properties of homogeneous muscle and inhomogeneous muscle-fat tissues [50]

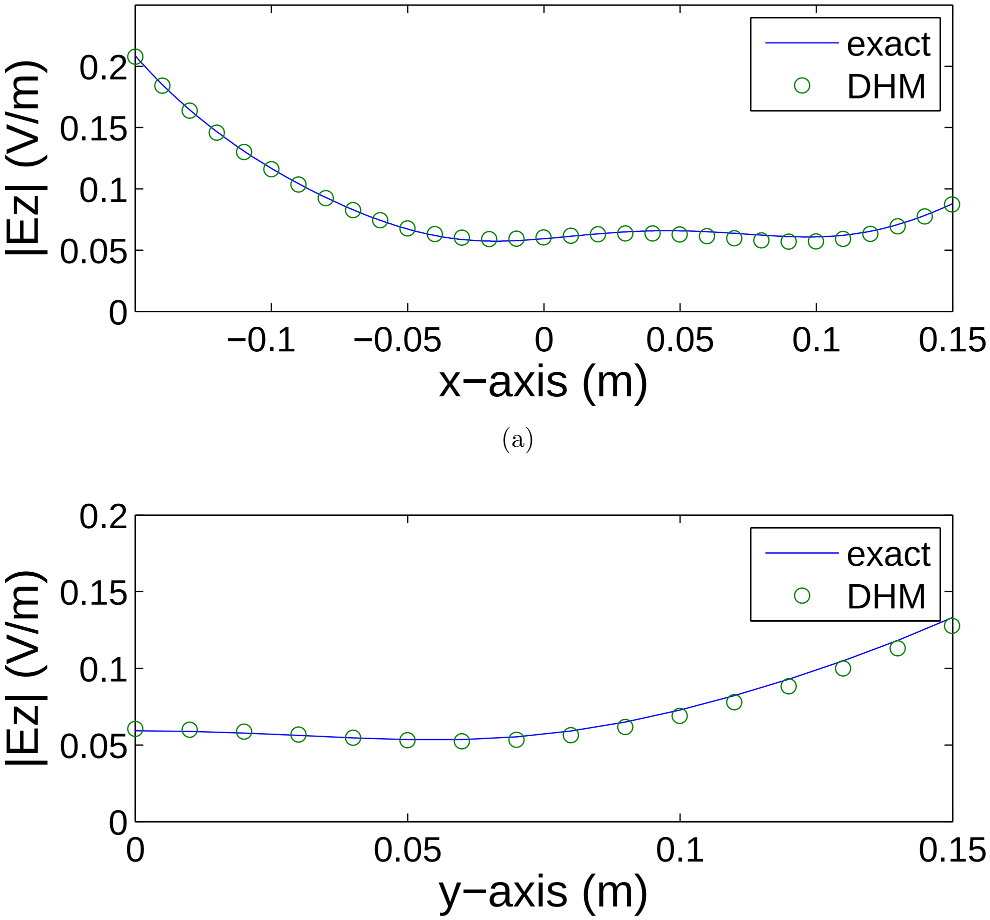

(a)

(b)

Figure 4.2: Comparison of numerical results calculated by discrete Hamilton's method (DHM) in frequency domain with exact solutions along (a) x-axis and (b) y-axis for homogeneous muscle cylinder exposed to incident field of 100 MHz frequency

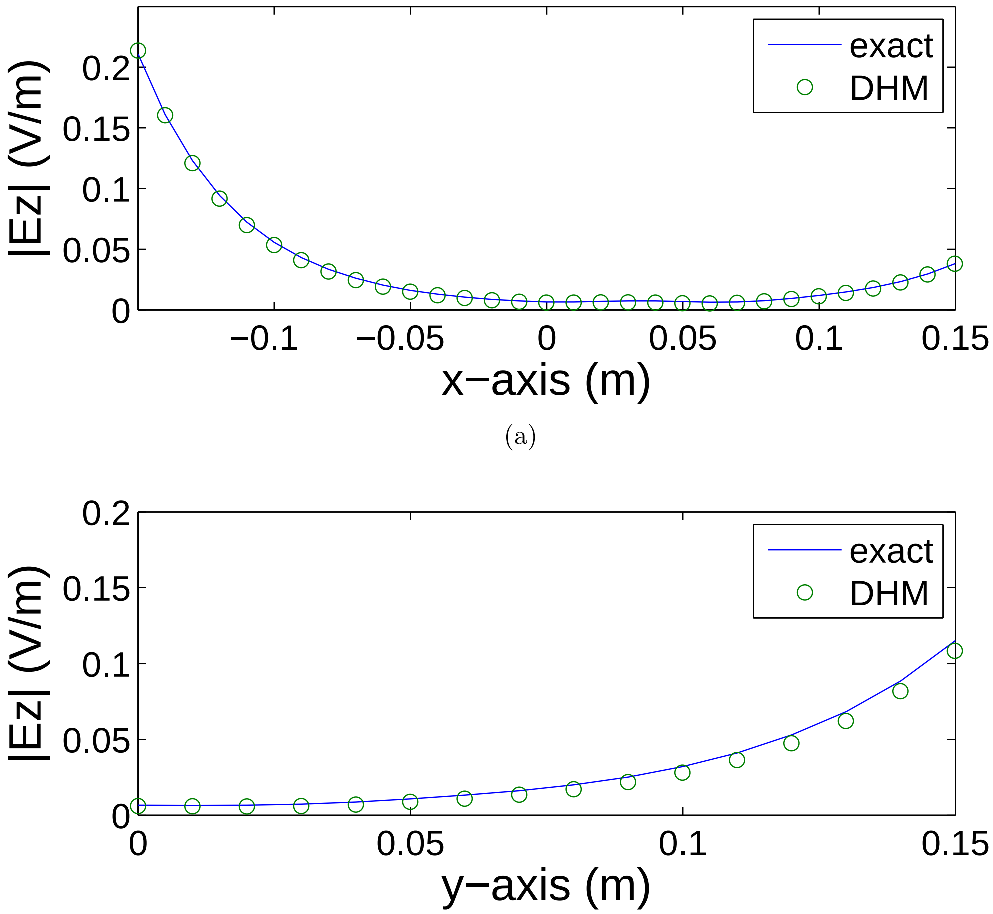

(a)

(b)

Figure 4.3: Comparison of numerical results calculated by discrete Hamilton's method (DHM) in frequency domain with exact solutions along (a) x-axis and (b) y-axis for homogeneous muscle cylinder exposed to incident field of 300 MHz frequency

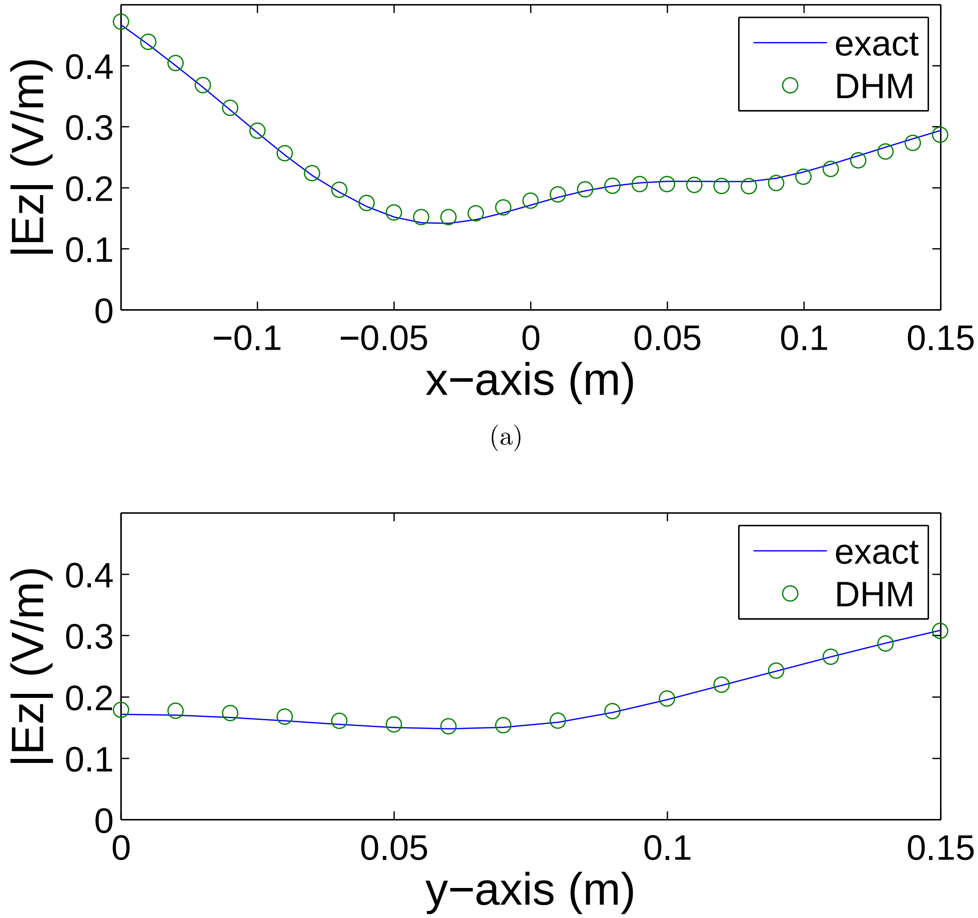

(a)

(b)

Figure 4.4: Comparison of numerical results calculated by discrete Hamilton's method (DHM) in frequency domain with exact solutions along (a) x-axis and (b) y-axis for inhomogeneous two layered muscle-fat cylinder exposed to incident field of 100 MHz frequency

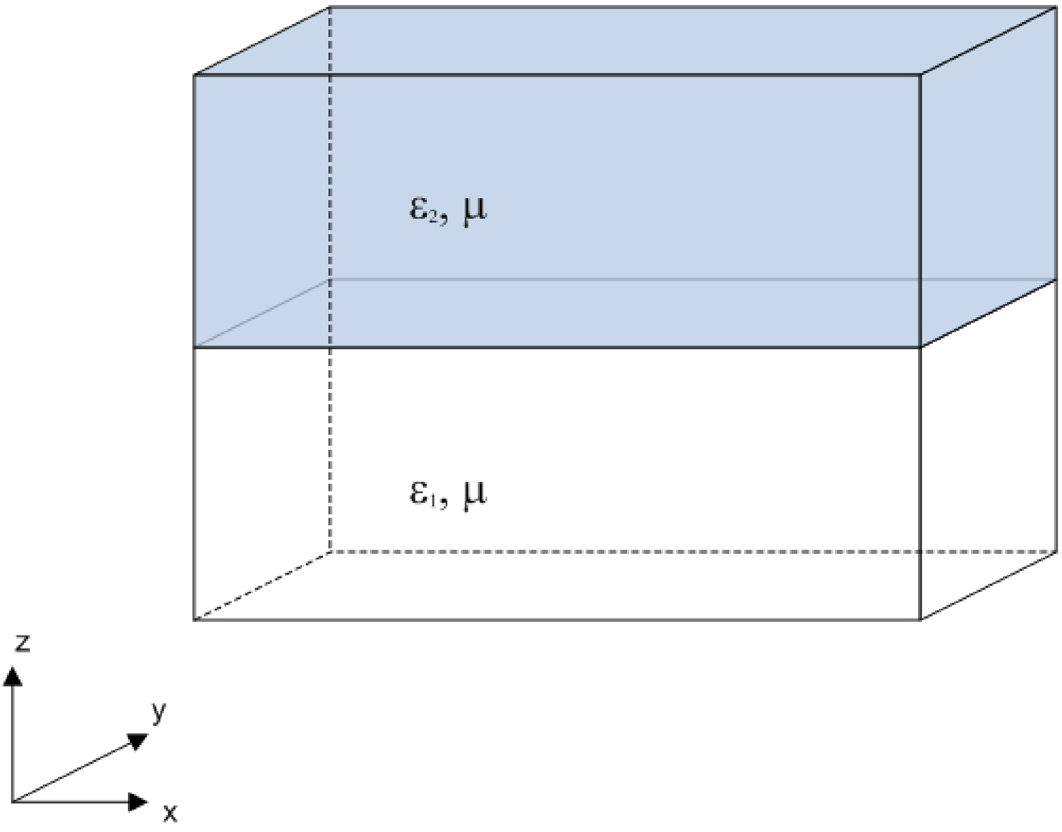

Figure 4.5: Three dimensional half filled rectangular cavity configuration

Eigenvalues (k_0, cm^{-1})			
Mode	Analytical [20]	DHM	|error| (%)
$TE_{Z_{101}}$	3.538	3.542	0.11
$TE_{Z_{201}}$	5.445	5.463	0.33
$TE_{Z_{102}}$	5.935	6.024	1.49
$TE_{Z_{301}}$	7.503	7.563	0.80
$TE_{Z_{202}}$	7.633	7.675	0.55
$TE_{Z_{103}}$	8.096	8.164	1.78

Table 4.4: Three dimensional inhomogeneous cavity resonance frequencies

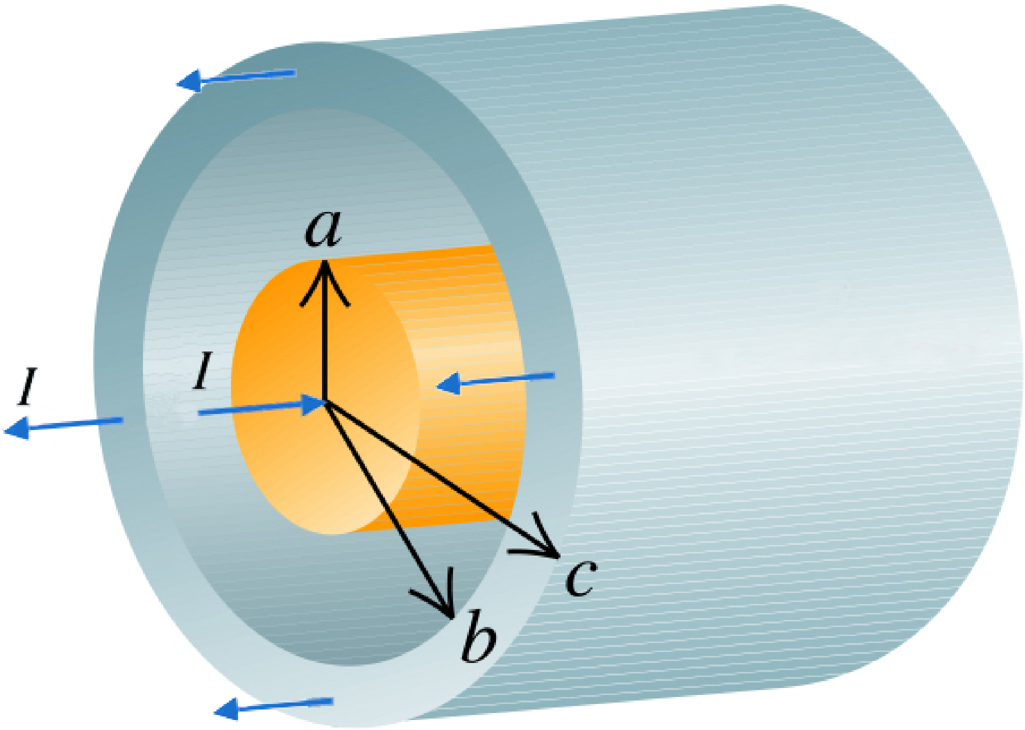

Figure 4.6: Circular coaxial cable [41]

Parameters	Value
Current flowing in the conductor	$I = 1$ (A)
Radius of inner conductor	$a = 1(m)$
Inner radius of outer conductor	$b = 3\ (m)$
outer radius of outer conductor	$c = 4\ (m)$
Permeability of air	$\mu = 1$ (H/m)

Table 4.5: Simulation parameters for coaxial cable example

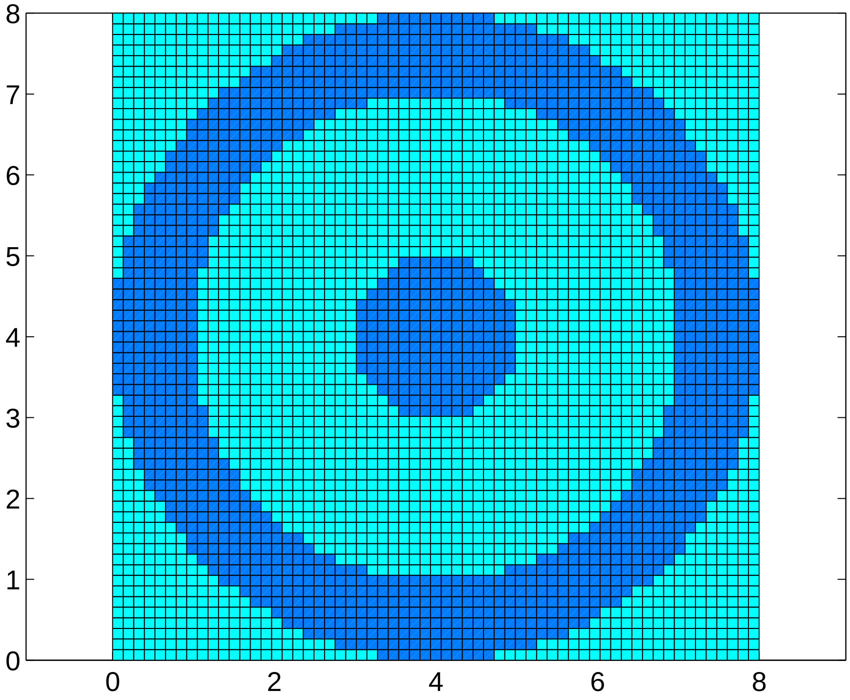

Figure 4.7: Mesh generation for the circular coaxial cable

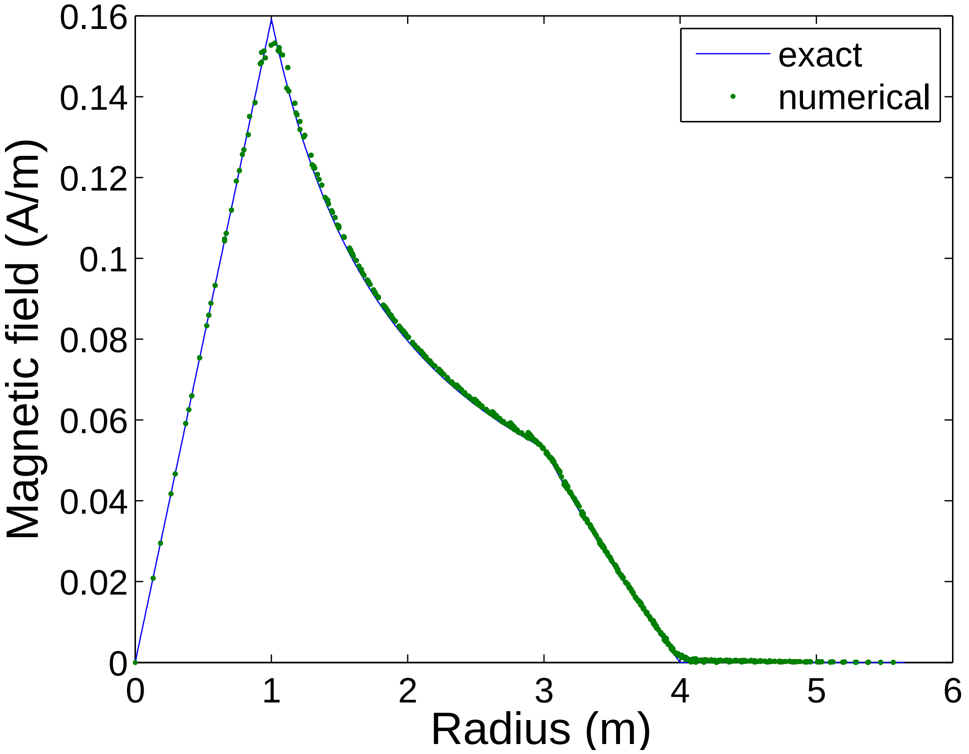

Figure 4.8: Comparison of magnetic field (H_ϕ) computed by discrete Hamilton's method (DHM) with the exact solution in the cross section of circular coaxial cable.

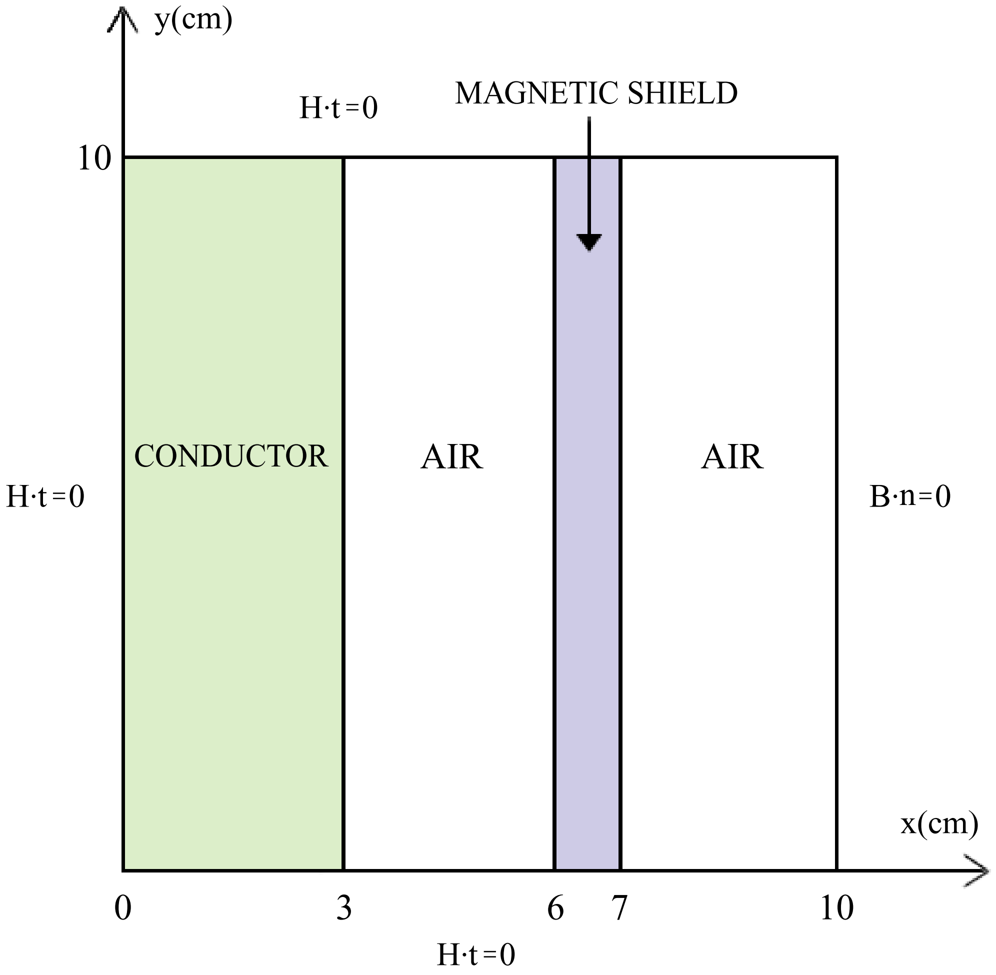

Figure 4.9: The configuration of magnetic shield problem with boundary conditions [16]

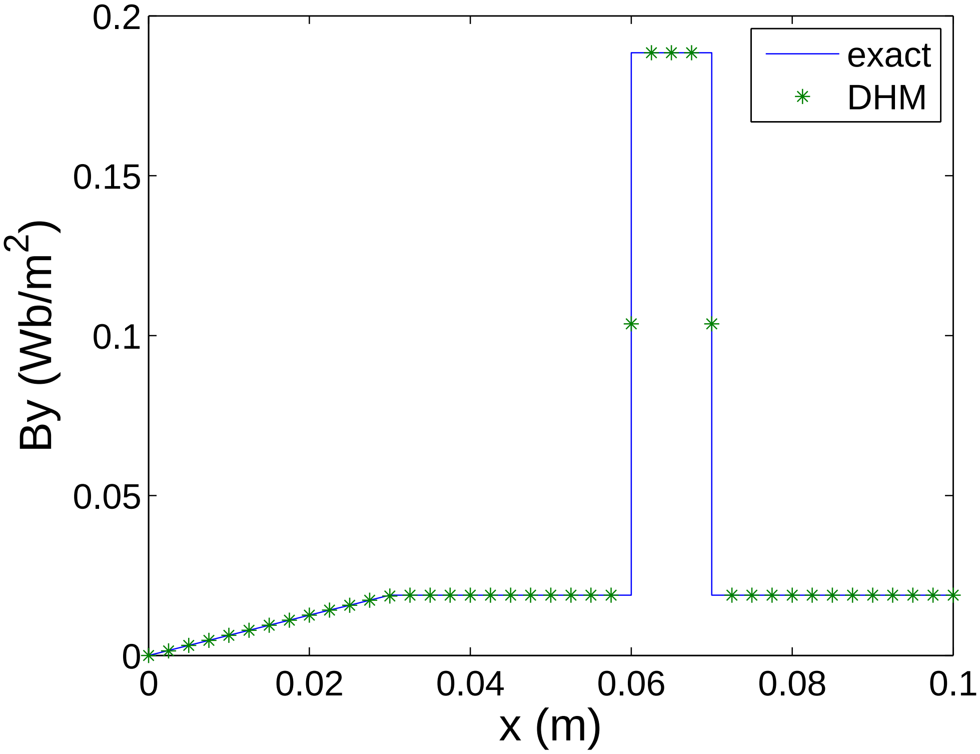

Figure 4.10: Comparison of Magnetic field density (B_y) calculated by discrete Hamiltonian method (DHM) with the exact analytical solution at y = 5(m), where the relative permeability (μ_r) of the magnetic shield material is 10

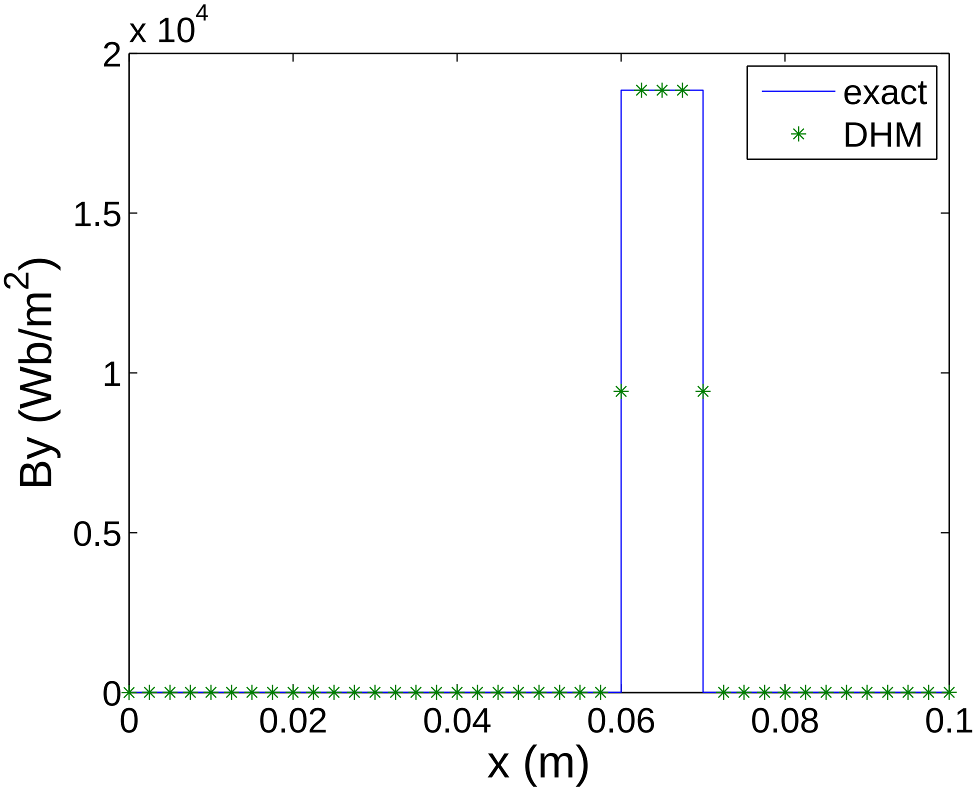

Figure 4.11: Comparison of Magnetic field density (B_y) calculated by Discrete Hamiltonian Method (DHM) with the exact analytical solution at y = 5(m), where the relative permeability (μ_r) of the magnetic shield material is 10^6

Chapter 5

Conclusion and Future Work

Extending previous work of Koo and Fahrenthold [57] and Horban and Fahrenthold [44], this dissertation has developed a new discrete energy method for electromagnetic and thermo-electromagnetic modeling. Anisotropic PML implementation has been developed for the derived formulation to be applied to infinite domain electromagnetic problems. The discrete Hamilton's equations developed in the time domain were specialized and validated in magnetostatic and frequency domain electromagnetic problems.

Most alternative numerical methods, such as finite difference time domain methods or finite element methods, are based on partial differential equations and have well known advantages and disadvantages. This has resulted in the application of different techniques to distinct classes of electromagnetic problems. The numerical method described here employed edge and face type interpolations for the field variables. The magnetic and potential energies defined a Hamiltonian for the system, and a discrete Ampere's equation provides nonholonomic constraints. We construct a discrete system of equations by employing system dynamics techniques, specifically a Hamiltonian methodology. This procedure precludes the use of partial differential equations. An anisotropic PML is incorporated into the system model for open boundary problems, to truncate the computational domain. Internal energy variables are introduced as a generalized coordinates in order to include general thermodynamics in the formulation, coupling the thermal and electromagnetic energy domains. This formulation allows for extending Hamiltonian methods to complex multi-energy domain systems. This research formulated and validated new discrete Hamiltonian methods for electromagnetic systems in order to provide an essential component of a unified Hamiltonian modeling approach for distributed electromechanical systems.

Additional research is suggested. It should include further development of the proposed discrete energy method, for coupling of electromagnetic and mechanical systems. This will lead to advances in systems modeling methods for complex multi-energy domain systems, such as MEMS actuators, magnetohydrodynamic systems, biological systems, and Z-pinch machines [1]. The results presented here should be further developed to model problems with complex geometry, including the use of edge and face interpolation functions in triangular elements for two dimensional problems and tetrahedral elements for three dimensional problems. Although the accuracy of the proposed formulation has been validated in several example problems, further numerical simulations may be performed to investigate convergence rates and obtain better accuracy at higher mesh resolutions. A new implementation of anisotropic PML has been developed here, to solve infinite domain electromagnetic problems. The numerical results were good, however the implementation introduces additional state variables and associated evolution equations. Further development aimed at producing an explicit formulation is desirable.

Appendices

Appendix A

Dual Formulation

The formulation developed in the previous chapters is well suited to TM mode problems. An alternative formulation, which will be referred to as a "dual formulation", is required to assign electric field intensity variables to the edges and magnetic flux density to the faces as shown in figure (A.1). In this formulation, electric co-energy is expressed in terms of electric field intensity and magnetic potential energy is represented in terms of magnetic flux density.

A.1 Interpolation Functions

In the dual formulation, the discretization of the modeled control volume is performed using face and edge type finite elements like those used in previous chapters [49][79]. However, face basis functions are used to interpolate the magnetic displacement, in terms of discrete generalized coordinates, while edge basis functions are used to interpolate the electric field intensity, in terms of discrete generalized quasi-velocities.

A.1.1 Electric Field Intensity: Edge Elements

The electric field intensity for element 'i' is [49][79]

$$\vec{\mathbf{E}}^{(i)} = \sum_{j=1}^{n_{es}} \vec{\mathbf{w}}_j^{(i)} \; E_j^{(i)} = \mathbf{w}^{(i)T} \; \mathbf{E}^{(i)} \tag{A.1}$$

with

$$\mathbf{w}^{(i)} = [\vec{\mathbf{w}}_1 \; \vec{\mathbf{w}}_2 \; \vec{\mathbf{w}}_3 \; ... \; \vec{\mathbf{w}}_{12}]^T \tag{A.2}$$

$$\mathbf{E}^{(i)} = [E_1 \; E_2 \; E_3 \; ... \; E_{12}]^T \tag{A.3}$$

where n_{es} is number of edges in the element, $\vec{\mathbf{w}}_j^{(i)}$ is vector interpolation function at edge 'j' on element 'i', $\vec{\mathbf{E}}^{(i)}$ is electric intensity field in the 'i'th element, and T denotes the transpose.

A.1.2 Magnetic Flux Density: Face Elements

The magnetic flux density in the element can be described by [79]

$$\vec{\mathbf{B}}^{(i)} = \sum_{j=1}^{n_{ef}} \vec{\mathbf{f}}_j^{(i)} B_j^{(i)} = \mathbf{f}^{(i)T} \; \mathbf{B}^{(i)} \tag{A.4}$$

with

$$\mathbf{f}^{(i)} = [\vec{\mathbf{f}}_1 \; \vec{\mathbf{f}}_2 \; \vec{\mathbf{f}}_3 \; ... \; \vec{\mathbf{f}}_6]^T \tag{A.5}$$

$$\mathbf{B}^{(i)} = [B_1 \; B_2 \; B_3 \; ... \; B_6]^T \tag{A.6}$$

where n_{ef} is number of faces in the element, $\vec{\mathbf{f}}_j^{(i)}$ is vector interpolation function at face 'j' on element 'i', $\vec{\mathbf{B}}^{(i)}$ is magnetic flux density in the 'i'th element.

A.2 Electric Co-energy

The electric co-energy (T^{e*}) is defined as

$$T^{e*} = \frac{1}{2} \int_v \epsilon\, \vec{\mathbf{E}} \cdot \vec{\mathbf{E}}\, dv \tag{A.7}$$

where ϵ is electric permittivity. The generalized quasi-velocity assigned to each edge is used to obtain a discrete form of the electric co-energy function. The system electric co-energy is the sum of the element co-energies and is represented by

$$T^{e*} = \frac{1}{2} \sum_{i=1}^{n_e} \mathbf{E}^{(i)T}\, \mathbf{C}^{(i)}\, \mathbf{E}^{(i)} \tag{A.8}$$

where the index n_e is the number of elements, $\mathbf{E}^{(i)}$ is column vector of the tangential electric intensity values on the edges of the 'ith element, and $\mathbf{C}^{(i)}$ is an capacitance matrix for element 'i' defined by

$$\mathbf{C}^{(i)} = \int_{v_e} \epsilon^{(i)}\, \mathbf{w}^{(i)}\, \mathbf{w}^{(i)T}\, dv \tag{A.9}$$

where $\mathbf{w}^{(i)}$ is column vector of vector edge interpolation functions on the 'i'th element. Equation (A.8) leads to the global matrix form

$$T^{e*} = \frac{1}{2}\, \mathbf{E}^T\, \mathbf{C}\, \mathbf{E} \tag{A.10}$$

where $\mathbf{E}$ is global vector of electric field intensity variables, and $\mathbf{C}$ is global capacitance matrix.

The discrete electric co-energy function defines generalized electric momenta as

$$\mathbf{X} = \frac{\partial T^{e*}}{\partial \mathbf{E}} = \mathbf{C}\, \mathbf{E} \tag{A.11}$$

where **X** is a discrete electric flux variable, used as a generalized momenta for the system.

A.3 Potential Energy

The general potential energy expression for electromagnetic systems can be written as

$$V = \frac{1}{2} \int_{v} \mu^{-1} \vec{\mathbf{B}} \cdot \vec{\mathbf{B}} \, dv \tag{A.12}$$

where μ is the magnetic permeability. The magnetic flux density interpolation allows the magnetic potential energy function to be expressed in a discrete form as

$$V = \frac{1}{2} \sum_{i=1}^{n_e} \mathbf{B}^{(i)T} \, \mathbf{R}^{(i)} \, \mathbf{B}^{(i)} \tag{A.13}$$

where $\mathbf{B}^{(i)}$ is column vector of magnetic flux density values, $\mathbf{R}^{(i)}$ is a reluctance matrix for element 'i' defined as

$$\mathbf{R}^{(i)} = \int_{V_e} \mu^{(i)-1} \, \mathbf{f}^{(i)} \, \mathbf{f}^{(i)T} \, dV \tag{A.14}$$

and $\mathbf{f}^{(i)}$ is column vector of face interpolation functions in the 'i'th element. Equation (A.13) takes the global form

$$V = \frac{1}{2} \mathbf{B}^T \, \mathbf{R} \, \mathbf{B} \tag{A.15}$$

where **B** is global vector of magnetic flux density variables and **R** is a global reluctance matrix.

The generalized conservative force associated with the magnetic state variables is

$$\mathbf{Y} = \frac{\partial V}{\partial \mathbf{B}} = \mathbf{R}\,\mathbf{B} \tag{A.16}$$

where $\mathbf{Y}$ is a generalized conservative force for the system.

A.4 Evolution Equation: Discrete Faraday's Equation

The evolution equation for the generalized coordinate ($\mathbf{B}$) can be derived from Faraday's equation, in integral form.

$$\int_S \dot{\vec{\mathbf{B}}} \cdot d\vec{S} = -\oint_{\partial S} \vec{\mathbf{E}} \cdot d\vec{\ell} - \int_S \vec{\mathbf{M}} \cdot d\vec{S} \tag{A.17}$$

where $d\vec{S}$ is a differential normal vector, $d\vec{\ell}$ is a differential length vector, and $\vec{\mathbf{M}}$ is a magnetic current density vector. The nonholonomic constraint for surface 'i' is therefore

$$\dot{B}^{(i)} = -S^{(i)-1} \oint \vec{\mathbf{E}} \cdot d\vec{\ell} - M^{(i)} = -\mathbf{a}^{(i)T}\mathbf{E} - M^{(i)} \tag{A.18}$$

where 'i' is a face index, $S^{(i)}$ is a surface area in the 'i'th face, $\mathbf{a}^{(i)}$ is a constant column vector, $M^{(i)}$ is a magnetic current density for face 'i', and $\mathbf{E}$ is a global vector of electric field intensity values. Equation (A.18) for the system is

$$\dot{\mathbf{B}} = -\mathbf{A}\,\mathbf{E} - \mathbf{M} \tag{A.19}$$

where

$$\mathbf{B} = [B^{(1)}\, B^{(2)}\, \cdots B^{(n_f)}]^T \tag{A.20}$$

$$\mathbf{A} = [\mathbf{a}^{(1)}\ \mathbf{a}^{(2)}\ \cdots\ \mathbf{a}^{(n_f)}]^T \tag{A.21}$$

$$\mathbf{M} = [M^{(1)}\, M^{(2)}\, \cdots M^{(n_f)}]^T \tag{A.22}$$

with n_f number of faces in the system. Here $\mathbf{A}$ is a function of geometry and performs the curl operation on $\mathbf{E}$. This constraint is classified as nonholonomic. The coefficient of the generalized velocity in equation (A.19), combined with a Lagrange multiplier, will determine nonconservative generalized forces in the electric momentum equations derived in the later section.

The magnetic current density in equation (A.19) is nonphysical property. However, magnetic conductive current may be used to implement absorbing boundary conditions for infinite domain electromagnetic problems. Hence, it will be treated as numerical damping, and impressed magnetic current density is omitted in this dissertation. The magnetic current density in equation (A.19) is defined as

$$\mathbf{M} = \mathbf{M}^c \tag{A.23}$$

where the superscript 'c' denotes conduction. In magnetic conductive materials, they dissipates energy through irreversible entropy production, with finite conductivity. This is in general represented by a constitutive relation. The constitutive relation is written here in terms of the magnetic flux density for the face 'i' as

$$M^{c(i)} = \frac{\sigma^{m(i)}}{\mu^{(i)}} B^{(i)} \tag{A.24}$$

where $\sigma^{m(i)}$ is magnetic conductivity and $\mu^{(i)}$ is magnetic permeability on the face 'i'. They are assumed to be uniform on the face. The constitutive relation in the system is then

$$\mathbf{M}^c = [M^{c(1)}\, M^{c(2)}\, \cdots\, M^{c(n_f)}]^T = \mathfrak{C}^m\, \mathbf{B} \tag{A.25}$$

where $\mathfrak{C}^m$ is diagonal magnetic conductance matrix. Substituting equation (A.25) into equation (A.19) yields

$$\dot{\mathbf{B}} = -\mathbf{A}\,\mathbf{E} - \mathfrak{C}^m\,\mathbf{B} \tag{A.26}$$

A.5 Electrical Conduction

Electric conduction is considered as a dissipative force and needs to be included in the electric momentum equation. Here Rayleigh's dissipation function is introduced to derive dissipation forces for Lagrangian or Hamiltonian formulations [37][68]. Rayleigh's function (Q_r^e) can be defined for an electric conductor as

$$Q_r^e = \frac{1}{2}\int_v \sigma^e \vec{\mathbf{E}} \cdot \vec{\mathbf{E}}\,dv \tag{A.27}$$

where σ^e is electric conductivity. The discrete form of equation (A.27) is obtained from the sum of the element dissipation functions

$$Q_r^e = \frac{1}{2}\sum_{i=1}^{n_e} \mathbf{E}^{(i)T}\,\mathfrak{R}^{e(i)}\,\mathbf{E}^{(i)} \tag{A.28}$$

where n_e is the number of elements, $\mathbf{E}^{(i)}$ is the column vector of tangential electric field intensity values on the edges of the 'i'th element, and $\mathfrak{R}^{e(i)}$ is the electric resistance matrix for element 'i'

$$\mathfrak{R}^{e(i)} = \int_{v_e} \sigma^{e(i)}\,\mathbf{w}^{(i)}\,\mathbf{w}^{(i)T}\,dv \tag{A.29}$$

Equation (A.28) is for the system

$$Q_r^e = \frac{1}{2}\,\mathbf{E}^T\,\mathfrak{R}^e\,\mathbf{E} \tag{A.30}$$

where $\mathbf{E}$ is global vector of electric field intensity variables, and $\boldsymbol{\mathfrak{R}}^e$ is the global electric resistance matrix.

The electric dissipation force is

$$\mathbf{f}^e = \frac{\partial Q_r^e}{\partial \mathbf{E}} = \boldsymbol{\mathfrak{R}}^e \, \mathbf{E} \tag{A.31}$$

where $\mathbf{f}^e$ is a discrete electric dissipation force and will be included in the nonconservative generalized forces.

A.6 Virtual Work

Electric field intensity variables are used as quasi-velocities and discretized by edge interpolation functions. They are related to the generalized quasi-coordinates by

$$E_i = \dot{q}_i^e \qquad (i = 1, 2, \cdots n_s) \tag{A.32}$$

where n_s is number of edges in the system. The virtual work depends on imposed fields on external boundary surfaces. The nonconservative power associated with these sources is

$$P^{nc} = -\int_S [\vec{\mathbf{H}}^s(\vec{\mathbf{x}}, t) \times \vec{\mathbf{E}}] \cdot \vec{\mathbf{n}} dS - \int_V \vec{\mathbf{J}}^s(t) \cdot \vec{\mathbf{E}} \, dV \tag{A.33}$$

where $\vec{\mathbf{H}}^s(\vec{\mathbf{x}}, t)$ is magnetic field source dependent on space and time, S is the surface bounding the volume element, $\vec{\mathbf{n}}$ is the outward vector normal to the surface S, V is the volume, and $\vec{\mathbf{J}}^s(t)$ is an impressed current source. The virtual work is determined by magnetic field sources, current sources, and the virtual change of the generalized quasi-coordinates. By using the vector identity (3.14), the virtual work in the system can be expressed as

$$\delta W = \sum_{i=1}^{n_e} \delta W^{(i)} \tag{A.34}$$

where

$$\delta W^{(i)} = -\int_{S^{(i)}} [\vec{\mathbf{n}} \times \vec{\mathbf{H}}^s(\vec{\mathbf{x}}, t)] \cdot \delta\vec{\mathbf{q}}^e \, dS - \int_{V^{(i)}} \vec{\mathbf{J}}^s(t) \cdot \delta\vec{\mathbf{q}}^e \, dV \tag{A.35}$$

with n_e number of elements, $S^{(i)}$ the total surface bounding the element 'i', $V^{(i)}$ the volume of element 'i', and $\delta\vec{\mathbf{q}}^e$ a virtual change of the generalized quasi-coordinates for the element. The generalized quasi-coordinates are discretized using edge interpolation functions,

$$\delta\vec{\mathbf{q}}^{e(i)} = \sum_{j=1}^{n_{es}} \vec{\mathbf{w}}_j^{(i)} \delta q_j^{e(i)} = \mathbf{w}^{(i)T} \delta\mathbf{q}^{e(i)} \tag{A.36}$$

where n_{es} is the number of the edges in the element, and $\vec{\mathbf{w}}_j^{(i)}$ is the vector interpolation function for edge 'j' of element 'i'. Substituting equation (A.36) into equation (A.35), the virtual work can be expressed as

$$\delta W^{(i)} = \sum_{j=1}^{n_{es}} Q_j^{(i)} \, \delta q_j^{e(i)} = \mathbf{Q}^{(i)T} \delta\mathbf{q}^{e(i)} \tag{A.37}$$

The last equation can be rearranged using

$$Q_j^{(i)} = Q_j^{s(i)} + Q_j^{I(i)} \tag{A.38}$$

The equation (A.37) becomes

$$\delta W^{(i)} = \sum_{j=1}^{n_{es}} [Q_j^{s(i)} + Q_j^{I(i)}] \, \delta q_j^{e(i)} = [\mathbf{Q}^{s(i)} + \mathbf{Q}^{I(i)}]^T \delta\mathbf{q}^{e(i)} \tag{A.39}$$

where

$$Q_j^{s(i)} = -\int_{S^{(i)}} [\vec{\mathbf{n}} \times \vec{\mathbf{E}}^s(\vec{\mathbf{x}}, t)] \cdot \vec{\mathbf{w}}_j^{(i)} \, dS, \qquad Q_j^{I(i)} = -\int_{V^{(i)}} \vec{\mathbf{J}}^s(t) \cdot \vec{\mathbf{w}}_j^{(i)} \, dV \quad \text{(A.40)}$$

The virtual work for the system is calculated by summing the element level contributions

$$\delta W = \sum_{i=1}^{n_e} \mathbf{Q}^{(i)T} \delta \mathbf{q}^{e(i)} = \sum_{i=1}^{n_e} [\mathbf{Q}^{s(i)} + \mathbf{Q}^{I(i)}]^T [\mathbf{B}^{e(i)} \delta \mathbf{q}^e] \qquad \text{(A.41)}$$

where $\mathbf{B}^{e(i)}$ is a Boolean matrix which relates the edges in the system to the edges of element 'i', and $\delta \mathbf{q}^e$ denotes virtual change of quasi-coordinate. The generalized force can be defined as the vector which is conjugate to the global quasi-coordinates in equation (A.41),

$$\delta W = [\mathbf{F}^s + \mathbf{F}^I]^T \, \delta \mathbf{q}^e \qquad \text{(A.42)}$$

where $\mathbf{F}^s$ is the global force vector associated with the magnetic sources imposed on the external boundary surfaces, and $\mathbf{F}^I$ denotes the global force vector due to the impressed current sources. They are

$$\mathbf{F}^s = \sum_{i=1}^{n_e} \mathbf{B}^{(i)T} \, \mathbf{Q}^{s(i)}, \qquad \mathbf{F}^I = \sum_{i=1}^{n_e} \mathbf{B}^{(i)T} \, \mathbf{Q}^{I(i)} \qquad \text{(A.43)}$$

A.7 Discrete Hamilton's Equations for Electromagnetic Systems

The stored energy functions, constraint equations, and virtual work expressions for the system may be combined with the canonical Hamilton's equations to obtain an ODE model for the electrodynamic system. The system Hamiltonian(Π) is

$$\Pi = T + V = \Pi(\mathbf{X}, \mathbf{B}) \tag{A.44}$$

and the canonical Hamilton's equations are

$$\dot{\mathbf{X}} = \mathbf{Q}^E \tag{A.45}$$

$$\mathbf{0} = -\frac{\partial \Pi}{\partial \mathbf{B}} + \mathbf{Q}^B \tag{A.46}$$

where $\mathbf{Q}^E$ and $\mathbf{Q}^B$ are generalized forces determined by the nonholonomic constraints, dissipation forces, and virtual work. Hamilton's equations take a degenerate form, since there are no generalized coordinates associated with the electric field intensity and no generalized momenta associated with the magnetic flux variable. Hence it is possible to determine in closed form the Lagrange multipliers. The evolution equation for the generalized coordinate $\mathbf{B}$ are classified as nonholonomic constraint. if Lagrange multipliers $\boldsymbol{\lambda}^B$ are introduced for the constraints, it follows that

$$\mathbf{Q}^E = \mathbf{A}^{\mathbf{T}}\boldsymbol{\lambda}^B - \mathbf{f}^e + \mathbf{F}^s + \mathbf{F}^I \tag{A.47}$$

$$\mathbf{Q}^B = \boldsymbol{\lambda}^B \tag{A.48}$$

The Lagrange multiplier is determined by equation (A.46). The electric momentum equation is augmented by the evolution equation (A.26), to produce a complete set of ODE equations for the electromagnetic systems. The final form of Hamilton's equations is

$$\dot{\mathbf{X}} = \quad \mathbf{A}^T \mathbf{R} \mathbf{B} \; - \; \boldsymbol{\mathcal{R}}^e \mathbf{C}^{-1}\mathbf{X} + \mathbf{F}^s + \mathbf{F}^I \tag{A.49}$$

$$\dot{\mathbf{B}} = -\mathbf{A} \mathbf{C}^{-1} \mathbf{X} - \boldsymbol{\mathcal{C}}^m \mathbf{B} \tag{A.50}$$

and are accompanied by the constitutive relations

$$\mathbf{X} = \mathbf{C} \mathbf{E} \tag{A.51}$$

$$\mathbf{Y} = \mathbf{R} \mathbf{B} \tag{A.52}$$

where $\mathbf{R}$ is the global reluctance matrix and $\mathbf{C}$ is the global capacitance matrix. Note that the momentum balance equation is a discrete form of Ampere's law. The divergence constraint on the magnetic displacement is satisfied (in rate form) by the face interpolation, while the divergence constraint on the electric flux is satisfied (in rate form) by the use of an edge interpolation for the electric field intensity. The above equations represent an explicit state space model for the electrodynamic system.

A.8 Example: TE Wave

As a dual case of the TM$_z$ wave problem solved in chapter three, the TE$_z$ mode problem is chosen to test the formulation. This example incorporates a perfect magnetic conducting boundary condition

$$H_z = 0 \left\{ \begin{array}{lll} \text{at } y = 0 & \text{and} & y = y_0 \\ \text{at } x = 0 & \text{and} & x = x_0 \end{array} \right. \tag{A.53}$$

and an initial condition

$$H_z(x, 0) = H_0 sin(\frac{m\,\pi}{x_0}\,x) sin(\frac{n\,\pi}{y_0}\,y) \tag{A.54}$$

where H_0 is the magnitude of the initial magnetic field, m and n are mode shapes, and x_0 and y_0 are the dimensions of the modeled domain. The initial configuration is shown in figure (A.2). The geometric and material parameters are listed in table (3.1). The rectangular computational domain is discretized using the same number of elements as in the TM$_z$ case. Figures (A.3) and (A.4) show the results for the computed electric and magnetic fields, at a stop time of 8.34 ns, which is 20% of one period. They show very good agreement with the exact solutions.

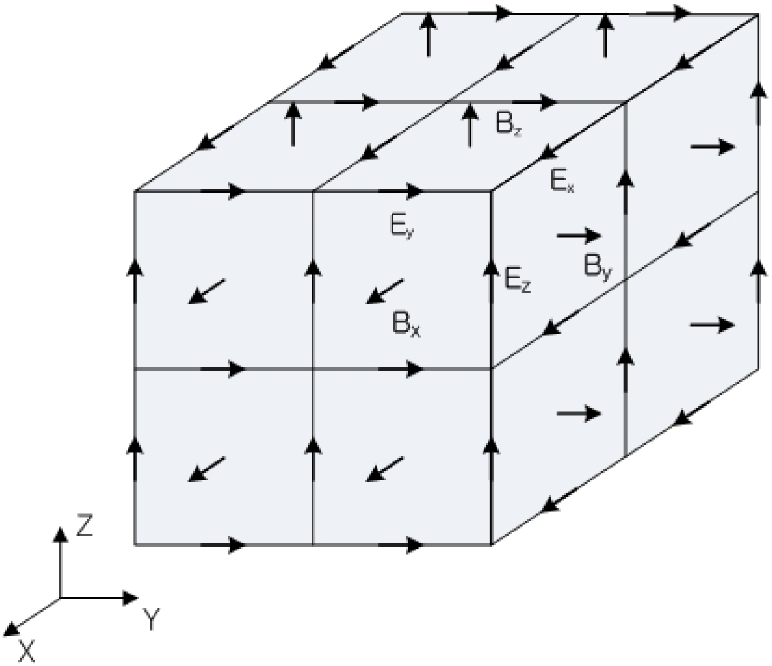

Figure A.1: The discretization of magnetic field and electric field variables for dual formulation

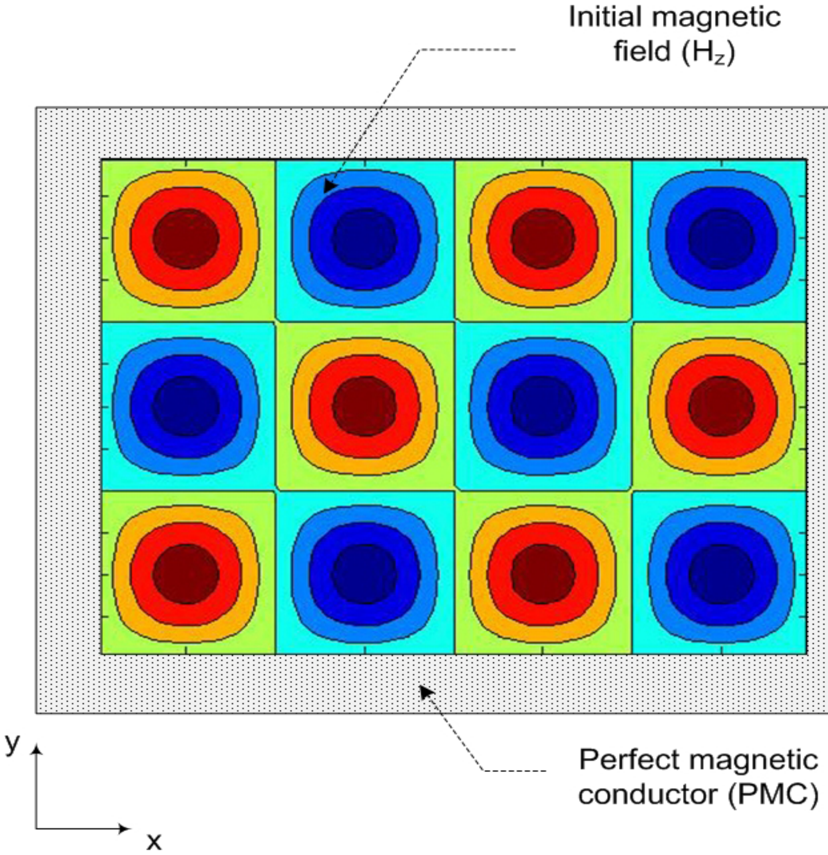

Figure A.2: Initial configuration for TE wave problem

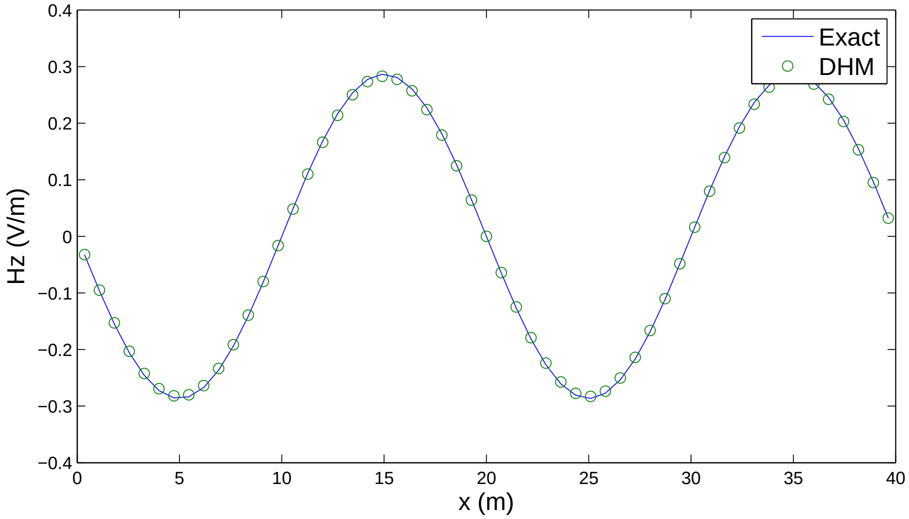

Figure A.3: Comparison of numerical result calculated by dual formulation with exact solution for electric field, Hz at t= 8.34 ns (0.2 × period) and y = 12 m

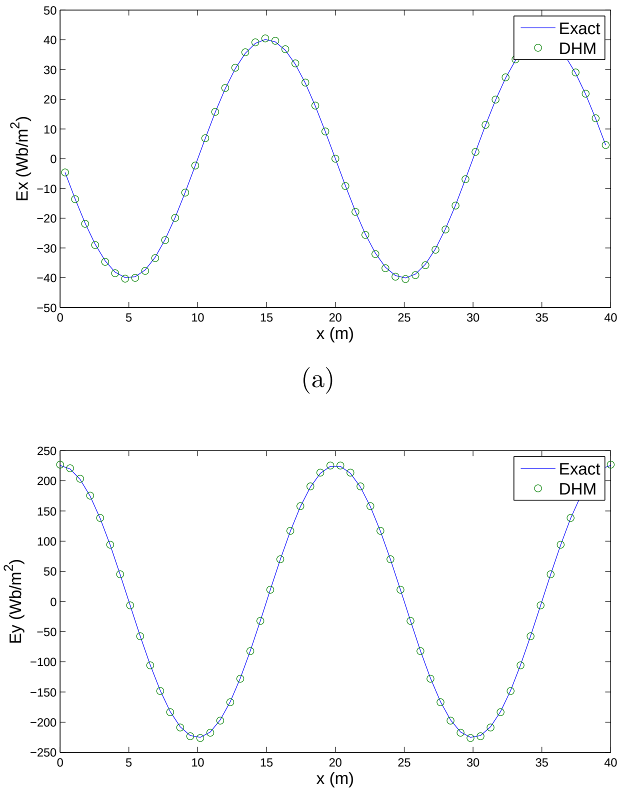

(a)

(b)

Figure A.4: Comparison of numerical results calculated by dual formulation with exact solutions for magnetic field intensities, (a) Ex and (b) Ey at t=8.34 ns (0.2 × period) and y = 12 m

Appendix B

Anisotropic PML in Two Dimensional Problems

The use of uniaxial anisotropic PML [80] as an absorbing boundary condition in infinite domain electromagnetic problems avoids the non-physical and rather cumbersome split field notations of the perfectly matched layer (PML) technique developed by Berenger [7][9]. The parameters $\overline{\overline{\mu}}$ and $\overline{\overline{\epsilon}}$, which are complex diagonal tensors, make the fields reflectionless at interfaces. In this appendix, Hamilton's equations with anisotropic PML are developed for two dimensional problems (transverse magnetic case) in the time domain. The permeability and permittivity tensors are [98][58]

$$\overline{\overline{\mu}}_2 = \mu_1 \begin{bmatrix} \left(1+\frac{\sigma_{2x}}{j\omega\epsilon_1}\right)^{-1}\left(1+\frac{\sigma_{2y}}{j\omega\epsilon_1}\right) & 0 \\ 0 & \left(1+\frac{\sigma_{2x}}{j\omega\epsilon_1}\right)\left(1+\frac{\sigma_{2y}}{j\omega\epsilon_1}\right)^{-1} \end{bmatrix} \tag{B.1}$$

$$\overline{\overline{\epsilon}}_2 = \epsilon_1 \left[\left(1+\frac{\sigma_{2x}}{j\omega\epsilon_1}\right)\left(1+\frac{\sigma_{2y}}{j\omega\epsilon_1}\right)\right] \tag{B.2}$$

As can be seen in the previous chapters, the implementation of the anisotropic PML to the derived formulation is straightforward in the frequency domain. Evolution equations, which represent constitutive equations, are needed in the PML regions. Figure (B.1) shows an anisotropic PML lossy medium outside of the solution domain(Ω_i). The discrete Hamilton's equations (3.64) and (3.65) developed in chapter 3 are written as

$$\dot{\mathbf{P}} = -\mathbf{A}^T \mathbf{F} \tag{B.3}$$

$$\dot{\mathbf{D}} = \mathbf{A}\,\mathbf{H} - \mathbf{J}^s \tag{B.4}$$

with the constitutive relations

$$\mathbf{P} = \mathbf{L}^* \mathbf{H} \tag{B.5}$$

$$\mathbf{F} = \mathbf{K}^* \mathbf{D} \tag{B.6}$$

where $\mathbf{L}^*$ is global complex inductance matrix and $\mathbf{K}^*$ is global complex elastance matrix. The evolution equations, which yield the constitutive equations (B.5) and (B.6), are defined for each region of the PML boundaries.

In region (1) where $\sigma_{2x} \neq 0$ and $\sigma_{2y} = 0$, the evolution equations which yield equation (B.5) are

$$\begin{aligned} \dot{\mathbf{P}}_x &= -\frac{\sigma_{2x}}{\epsilon_1}\,\mathbf{P}_x + \mathbf{L}_x\,\dot{\mathbf{H}}_x \\ \dot{\mathbf{P}}_y &= \frac{\sigma_{2x}}{\epsilon_1}\,\mathbf{L}_y\,\mathbf{H}_y + \mathbf{L}_y\,\dot{\mathbf{H}}_y \end{aligned} \tag{B.7}$$

A similar expression is derived to represent the equation (B.6)

$$\dot{\mathbf{F}}_z = -\frac{\sigma_{2x}}{\epsilon_1}\,\mathbf{F}_z + \mathbf{K}_z\,\dot{\mathbf{D}}_z \tag{B.8}$$

This formulation is validated by modeling a gaussian wave, placed in the center of the x-axis and propagating in the positive and negative x-direction. Note that the grade function described in equation (3.73) is used to reduce discretization error [99][51] and that the numerical values listed in table (3.3) are used in this calculation. Figure (B.2) illustrates electric wave propagation before and after arriving at the anisotropic PML and does not show any noticeable artifacts reflected back into the computational domain.

In region (2) where $\sigma_{2x} = 0$ and $\sigma_{2y} \neq 0$, the evolution equations which yield the equation (B.5) are

$$\begin{aligned} \dot{\mathbf{P}}_x &= \frac{\sigma_{2y}}{\epsilon_1}\,\mathbf{L}_x\,\mathbf{H}_x + \mathbf{L}_x\,\dot{\mathbf{H}}_x \\ \dot{\mathbf{P}}_y &= -\frac{\sigma_{2y}}{\epsilon_1}\,\mathbf{P}_y + \mathbf{L}_y\,\dot{\mathbf{H}}_y \end{aligned} \tag{B.9}$$

while for the equation (B.6)

$$\dot{\mathbf{F}}_z = -\frac{\sigma_{2y}}{\epsilon_1}\,\mathbf{F}_z + \mathbf{K}_z\,\dot{\mathbf{D}}_z \tag{B.10}$$

Using the same gaussian wave, the artificial boundary condition in this region is tested. The results, shown in figure (B.3) indicate very good performance, as the propagating wave passes through the anisotropic PML.

In region (3) where $\sigma_{2x} \neq 0$ and $\sigma_{2y} \neq 0$, both conductivities in the two tensors are nonzero, and an intermediate variable is usually introduced [34][89]. The intermediate variable $\bar{\mathbf{D}}_z$ for equation (B.6) is

$$\bar{\mathbf{D}}_z = (1 + \frac{\sigma_{2y}}{j\omega\epsilon_1})^{-1}\mathbf{D}_z \tag{B.11}$$

so that the evolution equations are

$$\begin{aligned} \dot{\mathbf{P}}_x &= -\frac{\sigma_{2x}}{\epsilon_1}\,\mathbf{P}_x + \frac{\sigma_{2y}}{\epsilon_1}\,\mathbf{L}_x\,\mathbf{H}_x + \mathbf{L}_x\,\dot{\mathbf{H}}_x \\ \dot{\mathbf{P}}_y &= -\frac{\sigma_{2y}}{\epsilon_1}\,\mathbf{P}_y + \frac{\sigma_{2x}}{\epsilon_1}\,\mathbf{L}_y\,\mathbf{H}_y + \mathbf{L}_y\,\dot{\mathbf{H}}_y \\ \dot{\mathbf{F}}_z &= -\frac{\sigma_{2x}}{\epsilon_1}\,\mathbf{F}_z + \mathbf{K}_z\,\dot{\bar{\mathbf{D}}}_z \\ \dot{\bar{\mathbf{D}}}_z &= -\frac{\sigma_{2y}}{\epsilon_1}\,\bar{\mathbf{D}}_z + \mathbf{K}_z\,\dot{\mathbf{D}}_z \end{aligned} \tag{B.12}$$

In the center of the computational domain, a pulse, generated by the same gaussian function, is propagated in the x and y directions. The open boundary conditions formulated for all regions in figure (B.1) are validated. Figure (B.4) does not show noticeable reflection from the anisotropic PML.

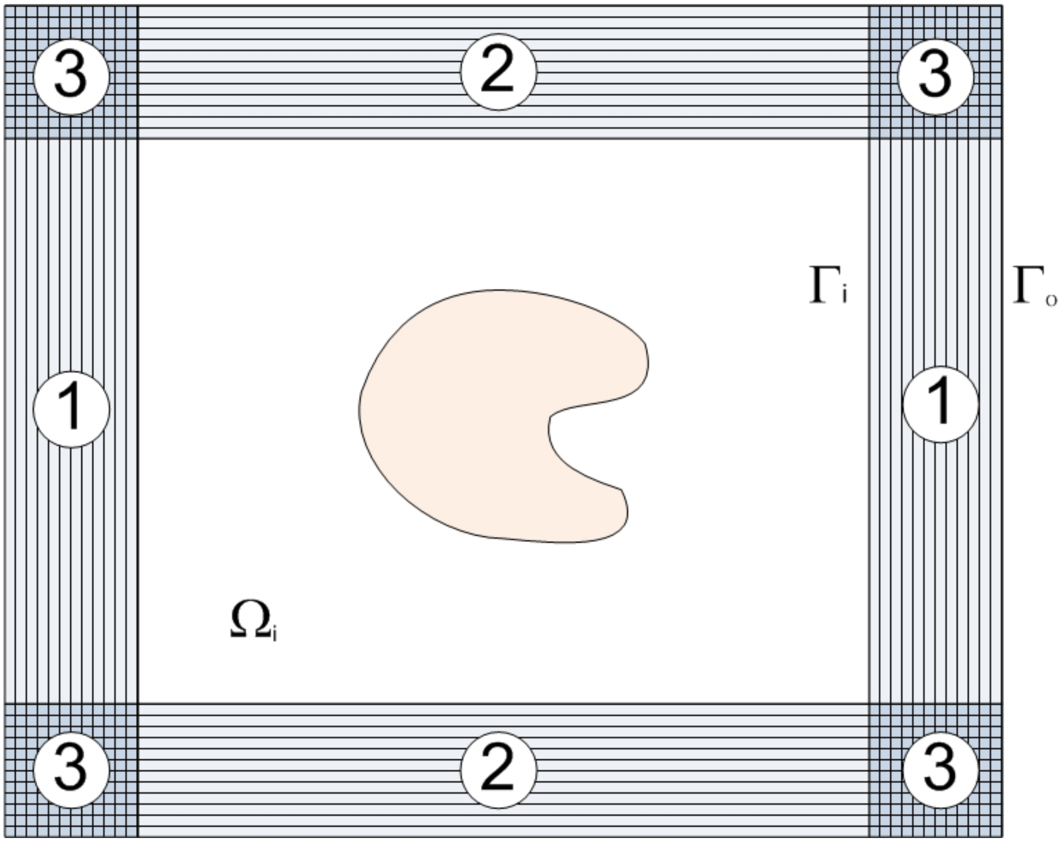

Figure B.1: Configuration of Anisotropic PML for two dimensional open boundary problem.

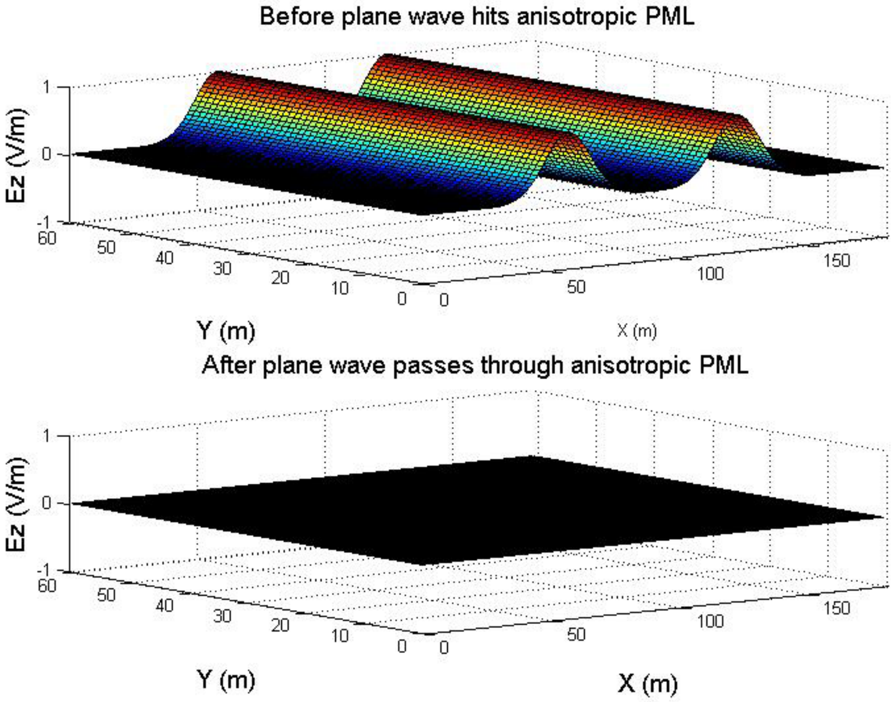
Before plane wave hits anisotropic PML

After plane wave passes through anisotropic PML

Figure B.2: Plane wave generated by Gaussian pulse passes through x-directional anisotropic PML.

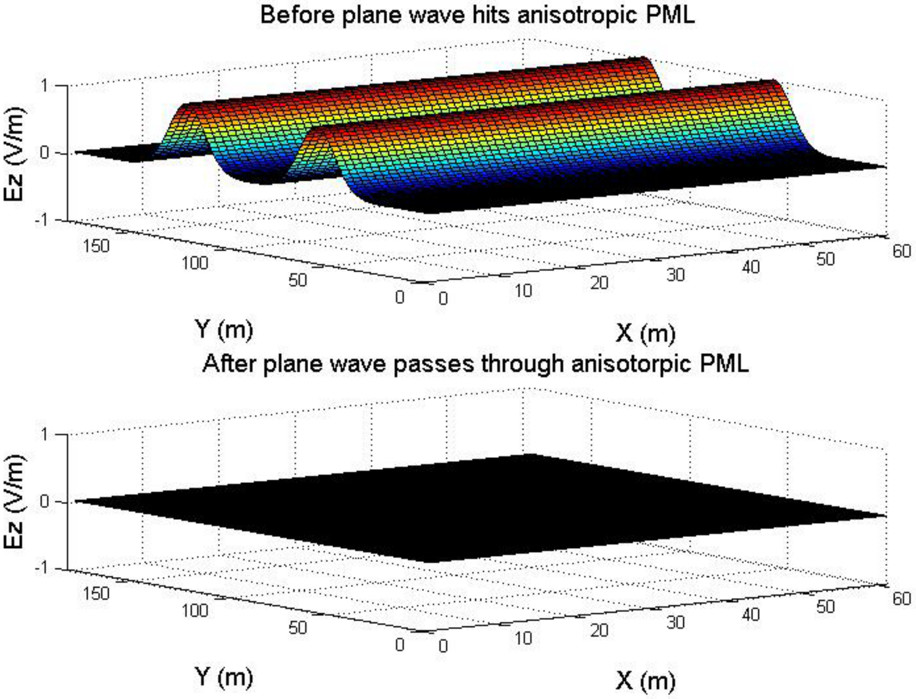

Figure B.3: Plane wave generated by Gaussian pulse passes through y-directional anisotropic PML.

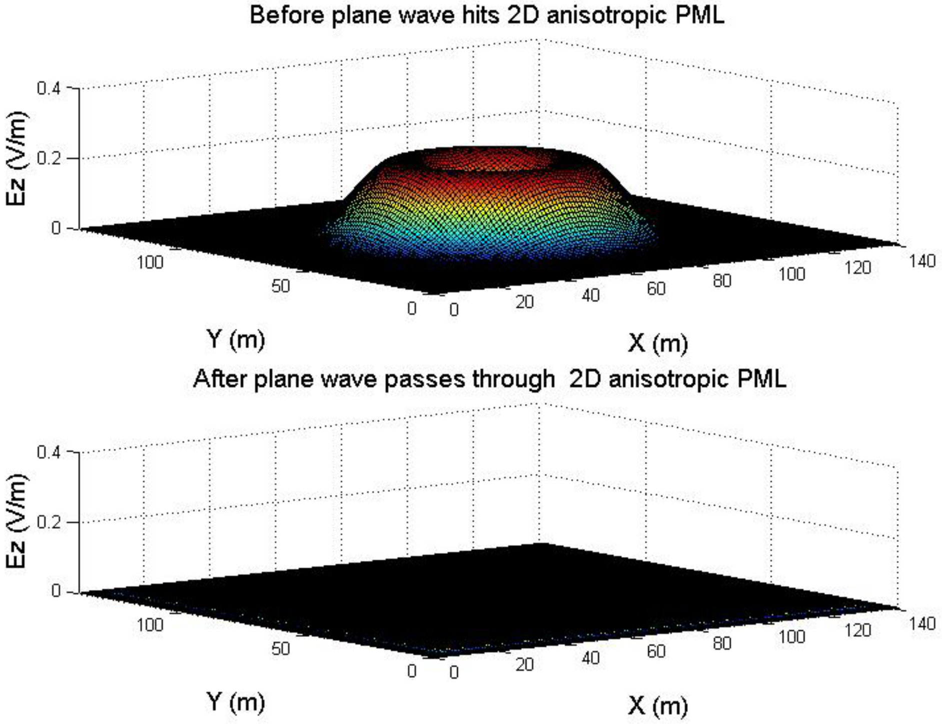

Figure B.4: Plane wave generated by Gaussian pulse passes through two dimensional anisotropic PML.

Appendix C

The Derivation of the Magnetic Inductance Matrix of the Hamiltonian Formulation for the Anisotropic PML

C.1 Uniaxial Anisotropic Lossy Medium

The magnetic co-energy can be defined for a uniaxial anisotropic lossy medium by

$$T^* = \frac{1}{2}\int_v \vec{\mathbf{B}}\cdot\vec{\mathbf{H}}\,dv = \frac{1}{2}\int_v \overline{\overline{\boldsymbol{\mu}}}\,\vec{\mathbf{H}}\cdot\vec{\mathbf{H}}\,dv \tag{C.1}$$

By substituting the magnetic field intensity, interpolated using edge basis functions (2.4), into equation (C.1), the complex magnetic inductance matrix is expressed for element 'i' as

$$\mathbf{L}^{*(i)} = \int_{v^{(i)}} \overline{\overline{\boldsymbol{\mu}}}^{(i)}\,\mathbf{w}^{(i)}\mathbf{w}^{(i)T}dv \tag{C.2}$$

where $\overline{\overline{\boldsymbol{\mu}}}^{(i)}$ is a magnetic permeability tensor in the 'i'th element. It can be represented in tensor form for the hexahedral element as

$$\overline{\overline{\boldsymbol{\mu}}}^{(i)} = \begin{bmatrix} \overline{\overline{\boldsymbol{\mu}}}_x^{(i)} & \mathbf{0} & \mathbf{0} \\ \mathbf{0} & \overline{\overline{\boldsymbol{\mu}}}_y^{(i)} & \mathbf{0} \\ \mathbf{0} & \mathbf{0} & \overline{\overline{\boldsymbol{\mu}}}_z^{(i)} \end{bmatrix} \tag{C.3}$$

where $\overline{\overline{\boldsymbol{\mu}}}_{\xi}^{(i)}$, ξ = x, y, and z, is the magnetic permeability matrix in the ξ-direction for element 'i'

$$\overline{\overline{\boldsymbol{\mu}}}_{\xi}^{(i)} = \begin{bmatrix} \mu_\xi + \frac{\sigma_\xi^m}{j\omega} & 0 & 0 & 0 \\ 0 & \mu_\xi + \frac{\sigma_\xi^m}{j\omega} & 0 & 0 \\ 0 & 0 & \mu_\xi + \frac{\sigma_\xi^m}{j\omega} & 0 \\ 0 & 0 & 0 & \mu_\xi + \frac{\sigma_\xi^m}{j\omega} \end{bmatrix} \tag{C.4}$$

with ω a frequency, σ_ξ^m the magnetic conductivity, and μ_ξ the magnetic permeability in the ξ-direction.

C.2 Anisotropic PML with the Graded Conductivity

The analytically derived permeability tensor for the anisotropic PML is taken from reference [80]

$$\overline{\overline{\boldsymbol{\mu}}}_2 = \mu_1 \begin{bmatrix} (1 + \frac{\sigma}{j\omega\epsilon_1})^{-1} & 0 & 0 \\ 0 & 1 + \frac{\sigma}{j\omega\epsilon_1} & 0 \\ 0 & 0 & 1 + \frac{\sigma}{j\omega\epsilon_1} \end{bmatrix} \tag{C.5}$$

where μ_1 is the magnetic permeability of the air and ϵ_1 is the electric permittivity of the air. From observation of equation (C.5), $\mu_x = \mu_y = \mu_z = \mu_1$ and $\sigma_x^m = \sigma_y^m = \sigma_z^m = \sigma$ in equation (C.4) for the anisotropic PML. If the spatially graded function (3.73) for the conductivity is used, then the magnetic permeability matrix (C.4) can be expressed for the reference hexahedral element in the x-direction as

$$\overline{\overline{\boldsymbol{\mu}}}_x^{(i)} = \mu_1 \begin{bmatrix} \left(1+\frac{\sigma_1^{(i)}}{j\omega\epsilon_1}\right)^{-1} & 0 & 0 & 0 \\ 0 & \left(1+\frac{\sigma_2^{(i)}}{j\omega\epsilon_1}\right)^{-1} & 0 & 0 \\ 0 & 0 & \left(1+\frac{\sigma_3^{(i)}}{j\omega\epsilon_1}\right)^{-1} & 0 \\ 0 & 0 & 0 & \left(1+\frac{\sigma_4^{(i)}}{j\omega\epsilon_1}\right)^{-1} \end{bmatrix} \tag{C.6}$$

and in the y-direction as

$$\overline{\overline{\boldsymbol{\mu}}}_y^{(i)} = \mu_1 \begin{bmatrix} \left(1+\frac{\sigma_5^{(i)}}{j\omega\epsilon_1}\right) & 0 & 0 & 0 \\ 0 & \left(1+\frac{\sigma_6^{(i)}}{j\omega\epsilon_1}\right) & 0 & 0 \\ 0 & 0 & \left(1+\frac{\sigma_7^{(i)}}{j\omega\epsilon_1}\right) & 0 \\ 0 & 0 & 0 & \left(1+\frac{\sigma_8^{(i)}}{j\omega\epsilon_1}\right) \end{bmatrix} \tag{C.7}$$

and in the z-direction as

$$\overline{\overline{\boldsymbol{\mu}}}_z^{(i)} = \mu_1 \begin{bmatrix} \left(1+\frac{\sigma_9^{(i)}}{j\omega\epsilon_1}\right) & 0 & 0 & 0 \\ 0 & \left(1+\frac{\sigma_{10}^{(i)}}{j\omega\epsilon_1}\right) & 0 & 0 \\ 0 & 0 & \left(1+\frac{\sigma_{11}^{(i)}}{j\omega\epsilon_1}\right) & 0 \\ 0 & 0 & 0 & \left(1+\frac{\sigma_{12}^{(i)}}{j\omega\epsilon_1}\right) \end{bmatrix} \tag{C.8}$$

where $\sigma_k^{(i)}$ is the conductivity of the PML layer for edge 'k' of element 'i'.

C.2.1 A Simple Example

An anisotropic PML discretized using three rectangular elements, as shown in figure (C.1), is considered here to explain the derivation of the magnetic inductance matrices for the element 'i' and the system.

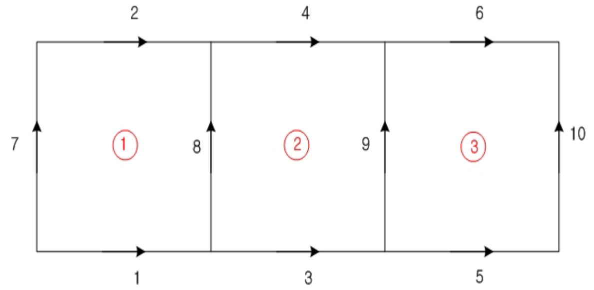

Figure C.1: Simple example

C.2.2 Magnetic Inductance Matrix for Element 'i'

If $a_k = \left(1 + \frac{\sigma_k}{j\omega\epsilon_1}\right)$ and k is an edge index, the magnetic permeability matrix for each element is

$$\overline{\overline{\boldsymbol{\mu}}}^{(i)} = \left[\begin{array}{cc} \overline{\overline{\boldsymbol{\mu}}}_x^{(i)} & 0 \\ 0 & \overline{\overline{\boldsymbol{\mu}}}_y^{(i)} \end{array}\right] \tag{C.9}$$

hence for element (1)

$$\overline{\overline{\boldsymbol{\mu}}}_x^{(1)} = \mu_1 \left[\begin{array}{cc} a_1^{-1} & 0 \\ 0 & a_2^{-1} \end{array}\right] \qquad \overline{\overline{\boldsymbol{\mu}}}_y^{(1)} = \mu_1 \left[\begin{array}{cc} a_7 & 0 \\ 0 & a_8 \end{array}\right] \tag{C.10}$$

and for element (2)

$$\overline{\overline{\boldsymbol{\mu}}}_x^{(2)} = \mu_1 \left[\begin{array}{cc} a_3^{-1} & 0 \\ 0 & a_4^{-1} \end{array}\right] \qquad \overline{\overline{\boldsymbol{\mu}}}_y^{(2)} = \mu_1 \left[\begin{array}{cc} a_8 & 0 \\ 0 & a_9 \end{array}\right] \tag{C.11}$$

and for element (3)

$$\overline{\overline{\boldsymbol{\mu}}}_x^{(3)} = \mu_1 \begin{bmatrix} a_5^{-1} & 0 \\ 0 & a_6^{-1} \end{bmatrix} \qquad \overline{\overline{\boldsymbol{\mu}}}_y^{(3)} = \mu_1 \begin{bmatrix} a_9 & 0 \\ 0 & a_{10} \end{bmatrix} \tag{C.12}$$

Using equation (C.2) with the magnetic permeability matrices for the element 'i', the complex inductance matrices can be defined for element (1) as

$$\mathbf{L}^{*(1)} = \begin{bmatrix} a_1^{-1}L_{11}^{(1)} & a_1^{-1}L_{12}^{(1)} & 0 & 0 \\ a_2^{-1}L_{21}^{(1)} & a_2^{-1}L_{22}^{(1)} & 0 & 0 \\ 0 & 0 & a_7L_{77}^{(1)} & a_7L_{78}^{(1)} \\ 0 & 0 & a_8L_{87}^{(1)} & a_8L_{88}^{(1)} \end{bmatrix} \tag{C.13}$$

and for element (2) as

$$\mathbf{L}^{*(2)} = \begin{bmatrix} a_3^{-1}L_{33}^{(2)} & a_3^{-1}L_{34}^{(2)} & 0 & 0 \\ a_4^{-1}L_{43}^{(2)} & a_4^{-1}L_{44}^{(2)} & 0 & 0 \\ 0 & 0 & a_8L_{88}^{(2)} & a_8L_{89}^{(2)} \\ 0 & 0 & a_9L_{98}^{(2)} & a_9L_{99}^{(2)} \end{bmatrix} \tag{C.14}$$

and for element (3) as

$$\mathbf{L}^{*(3)} = \begin{bmatrix} a_5^{-1}L_{55}^{(3)} & a_5^{-1}L_{56}^{(3)} & 0 & 0 \\ a_6^{-1}L_{65}^{(3)} & a_6^{-1}L_{66}^{(3)} & 0 & 0 \\ 0 & 0 & a_9L_{99}^{(3)} & a_9L_{9,10}^{(3)} \\ 0 & 0 & a_{10}L_{10,9}^{(3)} & a_{10}L_{10,10}^{(3)} \end{bmatrix} \tag{C.15}$$

where L_{kl} are the components of inductance matrices for air.

C.2.3 Magnetic Inductance Matrix for the System

Introducing Boolean functions,

$$\mathbf{L}^* = \sum_{i=1}^{n_e} \mathbf{B}^{e(i)T}\,\mathbf{L}^{*(i)}\,\mathbf{B}^{e(i)} \tag{C.16}$$

where

$$\mathbf{B}^{e(1)} = \begin{bmatrix} 1 & 0 & 0 & 0 & 0 & 0 & 0 & 0 & 0 & 0 \\ 0 & 1 & 0 & 0 & 0 & 0 & 0 & 0 & 0 & 0 \\ 0 & 0 & 0 & 0 & 0 & 0 & 1 & 0 & 0 & 0 \\ 0 & 0 & 0 & 0 & 0 & 0 & 0 & 1 & 0 & 0 \end{bmatrix} \tag{C.17}$$

$$\mathbf{B}^{e(2)} = \begin{bmatrix} 0 & 0 & 1 & 0 & 0 & 0 & 0 & 0 & 0 & 0 \\ 0 & 0 & 0 & 1 & 0 & 0 & 0 & 0 & 0 & 0 \\ 0 & 0 & 0 & 0 & 0 & 0 & 0 & 1 & 0 & 0 \\ 0 & 0 & 0 & 0 & 0 & 0 & 0 & 0 & 1 & 0 \end{bmatrix} \tag{C.18}$$

$$\mathbf{B}^{e(3)} = \begin{bmatrix} 0 & 0 & 0 & 0 & 1 & 0 & 0 & 0 & 0 & 0 \\ 0 & 0 & 0 & 0 & 0 & 1 & 0 & 0 & 0 & 0 \\ 0 & 0 & 0 & 0 & 0 & 0 & 0 & 0 & 1 & 0 \\ 0 & 0 & 0 & 0 & 0 & 0 & 0 & 0 & 0 & 1 \end{bmatrix} \tag{C.19}$$

the magnetic inductance matrix is for the system is

$$\mathbf{L}^* =$$

$$\begin{bmatrix} a_1^{-1}L_{11}^{(1)} & a_1^{-1}L_{12}^{(1)} & 0 & 0 & 0 & 0 & 0 & 0 & 0 & 0 \\ a_2^{-1}L_{21}^{(1)} & a_2^{-1}L_{22}^{(1)} & 0 & 0 & 0 & 0 & 0 & 0 & 0 & 0 \\ 0 & 0 & a_3^{-1}L_{33}^{(2)} & a_3^{-1}L_{34}^{(2)} & 0 & 0 & 0 & 0 & 0 & 0 \\ 0 & 0 & a_4^{-1}L_{43}^{(2)} & a_4^{-1}L_{44}^{(2)} & 0 & 0 & 0 & 0 & 0 & 0 \\ 0 & 0 & 0 & 0 & a_5^{-1}L_{55}^{(3)} & a_5^{-1}L_{56}^{(3)} & 0 & 0 & 0 & 0 \\ 0 & 0 & 0 & 0 & a_6^{-1}L_{65}^{(3)} & a_6^{-1}L_{66}^{(3)} & 0 & 0 & 0 & 0 \\ 0 & 0 & 0 & 0 & 0 & 0 & a_7L_{77}^{(1)} & a_7L_{78}^{(1)} & 0 & 0 \\ 0 & 0 & 0 & 0 & 0 & 0 & a_8L_{87}^{(1)} & a_8L_{88}^{(1)} + a_8L_{88}^{(2)} & a_8L_{89}^{(2)} & 0 \\ 0 & 0 & 0 & 0 & 0 & 0 & 0 & a_9L_{98}^{(2)} & a_9L_{99}^{(2)} + a_9L_{99}^{(3)} & a_9L_{9,10}^{(3)} \\ 0 & 0 & 0 & 0 & 0 & 0 & 0 & 0 & a_{10}L_{10,9}^{(3)} & a_{10}L_{10,10}^{(3)} \end{bmatrix} \tag{C.20}$$

which can be rewritten as

$$\mathbf{L}^* = \overline{\overline{\mathbf{S}}}\,\mathbf{L} \tag{C.21}$$

where

$$\overline{\overline{\mathbf{S}}} = \begin{bmatrix} a_1^{-1} & 0 & 0 & 0 & 0 & 0 & 0 & 0 & 0 & 0 \\ 0 & a_2^{-1} & 0 & 0 & 0 & 0 & 0 & 0 & 0 & 0 \\ 0 & 0 & a_3^{-1} & 0 & 0 & 0 & 0 & 0 & 0 & 0 \\ 0 & 0 & 0 & a_4^{-1} & 0 & 0 & 0 & 0 & 0 & 0 \\ 0 & 0 & 0 & 0 & a_5^{-1} & 0 & 0 & 0 & 0 & 0 \\ 0 & 0 & 0 & 0 & 0 & a_6^{-1} & 0 & 0 & 0 & 0 \\ 0 & 0 & 0 & 0 & 0 & 0 & a_7 & 0 & 0 & 0 \\ 0 & 0 & 0 & 0 & 0 & 0 & 0 & a_8 & 0 & 0 \\ 0 & 0 & 0 & 0 & 0 & 0 & 0 & 0 & a_9 & 0 \\ 0 & 0 & 0 & 0 & 0 & 0 & 0 & 0 & 0 & a_{10} \end{bmatrix}$$

$$\begin{aligned} \mathbf{L} &= \begin{bmatrix} L_{11}^{(1)} & L_{12}^{(1)} & 0 & 0 & 0 & 0 & 0 & 0 & 0 & 0 \\ L_{21}^{(1)} & L_{22}^{(1)} & 0 & 0 & 0 & 0 & 0 & 0 & 0 & 0 \\ 0 & 0 & L_{33}^{(2)} & L_{34}^{(2)} & 0 & 0 & 0 & 0 & 0 & 0 \\ 0 & 0 & L_{43}^{(2)} & L_{44}^{(2)} & 0 & 0 & 0 & 0 & 0 & 0 \\ 0 & 0 & 0 & 0 & L_{55}^{(3)} & L_{56}^{(3)} & 0 & 0 & 0 & 0 \\ 0 & 0 & 0 & 0 & L_{65}^{(3)} & L_{66}^{(3)} & 0 & 0 & 0 & 0 \\ 0 & 0 & 0 & 0 & 0 & 0 & L_{77}^{(1)} & L_{78}^{(1)} & 0 & 0 \\ 0 & 0 & 0 & 0 & 0 & 0 & L_{87}^{(1)} & L_{88}^{(1)} + L_{88}^{(2)} & L_{89}^{(2)} & 0 \\ 0 & 0 & 0 & 0 & 0 & 0 & 0 & L_{98}^{(2)} & L_{99}^{(2)} + L_{99}^{(3)} & L_{9,10}^{(3)} \\ 0 & 0 & 0 & 0 & 0 & 0 & 0 & 0 & L_{10,9}^{(3)} & L_{10,10}^{(3)} \end{bmatrix} \\ &= \begin{bmatrix} \mathbf{L}_x & \mathbf{0} \\ \mathbf{0} & \mathbf{L}_y \end{bmatrix} \end{aligned} \tag{C.22}$$

Here $\mathbf{L}$ is the magnetic inductance matrix for the air, and $\mathbf{L}_x$ and $\mathbf{L}_y$ are the partitioned matrices corresponding to the x and y directions. In a similar way, the elastance matrix for the system can be derived.

Bibliography

[1] http://zpinch.sandia.gov/.

[2] R. Albanese. Analysis of three dimensional electromagnetic fields using edge elements. *Journal of Computational Physics*, 108:236–245, 1993.

[3] B. Anderson and Z. Cendes. Solution of ferrite loaded waveguide using vector finite elements. *IEEE Transactions on Magnetics*, 31(3):1578–1581, May, 1995.

[4] P.L. Arlett, A.K. Bahrani, and O.C. Zienkiewicz. Application of finite elements to the solution of helmholtz's equation. *Proceedings of the IEEE*, 115:1762–1766, 1968.

[5] Constantine A. Balanis. *Advanced Engineering Electromagnetics.* John Wiley & Sons, 1989.

[6] A. Bayliss, M. Gunzburger, and E. Turkel. Boundary conditions for the numerical solution of elliptic equations in exterior domains. *SIAM Journal on Applied Mathematics*, 42:430–451, 1982.

[7] J.P. Berenger. A pefectly matched layer for the absorption of electromagnetic waves. *Journal of Computational Physics*, 114:185–200, 1994.

[8] J.P. Berenger. Perfectly matched layer for the fdtd solution of wave-structure interaction problems. *IEEE Transactions on Antennas and Propagation*, 51:110–117, 1996.

[9] J.P. Berenger. Three dimensional pefectly matched layer for the absorption of electromagnetic waves. *Journal of Computational Physics*, 127:363–379, 1996.

[10] Scipione Bobbio. *Electrodynamics of Materials: Forces, Stresses, and Energies in Solids and Fluids.* Academic Press, 2000.

[11] D.T. Borup, D.M. Sullivan, and O.P. Gandhi. Comparison of the fft consjugate gradient method and the finite-difference time-domain method for the 2-d absorption problem. *IEEE Transactions on Microwave Theory and Techniques*, MTT-35(4):383–405, April, 1987.

[12] A. Bossavit. A rationale for "edge-elements". *IEEE Transactions on Magnetics*, 24(1):74–79, 1988.

[13] A. Bossavit. Solving maxwell equations in a closed cavity, and the question of spurious modes. *IEEE Transactions on Magnetics*, 26(2):702–705, Mar, 1990.

[14] A. Bossavit. Whitney forms: A class of finite elements for three-dimensional computations in electromagnetism. *IEE-A Proceedings*, 135(8):493–500, Nov, 1988.

[15] Y.Y. Botros and J.L. Volakis. Perfectly matched layer termination for finite-element meshes: implementation and application. *Microwave and Optical Technology Letters*, 23(3), November, 1999.

[16] F. Brezzi, M.I. Perugia, P.D. Barba, and Savini A. A novel field-based mixed formulation of magnetostatics. *IEEE Transactions on Magnetics*, 32(3):635–638, May, 1996.

[17] F. Brezzi, M.I. Perugia, P.D. Barba, and Savini A. A novel field-based mixed formulation of magnetostatics. *IEEE Transactions on Magnetics*, 32(3):635–638, May, 1996.

[18] H.E. Bussey and J.H. Richmond. Scattering by a lossy dielectric circular cylindrical multilayer numerical values. *IEEE Transactions on Antennas and Propagation*, pages 383–405, September, 1975.

[19] M.V.K. Chari, P. Silvester, A. Konrad, Csendes Z.J., and M.A. Palmo. Three-dimensional magnetostatic field analysis of electrical machinery by the finite element method. *IEEE Transactions on Power Apparatus and Systems*, PAS-100(8):4007–4019, Aug, 1981.

[20] J.M. Chatterjee and J.L. Volakis. Computation of cavity resonances using edge-based finite elements. *IEEE Transactions on Microwave theory and techniques*, 40(11):180–185, November, 1992.

[21] David K. Cheng. *Field and Wave Electromagnetics.* Addison-Wesley Pub. Co., 1990.

[22] W.C. Chew and W.H. Weedon. A 3d perfectly matched medium from modified maxwell's equations with stretched coordinates. *Microwave and Optical Technology Letters*, 7(13):599–604, September 1994.

[23] B. Crain and A. Peterson. Analysis of propagation on open microstrip lines using mixed order covariant projection vector finite elements. *International Journal of Microwave and Millimeter-Wave Computer Aided Engineering*, 5(2):59–67, May, 1995.

[24] N.A. Demerdash, F.A. Fouad, T.W. Nehl, and O.A. Mohammed. Three dimensional finite element vector potential formulation of magnetic fields in electrical apparatus. *IEEE Transactions on Power Apparatus and Systems*, PAS-100(8):4104–4111, 1981.

[25] K.E. Drexler. *Nanosystems*. John Wiley & Sons, New York, 1992.

[26] J. Driesen, J.M. Belmans, and K. Hameyer. Methodologies for coupled transient electromagnetic-thermal finite-element modeling of electrical energy transducers. *IEEE Transactions on Industry Applications*, 38(5):1244–1250, Sep/Oct, 2002.

[27] E.P. Fahrenthold. Materials selection in elctromagnetic launcher design. *Journal of Engineering Materials and Technology*, 111:319–326, July 1989.

[28] E.P. Fahrenthold. Materials selection in electromagnetic launcher design. *Journal of Engineering Materials and Technology*, 111:319–326,

July, 1989.

[29] E.P. Fahrenthold and C.R. Hean. Discrete lagrange equations for thermofluid systems. *Journal of Dynamic Systems, Measurment, and Control*, 130:011009–1–011009–7, January 2008.

[30] E.P. Fahrenthold and B.A. Horban. Thermodynamics of continuum damage and fragmentation models for hypervelocity impact. *International Journal of Impact Engineering*, 20:241–252, 1997.

[31] E.P. Fahrenthold and S. Lee. Discrete hamilton's equations for magneto-thermoelastic-plastic media. In *Proceedings of the 33rd Plasmadynamics and Lasers Conference*, pages 2002–2168. AIAA Paper, 2002.

[32] E.P. Fahrenthold, J.H. Price, and D.R. Peterson. Structure design of cylindrical railguns. *IEEE Transactions on Magnetics*, 25(1):180–185, January, 1989.

[33] E.P. Farenthold and J.C. Koo. Hybrid particle-element bond graphs for impact dynamics simulation. *Journal of Dynamics, Measurement, and Control*, 122:306–313, June 2000.

[34] S.D. Gedney. An anisotropic perfectly matched layer-absorbing medium for the truncation of fdtd lattices. *IEEE Transactions on Antennas and Propagation*, 44(12), December 1996.

[35] J.H. Ginsberg. *Advanced Engineering Dynamics.* Harper and Row, Inc., Cambridge, 1998.

[36] J. Gong and J.L. Volakis. Optimal selection of uniaxial artificial absorber layer for truncating finite element meshes. *Electronics Letters*, 31(18), August, 1995.

[37] D.T. Greenwood. *Principles of Dynamics.* Prentice Hall, Inc., 1988.

[38] P. Hammond. *Energy Methods in Electromagnetism.* Oxford University Press, 1981.

[39] R.F. Harrington. *Field computations by moment methods.* Macmillan, New York, 1968.

[40] Roger F. Harrington. *Time-Harmonic Electromagnetic Fields.* McGRAW-HILL BOOK COMPANY, 1961.

[41] William H. Hayt and John A. Buck. *Classical Electrodynamics.* John Wiley & Sons, 1998.

[42] R.L. Higdon. Absorbing boundary conditions for difference approximations to the multi-dimensional wave equation. *Mathematics of Computation*, 47:437–459, 1986.

[43] B.A. Horban. *A hamiltonian particle-finite element method for elastic-plastic impact simulation.* PhD thesis, The University of Texas at Austin, 2001.

[44] B.A. Horban and E.P. Fahrenthold. Hamilton's equations for impact simulations with perforation and fragmentation. *Journal of Dynamic Systems, Measurement, and Control*, 127:617–622, December 2005.

[45] John David Jackson. *Classical Electrodynamics*. John Wiley & Sons, 1998.

[46] D. Jiao and J.M. Jin. Three-dimensional orthogonal vector basis functions for time-domain finite element solution of vector wave equations. *IEEE Transactions on Antennas and Propagation*, 51(1), January, 2003.

[47] D. Jiao and J.M. Jin. An effective algorithm for implementing perfectly matched layers in time-domain finite-element simulation of open-region em problems. *IEEE Transactions on Antennas and Propagation*, 50(11), November, 2002.

[48] D. Jiao, J.M. Jin, E. Michielssen, and D.J. Riley. Time-domain finite-element simulation of three-dimensional scattering and radiation problems using perfectly matched layers. *IEEE Transactions on Antennas and Propagation*, 51(2), February, 2003.

[49] Jianming Jin. *The Finite Element Method in Electromagnetics*. John Wiley & Sons, 2002.

[50] C.C. Johnson and A.W. Guy. Nonionizing electromagnetic wave effects in biological materials and systems. *Proceedings of The IEEE*, 60(6):692–718, June, 1972.

[51] D.S. Katz, E.T. Thiele, and A. Taflove. Validation and extension to three dimensional of the berenger pml absorbing boundary condition for

fd-td meshes. *IEEE Microwave and Guided Wave Letters*, 4(8):268–270, Aug, 1994.

[52] D.S. Katz, E.T. Thiele, and A. Taflove. Validation and extension to three dimensions of the berenger pml absorbing boundary condition for fd-td meshes. *IEEE Microwave and Guided Wave Letters*, 4(8), August, 1994.

[53] K.L. Kelly, A.A. Lazarides, and G.C. Schatz. Computational electromagnetics of metal nanoparticles and their aggregates. *Computing in Science and Engineering*, pages 67–73, July/August, 2001.

[54] R. E. Kidder. Nonlinear diffusion of strong magnetic fields in a conducting half space. *University of California Lawrence Radiation Laboratory Report*, UCRL-5467, 1959.

[55] D.M. Kingsland, J. Gong, J.L. Volakis, and J.F. Lee. Performance of an anisotropic artificial absorber for truncating finite-element meshes. *IEEE Transactions on Antennas and Propagation*, 44(7), July, 1996.

[56] J.C. Koo. *Energy-Based Modeling of Physical Systems with Continuous Media*. PhD thesis, The University of Texas at Austin, 1997.

[57] J.C. Koo and E.P. Farenthold. Discrete hamilton's equations for arbitrary lagrangian eulerian dynamics of viscous compressible flow. *Computer Methods in Applied Mechanics and Engineering*, 189:875–900, 2000.

[58] M. Kuzuoglu and R. Mittra. Investigation of nonplanar perfectly matched absorbers for finite-element mesh truncation. *IEEE Transactions on Antennas and Propagation*, 45(3), March, 1997.

[59] J. Lee, D. Sun, and Z. Cendes. Full-wave analysis of dielectric waveguides using tangential vector finite elements. *IEEE Transactions on Microwave Theory and Techniques*, 39(8):1262–1271, Aug, 1991.

[60] J. Lee, D.K. Sun, and Z. Cendes. Tangential vector finite elements for electromagnetic field computation. *IEEE Transactions on Magnetics*, 27(5):4032–4035, Sep, 1991.

[61] J.F. Lee and Z.S. Sacks. Whitney element time domain (wetd) methods. *IEEE Transactions on Magnetics*, 31(3):1325–1329, May, 1995.

[62] W.K. Liu, S. Hao, T. Belytschko, S. Li, and Chang C.T. Multi-scale methods. *International Journal for Numerical Methods in Engineering*, 47:1343–1361, 2000.

[63] G. C. Long. *Fundamental limits to the velocity of solid armatures in railguns*. PhD thesis, The University of Texas at Austin, 1987.

[64] K. Mahadevan and R. Mittra. Radar cross section computation of inhomogeneous scatterers using edge based finite element method in time and frequency domains. *Radio Science*, 28(6):1181–1193, Nov/Dec, 1993.

[65] K. Mahadevan, R. Mittra, and P.M. Vaidya. Use of whitney's edge and face elements for efficient finite element time domain solution of

maxwell's equations. *Journal of Electromagnetic Waves and Applications*, 8(9-10):1173–1191, 1994.

[66] B.H. McDonald and A. Wexler. Finite-element solution of unbounded field problems. *IEEE Transactions on Microwave Theory and Techniques*, 20(12):841–847, 1972.

[67] L. Meirovitch. *Elements of Vibration Analysis*. McGraw-Hill, Inc., 1975.

[68] L. Meirovitch. *Principles and Techniques of Vibrations*. Prentice Hall, Inc., 1997.

[69] P.B. Monk. A mixed method for approximating maxwells equations. *SIAM Jounal on Numerical Analysis*, 28(6):1610–1634, Dec, 1991.

[70] C.D. Munz, R. Schneider, and U. Vob. A finite volume method for the maxwell equations in the time domain. *SIAM Journal of Scientific Computing*, 22(2):449–475, 2000.

[71] A. Nakano, M.E. Bachlechner, R.K. Kalia, E. Lidorkis, P. Vashishta, and G.Z. Voyiadjis. Multiscale simulation of nanosystems. *Computing in Science and Engineering*, pages 56–66, July/August 2001.

[72] J.C. Nedelec. Mixed finite elements in r3. *Numerische Mathematik*, 35(3):315–341, Sep, 1980.

[73] Y.K. Park and E.P. Farenthold. A kenel free particle finite-element method for hypervelocity impact simulation. *International Journal for Numerical Methods in Engineering*, 63:737–759, 2005.

[74] R.E. Peterkin, M.H. Frese, and C.R. Sovinec. Transport of magnetic flux in an arbitrary coordinate ale code. *Journal of Computational Physics*, 140:148–171, 1998.

[75] Robert J Rabb. *A mesomechanical particle-Element model of impact dynamics in neat and shear thickening fluid kevlar.* PhD thesis, The University of Texas at Austin, 2007.

[76] D.C. Rapaport. Molecular dynamics simulation using quaternions. *Journal of Computational Physics*, 41:306–314, 1985.

[77] C.J. Reddy, M.D. Deshpande, C.R. Cockrell, and F.B. Beck. Finite elements method for eigenvalue problems in electromagnetics. *Nasa Technical Paper 3485*, pages 1–27, December, 1994.

[78] J.H. Richmond. Scattering by a dielectric cylinder of arbitrary cross section shape. *IEEE Transactions on Antennas Propagation*, 13(3):334–341, 1965.

[79] G. Rodrigue and D. White. A vector finite element time-domain method for solving maxwell's equations on unstructured hexahedral grids. *SIAM Journal on Scientific Computing*, 23(3):683–706, 2001.

[80] Z.S. Sacks, D.M. Kingsland, R. Lee, and J.F. Lee. A perfectly matched anisotropic absorber for use as an absorbing boundary condition. *IEEE Transactions on Antennas and Propagation*, 43(12):1460–1463, December, 1995.

[81] R. Shivarama and E.P. Farenthold. An ellipsoidal particle finite-element method for hypervelocity impact simulation. *International Journal for Numerical Methods in Engineering*, 59:737–753, 2004.

[82] P.P. Silverster and M.S. Hsieh. Finite-element solution of two-dimensional exterior field problems. *IEE Proceedings - Part H: Microwaves, Antennas and Propagation*, 118:1743–1747, Dec, 1971.

[83] P. Silvester. Finite element solution of homogeneous waveguide problems. *Alta frequenza*, 38:313–317, 1969.

[84] P.P. Silvester and R.L. Ferrari. *Finite Element for Electrical Engineers*. Cambridge University Press, New York, 1983.

[85] D. Srivastava, M. Menon, and Cho K. Computational nanotechnology with carbon nanotubes and fullerenes. *Computing in Science and Engineering*, pages 42–55, July/August 2001.

[86] D.M. Sullivan, O.P. Gandhi, and A. Taflove. Use of the finite-difference time-domain method for calculating em absorption in man models. *IEEE Transactions on Biomedical Engineering*, 35(3):179–186, March, 1988.

[87] D. Sun, J. Magnes, X. Yuan, and Z. Cendes. Spurious modes in finite element methods. *IEEE Antennas and Propagation Magazine*, 37(5):12–24, Oct, 1995.

[88] A. Taflove. Review of the formulation and applications of the finite-differenc time-domain method for numerical modeling of electromagnetic wave interaction with arbitrary structures. *Wave Motion*, 10:547–582, 1988.

[89] Allen Taflove and Susan C. Hagness. *Computational Electrodynamics: The Finite-Difference Time-Domain Method*. Artech House, 1995.

[90] F. Torres and B. Jecko. Complete fdtd analysis of microwave heating processes in frequency-dependent and temperature-dependent media. *IEEE Transactions on Micorowave Theory and Techniques*, 45(1):108–117, Jan, 1997.

[91] K. Umashankar and A. Taflove. A novel method to analyze electromagnetic scattering of complex objects. *IEEE Transactions on Electromagnetic compatibility*, EMC-24(4):397–405, November, 1982.

[92] H. Vanicek and S. Satapathy. Thermal characteristics of a laboratory em launcher. *Electromagnetic Launch Technology*, pages 133– 137, May, 2005.

[93] J.C. Veihl and R. Mittra. An efficient implementation of berenger's perfectly matched layer (pml) for finite-differece time-domain mesh trunca-

tion. *IEEE Microwave and Guided Wave Letters*, 6(2), February, 1996.

[94] John L. Volakis, Arindam Chatterjee, and Leo C. Kempel. *Finite Element Method for Electromagnetics: Antennas, Microwave Circuits, and Scattering Applications.* IEEE PRESS, 1998.

[95] B.K. Wallin, C. Tong, A.L. Nichols, and E.T. Chow. Large multiphysics simulations in ale3d. *Presented at the Tenth SIAM Conference on Parallel Processing for Scientific Computing*, Portsmouth, Virginia, March 12–14, 2001.

[96] J.D. Wargo. *Vector and Tensor-Based Bond Graphs for Solid Dynamics.* PhD thesis, The University of Texas at Austin, 1994.

[97] D.A. White. Orthogonal vector basis functions for time domain finite element solution of the vector wave equation. *IEEE Transactions on Magnetics*, 35(3), May, 1999.

[98] J.Y. Wu, D.M. Kingsland, J.F. Lee, and R. Lee. A comparison of anisotropic pml to berenger's pml and its application to the finite-element method for em scattering. *IEEE Transactions on Antennas and Propagation*, 45(1), January, 1997.

[99] Z. Wu and J. Fang. High-performance pml algorithms. *IEEE Microwave and Guided Wave Letters*, 6:335–337, 1996.

[100] Z. Xi, C.H. Chan, and B. Zhang. An explicit fourth-order orthogonal curvilinear staggered-grid fdtd method for maxwell's equations. *Journal of Computational Physics*, 175:739–763, 2002.

[101] K.S. Yee. Numerical solution of initial boundary value problems involving maxwell's equations in isotropic media. *IEEE Transactions on Antennas and Propagation*, 14:302–307, 1966.

Vita

Seunghan Lee was born in Pusan, South Korea on 26 November 1969, the son of Yoon Lee and Kukja Kim. He pursued the undergraduate education at the Sungkyunkwan University where he graduated with a Bachelor of Science degree in Mechanical Engineering in 1994. He worked as a Elevator Sales Person at LG Industrial Electric Company for 1994 and 1995. In the fall of 1996, he joined the Mechanical Department in the University of Michigan at Ann Arbor where he received a Master of Science in Engineering. In august 1998, he entered the Mechanical Systems and Design program in the University of Texas at Austin to continue his doctoral work in Mechanical Engineering.

Permanent address: 514-903 LG5-Cha Village Sinbong-Dong
Yongin-Si, Gyeonggi-Do Rep. of Korea 449-537

This dissertation was typeset with LaTeX† by the author.

---

†LaTeX is a document preparation system developed by Leslie Lamport as a special version of Donald Knuth's TeX Program.